Direct and Non-Invasive Monitoring of Battery Internal State Via Novel GMI-IDT Magnetic Sensor

Akila Khatun
Marquette University

DIRECT AND NON-INVASIVE MONITORING OF BATTERY INTERNAL STATE VIA NOVEL GMI-IDT MAGNETIC SENSOR

by

AKILA KHATUN, B.Sc., M. Sc.

A Dissertation submitted to the Faculty of the Graduate School,
Marquette University,
in Partial Fulfillment of the Requirements for
the Degree of Doctor of Philosophy in Electrical and Computer Engineering.

Milwaukee, Wisconsin

December 2021

ABSTRACT
DIRECT AND NON-INVASIVE MONITORING OF BATTERY INTERNAL STATE VIA NOVEL GMI-IDT MAGNETIC SENSOR

Akila Khatun, B.Sc., M. Sc.

Marquette University, 2021

Efficient battery management systems (BMSs) in rechargeable battery-based systems require precise measurements of various battery parameters including state of charge (SOC), state of health (SOH) and charge capacity. Presently, SOC, charge capacity and SOH can only be indirectly inferred from long-term measurement of current, open circuit voltage (OCV), and temperature using multiple sensors. These techniques can only give an approximation of SOC and often require knowledge of the recent battery history to prevent excessive inaccuracy.

To improve the performance of the BMS, an alternative method of monitoring the internal state of Li-ion batteries is presented here. Theoretical analysis of Li-ion batteries has indicated that the concentration of active lithium ions in the cathode is directly related to the magnetic susceptibility of the electrode materials. While charging/discharging, due to the change in the oxidation and/or spin state of metal atoms, the magnetic moment in the cathode varies. This indicates the potential for directly probing the internal state of the Li-ion batteries during charging/discharging by monitoring the changes in magnetic susceptibility via an appropriately designed magnetic sensor.

In this research, a highly sensitive micromagnetic sensor design is investigated consisting of a single interdigital transducer (IDT) shunt-loaded with a magnetically sensitive Giant Magnetoimpedance (GMI) microwire. This design takes advantage of the coupling of the impedance characteristics of the GMI microwire to the IDT transduction process. The initial GMI-IDT sensor design is further developed and modified to maximize sensitivity and linearity. The sensor can detect magnetic field in the range of 900 nT and minute changes less than 1 μT when operated at or near its peak sensitivity. In addition, an appropriate procedure for preconditioning the GMI wire is developed to achieve sensor repeatability. Furthermore, using the identified optimum geometry of the experimental setup, the proposed sensor is implemented in monitoring the internal state of two types of Li-ion cells used in electric vehicles (EVs). The initial characterization results confirm that the GMI-IDT sensor can be used to directly monitor the charge capacity of the investigated Li-ion batteries. Other possible applications also include energy storage for renewable energy sources, and portable electronic device.

ACKNOWLEDGEMENTS

Akila Khatun, B.Sc., M. Sc.

First and foremost, I would like to express my gratitude to the Almighty without whom nothing is possible. No doubt, this is the most challenging journey that I have undertaken. I have learned lifetime lessons that humbled me and taught me the power of patience and perseverance.

I would like to express my sincere gratitude to my supervisor Dr. Fabien Josse for his guidance and encouragement throughout the completion of this work. I thank him deeply for giving me timely guidance, advice, and encouragement on technical aspects, writing style, and presentation skills in this work. My gratitude is also due to Dr. Florian Bender for his time, guidance, and helpful discussions throughout this journey. I would also like to extend my appreciation to Dr. Arnold Mensah-Brown for his suggestions, guidance and help during this work. My sincere gratitude also goes to my entire dissertation committee including Dr. Susan Schneider and Dr. Edwin Yaz for reading, reviewing, correcting, and making constructive suggestions on how to improve this dissertation. My sincere gratitude goes to Dr. James Richie and Mr. Dyche Anderson of Ford Motor Co. for their timely guidance, advice, and suggestions. I would like to express my gratitude to Dr. Raymond Fournelle for his help in equipment training. I also would like to acknowledge my former and present fellow students in the Microsensors Research Laboratory and Department of Electrical and Computer Engineering (Karthick Sothivelr, Sakin Satter, Nicholas Post, Jeffery Josse, Rafee Mahbub).

Finally, a debt of gratitude and love goes to my parents, my brothers, my sister, and her family. I thank them all for putting up with me and always encouraged me to continue in my academic career. Without their encouragement and support, I could not have made it this far. I would like to take this opportunity to express my thanks to my close friends for their love, support, and understanding for every moment during the ups and downs of this work.

This project was supported in part by a University Research Project Grant from Ford Motor Company.

TABLE OF CONTENTS

LIST OF TABLES

LIST OF FIGURES

1. INTRODUCTION

1.1 General Background

Energy conversion and storage units play an important role in almost all electronic systems and devices. Electrochemical energy storage systems, specifically rechargeable batteries are attracting attention since they can be used as secondary energy storage systems in various ways. They can be used or discharged essentially like a primary battery but recharged after use instead of being discarded, thus saving costs. In contrast to a primary battery, they can also be used as an energy-storage device electrically connected to and charged through a primary energy source, releasing this energy to the load on demand. Although compared to primary batteries, rechargeable batteries have lower power densities, they attract growing interest in portable electronic devices such as laptops, mobile phones, iPods, digital cameras, tablets, toys, etc. as well as in motorized vehicles such as hybrid or fully electric cars, airplanes, electric bicycles, electric motorcycles, etc.

Commonly used rechargeable batteries are lead-acid, nickel-cadmium (NiCd), nickel-metal hydride (NiMH), lithium-ion (Li-ion), etc. Among them, the Li-ion battery is a promising power source due to its high capacity, high specific energy density, wide operating temperature range, high unit cell voltage, relatively fast charging time, lower self-discharge rate, longer life span, etc. [1] . Moreover, with the continuous development of novel electrode materials, separator, and electrolyte performance, the manufacturing process has made Li-ion batteries more adaptable in various fields and the demand for Li-ion batteries has increased massively. Specifically, for some applications

such as the automotive industry, electric vehicle (EV), aircraft systems, industrial truck, etc. Li-ion batteries outperform other types of secondary batteries. Essential requirements for these applications are high energy density to provide an adequate driving range, low initial and operating cost, and long-life cycle to keep the cost and frequency of battery replacement low. However, developing techniques to cost-effectively monitor, manage, and predict important performance measures of rechargeable batteries remains a key technical challenge, which usually demands an appropriately designed battery management system (BMS).

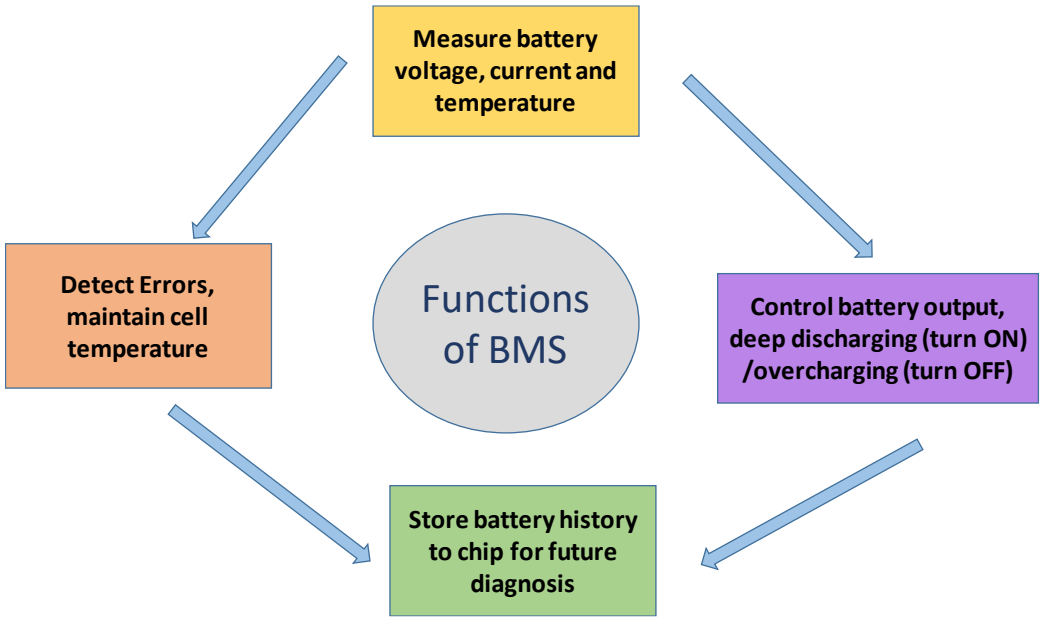

Figure 1.1: Major functions of a BMS

A BMS is an embedded system that uses a combination of hardware and software components to enable the proper use of battery systems in specific applications [2] . The major functions of BMS are to monitor and regulate different parameters of charging and

discharging of batteries as shown in Fig 1.1. [2] , [3] . The battery characteristics to be monitored includes the detection of unsafe operating conditions and communicate with the operator; detection of the section where failures occur and isolate the failing components from the rest of the battery pack. Moreover, coordination between the load and power sources are crucial, to ensure that the battery pack will not be overcharged or over-discharged. In addition to this, the BMS also ensures that the battery is kept within its designed operating temperature range to prevent damage from excessive heating, while continuously monitoring the remaining charge capacity, the battery state of charge (SOC) and state of health (SOH) [3] , [4] . Conventional low-cost rechargeable batteries have few protective features, thus a lack of flexibility, reliability, and protection. In contrast, a properly designed BMS can provide all the safety features required for the application of any sophisticated battery-based system, where information about the available power and estimation of the remaining charge are important issues [3] . Such applications include hybrid electric vehicles (HEV), battery electric vehicles (BEVs), plug-in hybrid electric vehicle (PHEV), energy storage for renewable energy sources, and consumer portable electronics, etc. where many difficult and precise requirements are imposed on the battery cells. As a result, the above requirements demand an advanced BMS. Performance measures that must be monitored in BMS include the state of charge (SOC), state of health (SOH), and charge capacity, which are commonly obtained by measuring battery variables such as battery voltage, current, and temperature [5] .

SOC is defined as the level of charge of a battery, which is expressed as a percentage of its present maximum charge capacity. Generally, the value of the SOC varies between 0% and 100%. If a battery is fully charged, then the cell is said to be at its

100% SOC level, whereas a completely discharged cell indicates a SOC of 0%. When a cell starts aging, the maximum charge capacity starts decreasing. For example, a 100% SOC for an aged cell would be equivalent to 75% - 80% of a new cell [5] . Battery charge capacity is a measure of the charge stored by the battery and is typically expressed in Amp-hour or Ah. It represents the maximum amount of energy that can be extracted from the battery under a specified charge/discharge current. Similar to the fuel gauge sensor used in conventional vehicles, battery charge capacity indicates the remaining energy left in the battery. Therefore, knowledge of the accurate charge capacity and SOC of the battery is very important because it allows estimating the remaining range (traveling distance) of an EV from the available charge capacity of the battery. However, it is important to recall again that the available charge capacity is a function of the battery age. Thus, knowing the current charge capacity gives the user an indication of how long a battery will continue to perform before it needs to be recharged. In addition, to deliver and accept charging without the risk of over-discharge or overcharge of the cell it is important to keep the batteries in a specified SOC range [5] , [6] .

SOH, on the other hand, is a relative measure that indicates the general condition of a battery and its ability to deliver the specified performance compared to the fresh battery. It is a measure of the long-term capability of the battery and reflects how much charge capacity of the battery has been lost and how much is left. The purpose of measuring SOH is similar to the automotive odometer display, which indicates the number of miles traveled since the vehicle was new [7] . Although there is no specific definition for SOH during the lifetime of a battery, the performance or “health” will be likely to decline slowly due to irreversible physical and chemical changes during usage,

and with time the battery will become unusable or dead. Any parameters which change significantly with age, such as loss of rated capacity or increased temperature rise during operation or change in internal battery resistance could be an indication of a change in SOH [7] . SOH represents the long-term capability of the battery whereas SOC describes its short-term capability. However, it is possible to extract SOH by long term recording of SOC parameters, specifically, voltage, current, and temperature, for the number of charge/discharge cycles completed by the battery, and by estimating the magnitude of the deviation from the new to present situation [1] , [2] .

Generally, a BMS for rechargeable batteries is incorporated with a model that considers the factors that can be used to infer SOC and SOH performance. Typical input parameters to the model include voltage, current, and temperature data, which are obtained from the respective sensors. These data are stored on a chip and can be downloaded and processed when required [5] . There are different techniques for data acquisition and processing of battery internal state parameters, which will be discussed in the following section. Compared to other types of rechargeable batteries, Li-ion batteries have been accepted and widely implemented in electronic products and are considered the main power source for electric vehicles [3] . In terms of energy density, power capability, lifetime, and cost for the PHEV and EV applications, the Li-ion battery technology is dominant over other types of battery technologies. An estimated price of less than $250 per kWh battery level is predicted for Li-ion batteries, which reduce the cost of energy in automotive applications dramatically [3] . However, one major drawback of Li-ion batteries is that they are very sensitive to overcharging and deep discharging, which can lead to accelerated aging of the battery or even serious defects

including battery fires [1] . To overcome these challenges, the Li-ion battery requires a special protection circuit that maintains the voltage and current within safe limits. Furthermore, the difficulty in accurately measuring SOC is always a major issue in improving the BMS for Li-ion battery-based systems. The most common widely used approach to SOC measurement is voltage based SOC measurement of a Li-ion battery during charging and discharging. They are easy to use and fast in computation, but the accuracy of the method highly relies on the performance of the sensors (voltage, current, and temperature) used in the measurements [6] . Due to the lack of a sensor which can measure the electrochemical phenomena inside the cell, this method may have a large error due to uncertainties and disturbances in sensor measurements. Moreover, the flat discharge voltage curve of Li-manganese, Li-iron-phosphate, and NMC batteries makes the voltage method impractical [1] , [2] .

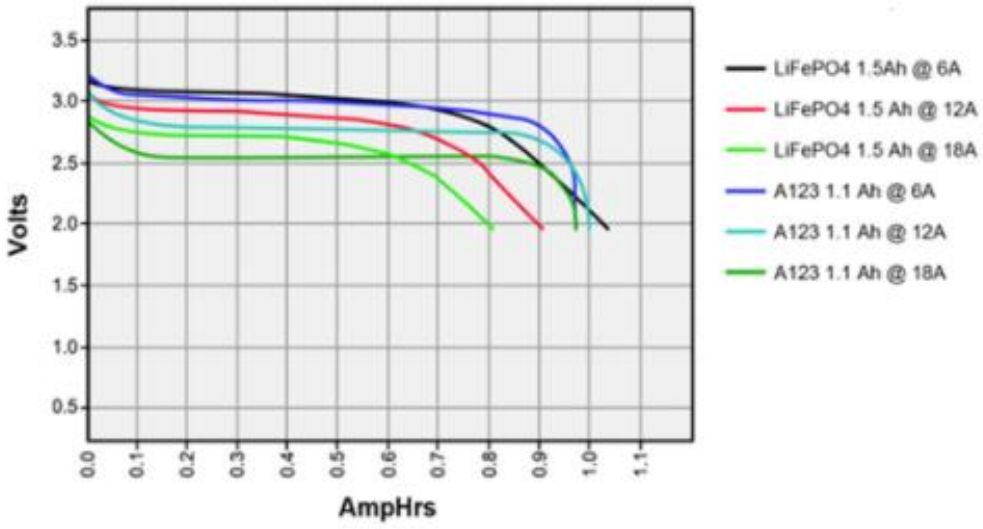

Figure 1.2: Sample voltage profiles for Li ion batteries [6]

Fig 1.2 shows the flat voltage profile of the two most common types of $LiFePO_4$ batteries: commercial $LiFePO_4$ battery by the manufacturer A123 and pure $LiFePO_4$ battery, at different discharging rates [6] . Note that the middle part of the profile is very flat, which makes SOC estimation based on the measured voltage inaccurate. For example, for the A123 1.1 Ah battery at 18A discharge rate, the change in voltage for a change in capacity from 0.1 Ah to 0.9 Ah is very small, which leads to a chance of inaccurate SOC estimation [6] . There are several advanced techniques used to estimate the SOC. Also, research is ongoing to improve SOC measurement techniques. Some of these techniques will be discussed in the next section.

1.2 Review of State-of-the-Art Monitoring Techniques of Li-ion Batteries

From the previous section, it is obvious that the BMS plays a major role in implementing and using rechargeable batteries in various applications. The main purpose of the BMS is to monitor the safety, reliability, and charge capacity of the battery typically by measuring SOC and SOH. Present measuring techniques of SOC and SOH are mostly non-invasive and involve an indirect approach based on estimation theory [2] . However, direct measurement of internal physical parameters is also explored using different sensor technologies [18] , [22] . In this section, a review of battery internal state monitoring techniques will be given. Depending on the technology, three types of battery internal state monitoring procedures will be reviewed, specifically, estimation technique, physical technique, and direct technique.

1.2.1 Estimation Technique

The estimation technique is an indirect way to estimate battery SOC by measuring battery variables such as time-varying voltage and the charging/discharging current. SOC

estimation using this technique has drawn the attention of many researchers and there have been various SOC and SOH estimation methods as shown in Fig.1.3 [8] .

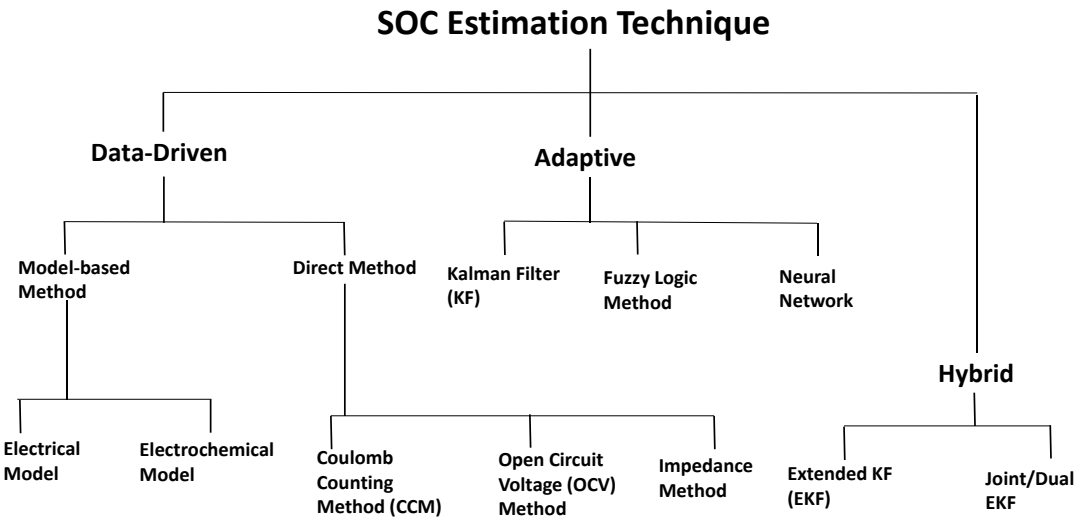

Figure 1.3: Various SOC estimation methods [8]

The existing SOC estimation methods are divided into three types: data-driven method, adaptive method, and hybrid methods [7] . The data-driven method can be divided into two categories: model-based method and direct measurement. Model-based methods utilize a battery model with advanced algorithms to estimate the states of a battery from its measured parameters. The measured parameters such as voltage, current, and temperature are used as input in either the electrical or electrochemical model to calculate the output or SOC [9] , [10] . Both models used in this approach have serious drawbacks. The model parameters can only be valid for new batteries, as any electrochemical changes that the batteries may undergo over time are not considered. The overall approach is costly to implement, computationally time-consuming, and not

practical. These models are used to a limited extent in the online estimation and control framework [8] .

The direct measurement approach generally are three types: coulomb counting method (CCM), open-circuit voltage (OCV) method, and impedance method. The CCM is performed by measuring the charge and discharge current time integral to obtain an estimated SOC value. A disadvantage of CCM is that the initial SOC value needs to be known. If the initial SOC value is inaccurate, it will lead to errors in the entire estimation process [11] . Also, the measurement of battery current from the current sensor output usually contains measurement errors and measurement noise that led to inaccuracy in estimation. In the OCV method, the cell voltage is continuously measured and SOC is estimated from the OCV curve by either a direct OCV curve inversion method or a cell-model based method [12] , [13] . One major drawback of the OCV method is that the battery needs a long resting time to reach equilibrium and to arrive at OCV. As a result, this method is not applicable in a real-time manner. Moreover, the fact that the OCV characteristics are different among cells could lead to inaccurate SOC measurements and it becomes less accurate if a battery has a relatively flat OCV-SOC curve such as that of commercial $LiFePO_4$ batteries [8] . Another type of direct measurement is the impedance method where the impedance spectrum of a battery can be computed by applying sinusoidal excitation at different excitation frequencies and analyzing the corresponding change in voltage and current, which is associated with the underlying electrochemical changes in the battery [14] . This estimation method is not suitable for inconsistently charged batteries; the batteries require identical charging conditions with a

constant current. Moreover, this method is highly sensitive to temperature and thus can only be used in the high-frequency range.

The adaptive method considers the self-designing effects such as chemical factors and provides an improved solution for SOC estimation with non-linear estimation theory, which can automatically adjust to time-varying systems [15] . The technique is a combination of a model-based approach and direct measurement. There are several adaptive methods for SOC estimation techniques that have been developed including the use of Extended Kalman filter (EKF), fuzzy logic, neural network, etc. The most widely used adaptive filter technique is the EKF and it is proven to be verifiable through real-time state estimation [15] . However, the accuracy and performance of this method highly depend on sensor precision, prior knowledge of the model, measurement noise covariance, and initial conditions. Moreover, numerical instabilities can occur due to complex matrix operations and linearization inaccuracy, and this makes the model harder to implement on hardware [8] . The fuzzy logic based SOC estimation method has potential for some portable devices where battery characteristics are static. However, the computational cost in this approach is very high and the model cannot consider the change in battery parameters over battery lifetime, thus leading to insufficient estimation accuracy [16] . The adaptive method based on a neural network approach has potential for small-scale operations but for large systems such as electric vehicles, it needs more neurons to increase model accuracy. Also, the network needs to be trained before use and it can be accurate for the new battery but not for an aged battery. Online training requires high computational effort, which brings various potential problems such as overfitting [17] .

The hybrid method permits a globally optimal estimation performance as it benefits from the advantages of each of the data driven and adaptive SOC estimation methods. In the extended Kalman filter (EKF) approach, a multiscale framework is proposed to estimate SOC and capacity [18] . The EKF method is easy to implement and considers the non-linear battery characteristics, which increase the accuracy of the model compared to other methods. Plett et al. developed and presented a complete model using the EKF method that provides a quantitative estimate of battery internal state [18] , [19] . EKF method achieves higher accuracy and efficiency than dual/joint EKF because the data used in the model are based on a valid cell dynamic model employing a hybrid of CCM and adaptive filtering technique.

1.2.2 Physical Technique

There are few physical techniques under investigation to monitor the internal state of the battery using various types of sensors including cell bulk force measurement, cell swelling measurement using strain or displacement sensor; use of ultrasonic transmission through the battery, etc. Because of the high demand for Li-ion batteries in electronic systems, most of the physical techniques were investigated for Li-ion batteries only. When Li-ion batteries are charged or discharged due to the intercalation and de-intercalation of the Li ions, a volumetric change occurs resulting in a change in bulk force or stress related to the expansion or contraction of the electrodes. Using this phenomenon, a model of the bulk force is employed for the Li-ion cells where a strain or displacement sensor is placed between the cells in a multi-cell battery pack. The sensor output is used to estimate SOC by different estimation techniques including the use of equivalent circuit models, moving horizon estimation (MHE) technique, etc. [20] , [21]

. Although the force measurement can improve direct SOC measurement significantly, one of the major drawbacks of this technique is that it does not consider the internal heat generated by the battery during high current operation, which introduces a major error in estimation.

L. Gold et al. [22] investigated another type of physical technique to measure SOC of a Li-ion battery by transmitting an ultrasonic wave through the battery. The change in amplitude of an ultrasonic pulse from the transmitter to receiver piezoelectric transducer is related to intercalation and deintercalation of lithium in the graphite electrode of the battery, which is also linearly related to the SOC [22] . The experimental setup using this method is costly and before implementation in BMS, several factors must be considered including long-term battery behavior, battery aging, temperature effect, etc.

1.2.3 Direct Technique

Several approaches are made to estimate the internal state of the battery directly. L.W. Sommer et al. [23] used fiber optic sensors placed externally onto Li-ion cells to monitor the change in strain signal due to excess volume change during charging and discharging similar to the bulk force measurement technique [23] . Although this approach seems promising, the lithium distribution around the electrodes is inhomogeneous and the change in volume is only substantial at a high SOC level.

Using a similar type of sensor, another type of direct measurement technique is investigated where fiber optic sensors are embedded within a Li-ion battery electrode stack during cell fabrication [24] . Compared to the externally attached fiber optic sensor approach, an increased signal is observed because error sources such as

environmental influences can be minimized in this approach. However, there is a practical limitation of this approach. Generally, to prevent swelling during battery operations (charging and/or discharging), Li-ion batteries are installed between compression plates or inside a rigid housing [25] . Using this geometry, embedded fibers could cause local stress and lead to serious defects in the battery. Also, embedding sensors during fabrication and monitoring sensor signals during operation are costly.

1.2.4 Challenges of Current Monitoring Techniques

The above-presented review indicates despite the many techniques and methods to estimate the SOC of the battery that have been investigated, accuracy and practicability of those techniques are still major challenges. Many factors play a role in the achievable accuracy and robustness of SOC measurements, which makes it difficult to enhance the effectiveness of the model without increasing complexity. Furthermore, the results obtained using current techniques give only an approximation of SOC and SOH leading to difficulties in charge balancing between the individual cells of a multi-cell battery pack. For these reasons, many battery systems are overdesigned to meet operational requirements in terms of cost, weight, and/or volume, which often increases the cost of the overall system. Therefore, there is a demand for a more accurate, properly designed battery model and measurement technique that makes it possible to monitor the change in battery dynamics in a real-time including battery aging and thermal behavior. This research proposed an alternative way of monitoring the battery internal state (charge capacity) by investigating the magnetic properties of the Li-ion batteries. Before discussing the principles of the proposed technique, it is important to first understand the

cell structure and chemistry as well as the electrode behavior during charging and discharging of a Li-ion battery.

1.3 Properties of Li-ion Batteries: Possibility of Magnetic Measurement of Battery Charge Capacity

Lithium-ion (Li-ion) batteries utilize lithium compounds as the positive electrode material. Li^+ ions are exchanged between the positive and negative electrodes upon charging and discharging. The positive electrode material is either of a lithium metal phosphate ($LiFePO_4$) or lithium metal oxide ($LiCoO_2$, $LiMn_2O_4$, $Li(NiMnCo)O_2$, etc.) usually having a layered structure. The negative electrode material is mostly graphite, which is also a layered material. During the charging or discharging process, the lithium ions are inserted or extracted from the interlayer space between atomic layers of the active materials [1] . The positive and negative electrodes are electrically isolated by microporous polyethylene or polypropylene separator films as shown in Fig. 1.4.

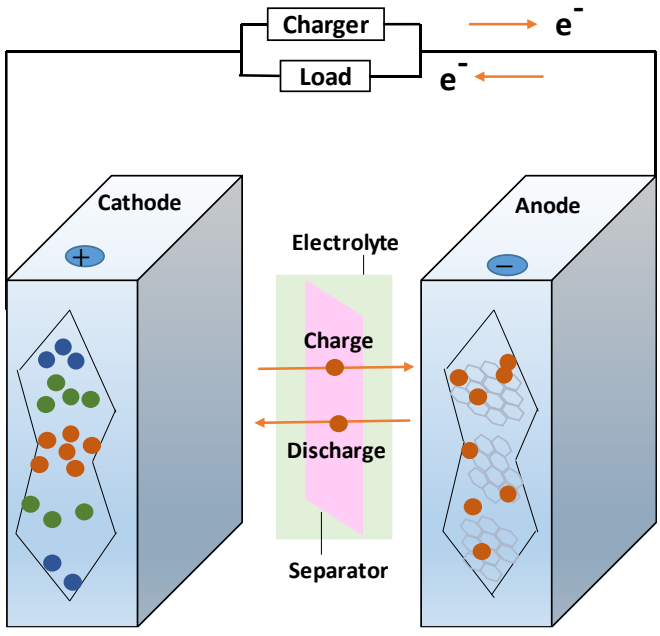

Figure 1.4: Schematic of Li-ion battery (• = Li^+ ion)

The electrochemical reaction of Li-ion batteries is similar to that of other types of rechargeable batteries. When the Li-ion cell is charged, the active positive electrode material is oxidized, and the active negative electrode material is reduced. In this process, lithium ions are deintercalated from the positive material and intercalated into the negative electrode material. The redox reaction is given below in Fig. 1.5:

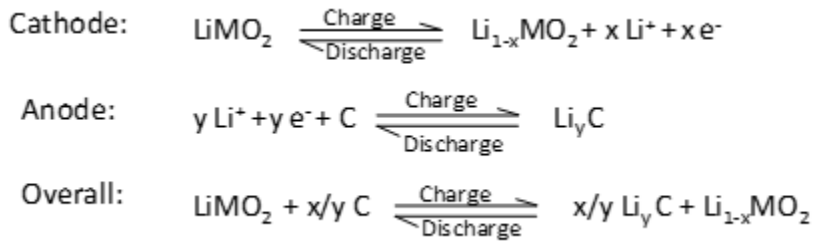

Figure 1.5: Redox reactions in the Li-ion cell [1]

where $LiMO_2$ represents the metal oxide of the positive electrode, for example, $LiCoO_2$, $LiMnO_4$, etc., C represents the carbon materials used in negative electrodes such as graphite and subscript x and y are selected depending on the molar capacities of the electrode materials for Li. From the above equations, it is observed that the Li present in the cell is not metallic, which makes the Li-ion batteries chemically less reactive, safe, and offers a longer life cycle than other types of rechargeable batteries [1] .

The performance of Li-ion batteries is mostly depending on the selection of electrode materials and the structure of electrodes. To provide high capacity, the positive electrode material must incorporate a large amount of lithium ions and they must be exchangeable during charging and discharging with little structural change. The positive electrode can be of three types: an ordered rock-salt, spinal type structure, or olivine type

structure [1] . The ordered rock-salt is basically a layered structure in which the lithium ions, transition metal atoms, and oxygen atoms are placed in alternate layers. An example is NMC type batteries used in hybrid vehicles. The spinal structure is a three-dimensional structure used in $LiMnO_2$, $(Mg/Fe)SiO_4$ batteries. The olivine type structure is also a three-dimensional structure based on PO_4 tetrahedra and FeO_6 octahedra commonly available for $LiFePO_4$ (LFP) batteries [1] . This work will focus on NMC and LFP type of Li-ion battery electrodes and their potential characteristics useful for magnetic measurements.

As mentioned earlier, in the NMC electrode materials the cations are distributed in the transition metal layers of the structure. On the other hand, in LFP batteries lithium ions are bonded with iron, phosphorus, and oxygen in a complex crystal structure. In both cases, during charging and discharging, the oxidation state and/or spin state of the transition metal atoms changes, resulting in a change in the magnetic moment of the atom. [26] , [27] . The change in the magnetic moment leads to a change in magnetic properties i.e., magnetic susceptibility of the electrode, which can be probed in the presence of a magnetic field. For a fully charged or discharged battery, this magnetic field can be sensed by a magnetic sensor and used as a baseline for analysis. As the battery charges or discharges, the magnetic field will be perturbed by the withdrawal or insertion of Li^+, allowing direct measurement of the degree of lithiation. The degree of lithiation is related to the degradation of the battery i.e., capacity loss, which is related to SOC of the battery.

Measurement of charge capacity based on magnetic susceptibility is a promising approach because it combines the advantages of noninvasive and relatively direct

measurement of active lithium-ion concentration of the battery. Kadyk et al. [26] describe this principle for the $LiFePO_4$ battery electrode where they found how the concentration of active lithium ions in $LiFePO_4$ battery electrodes is related to the change in magnetic susceptibility of the electrodes. The main reason is the presence of metal atoms in the positive electrode material: iron for the LFP battery, Co and/or Ni for the NMC battery. Depending on their oxidation state, these metal atoms can be ferromagnetic, ferrimagnetic, or paramagnetic, thus providing a rationale for measurement of battery charge capacity through magnetic susceptibility, which can be used to infer battery SOC [26] . Although the sensing principle will be described further for NMC and LFP type of Li-ion batteries, it may be used for measuring battery internal state of other types of batteries containing ferromagnetic electrode materials.

1.4 Problem Statement

As stated in the above sections, there is a growing need for complex systems of rechargeable batteries, e.g., in electric vehicles (EV), airplanes, energy storage for renewable energy sources, portable electronic devices, etc. Developing techniques to cost-effectively monitor, manage, and predict important performance measures such as present charge capacity, SOC and SOH of these batteries remains a key technological challenge. At present, commonly used measurement techniques of SOC are estimation techniques that represent indirect methods and do not consider the battery dynamics in a real-time manner. Some physical and direct methods of SOC measurement have been proposed. However, before any of these methods reaches the implementation and commercialization stage, various problems must be solved, which includes taking into

account environmental parameters (such as temperature) interfering with the measurements.

For these reasons, this research is aimed at improving the existing BMS for rechargeable batteries by introducing an alternative way of monitoring the internal state (charge capacity) of the battery based on the magnetic properties of the battery. In various theoretical work, it has been found that, for Li-ion batteries, the concentration of active lithium ions in the cathode electrodes is directly related to the change in magnetic susceptibility of the electrodes [26] . This opens a possibility of directly probing the internal state of the battery during charging and discharging by monitoring the change in magnetic susceptibility of Li-ion battery. However, until recently, there is still a lack of significant experimental work on this approach. Hu et al. [28] introduced the use of atomic magnetometers to map the magnetic susceptibility for Li-ion cells. Though this type of measurement technique provides precise information of the magnetic susceptibility of Li-ion batteries, it is applicable only when the battery is placed inside the meter but not in a continuous, real-time manner [28] . Using a type of sensor to measure the susceptibility-induced field surrounding a cell during charging or discharging would be a more direct, non-destructive, and non-invasive way to monitor the magnetic properties, hence the charge capacity of the battery. Furthermore, direct measurement of battery charge capacity will enable a more accurate determination of battery SOC and might have the potential to gain information about battery SOH from the long-term magnetic measurement of the battery.

In this work, efforts will be made to design a micromagnetic sensor for direct measurement of magnetic susceptibility of Li-ion battery electrodes, by combining

magnetically sensitive elements based on Giant Magnetoimpedance (GMI) effect with a single interdigital transducer (IDT) on a piezoelectric substrate. The proposed direct and non-invasive measurement of battery charge capacity will allow to accurately monitor the battery dynamics during charge and discharge conditions over a wide operating range particularly for multi-cell battery packs. In addition, using a type of sensor that can be operated wirelessly will eliminate the need for wiring, which is an important cost factor in multi-cell batteries. Furthermore, the use of a sensor technology that is suitable for sensor arrays will allow measuring charge capacity of individual battery cells or small groups of battery cells in battery packs, thus allowing for charge balancing between individual cells and for early identification of defective battery cells. Also, for improved measurement accuracy, the sensor should be suitable for operation over a wide temperature range (-40°C to 40°C).

1.5 Organization of the Dissertation

This dissertation is divided into six chapters; Chapter 1 introduces the importance of and demand for a properly designed BMS in the development of advanced electronic systems. Effective BMS requires precise measurement of battery parameters including SOC, SOH, and charge capacity, which are defined here. A brief review of current measurement techniques for SOC is given. Chapter 1 also reviews the drawbacks of the current techniques of SOC measurement that the dissertation is addressing, and the proposed technique and goal of this research are discussed as one possible solution to these drawbacks in the problem statement. In Chapter 2, a general review of the commonly used magnetic sensors is given. An introduction to the selected sensor platform – a single IDT deposited on a piezoelectric substrate is presented. More

specifically, the working principle and equivalent circuit model of the IDT is described to describe the principle of operation of the proposed sensor. In addition to this, the relevant theoretical background required for explaining the detailed modelling of the proposed sensor design is introduced. In Chapter 3, an investigation of magnetically sensitive elements for the proposed magnetic sensor design is presented. The focus of the work was narrowed to the analysis of magnetic sensor designs based on selected magnetostrictive thin film coated SAW devices and GMI wire integrated with an IDT on a piezoelectric substrate, respectively. The relevant theoretical background of magnetostrictive thin film-based sensor design is presented along with the design, characterization, and analysis of the thin film coated magnetic sensor. In the second part of this chapter, a detailed review of the Giant Magnetoimpedance (GMI) effect is given together with a description of different types of GMI elements. The chapter ends with a detailed discussion on the underlying physics behind the distinctive properties and characteristics of the GMI microwires. In Chapter 4, detailed modeling of the proposed GMI-IDT sensor design and a strategy to modify the sensor parameters are presented. The design parameters of the GMI-IDT sensors that were used to collect the data analyzed in this dissertation are discussed. In addition to this, the equipment, materials, experimental procedures, and experimental setup used in this work are presented. In Chapter 5, results on the experimental characterization of the designed GMI-IDT magnetic sensor are shown. An effective pre-conditioning method adopted for the proposed sensor design is discussed. Furthermore, measurement results using the GMI-IDT sensor for actual EV type Li-ion battery measurement are given. A comparative analysis of the proposed technique of battery internal state monitoring with the state of

the art is presented followed with a discussion of the observed and measured sensor responses. Finally, Chapter 6 provides a summary and conclusion of the work performed in this dissertation and provides some suggestions regarding possible extensions of this work for future research in this field.

2. MAGNETIC SENSORS AND SENSOR PLATFORMS

2.1 Magnetic Sensors: General Background

Magnetic sensors play an important role in a variety of fields in engineering and industrial sectors, including medical, automobile, military and security, mining, meteorological, archeological, and geological applications. A magnetic sensor detects the changes and disturbances in a magnetic field such as flux density, field strength, and field direction [29] . The characteristics of a magnetic sensor are strongly dependent upon the requirements of the application. However, regardless of the application, the key characteristics that a magnetic sensor must exhibit include:

- Sensitivity: defines the change in the measurement (output) signal per unit change in input signal [30] . Note that the sensitivity of a magnetic sensor is not necessarily constant throughout the entire range of the input signal [29] .
- Selectivity: describes the ability of a sensor to distinguish between the measured magnetic field and other interfering fields or parameters [30] . For magnetic sensors, separating the sensor response from any other background magnetic field or geomagnetic field is crucial.
- Detection limit: the smallest quantity of magnetic field that a magnetic sensor can reliably detect. 'Reliably' here refers to an adequate signal to noise ratio (typically, a signal greater than three times the RMS noise) [30] .
- Dynamic range: magnetic field strength that the magnetic sensor can detect. Changes in magnetic field values outside this field range may be unmeasurable by the sensor [30] .

- Stability: the ability of the magnetic sensor to produce the same output value with respect to the input signal over a period of time [30] .
- Repeatability: magnetic sensor's ability to produce the same output for successive measurements under the same measurement conditions [30] .
- Reproducibility: ability to reproduce the same output responses using the same method after some measurement condition has been altered [30] .

Magnetic sensors can be implemented using a range of different techniques depending on the applications. Those include induction sensors, Hall effect sensors, magnetoresistor sensors, magnetoimpedance sensors, inductive coils, fluxgate devices, superconducting quantum interference device (SQUID), etc. Hall devices are the most extensively used magnetic sensors in a wide range of applications such as proximity sensors, switches, wheel speed sensors, position sensors, pressure sensors, flow sensors, current sensors, etc. [32] . The Hall effect sensor is based on the Hall effect principle, which states that when a current-carrying (semi)conductor is exposed to a magnetic field, the charge carriers of the semiconductor experience a force in a direction perpendicular to the magnetic field and current; and produce a voltage called Hall voltage. The output (voltage) of the Hall effect sensor is proportional to the magnetic field intensity applied to it [29] , [32] . Although Hall devices are fully compatible with microelectronics, they have limited sensitivity due to the limitations of semiconductor materials. In addition, they have a low signal to noise ratio and relatively large offset, lack of long-term stability, etc. [29] , [31] , [32] . Magnetoresistors are another type of commonly used magnetic sensor. Magnetoresistors are resistors whose resistance changes in the presence of a magnetic field. They can be based on either thin ferromagnetic films or

semiconductor materials. Compared to other magnetic sensors, magnetoresistors have high sensitivity in low magnetic fields but they have disadvantages including flipping effect, hysteresis, temperature drift, external magnetic interferences, etc. [29] , [31] .

Inductive coils or search-coil magnetometers are another type of commonly used magnetic sensor based on Faraday's laws of induction. The sensor consists of a ferromagnetic rod which is inserted inside a coil [29] . When the coil is placed in a magnetic field the magnetic flux across the coil changes and produces a voltage proportional to the rate of change in flux. These devices are also known as proximity switches or proximity sensors and are used to detect the presence and localized defects of metallic targets. One major disadvantage of inductive coils is that miniaturization of coils is difficult, which limits the applications [29] , [32] . The fluxgate devices are highly sensitive magnetic sensors, which consist of a ferromagnetic core wrapped with two coils named primary or excitation coil and the secondary or pickup coil. The operating principle of fluxgate devices is based on modulation of the permeability of the soft magnetic core, which generates changes in the DC flux of the pickup coil. When an AC current is applied to the primary coil the permeability of the core changes, which causes the core field to change thus inducing a voltage in the pickup coil [29] . Compared to other types of highly sensitive magnetic sensors such as SQUIDs, fluxgates are inexpensive, but they are limited by offset noise, low magnetic permeability of the ferromagnetic cores, are difficult to miniaturize due to the three-dimensional structure of the coils, and consume high power, etc. [29] , [32] . Other types of well-known magnetic sensors include SQUID, giant magneto resistive (GMR), anisotropic magneto resistive (AMR), etc. and are described in detail in the literature [29] , [33] .

In recent years, compared to conventional magnetic sensors, a trend towards highly sensitive, miniaturized magnetic sensors with low power consumption has been observed. Depending on the application, it is often necessary to develop an appropriate sensing platform and technology to design and implement a magnetic sensor with the required specifications. As mentioned in chapter one the goal of this research is to design a micromagnetic sensor for direct and noninvasive measurement of the magnetic susceptibility of the Li-ion battery. The characteristics for the proposed sensor that are essential for this specific application include high sensitivity specifically in the low magnetic field region, and low power consumption. Furthermore, the sensor must be easy to miniaturize, and needs to be operated over a large temperature range, and must have the potential for passive interrogation for sensor arrays for multi-cell battery packs, etc. To achieve these sensor characteristics this work presents a promising design for a magnetic sensor that makes use of a combination of magnetically sensitive elements based on giant magnetoimpedance (GMI) effect and single interdigital transducers (IDTs) deposited onto a piezoelectric substrate. For the proposed sensor design, single IDTs are selected as a sensing platform because of various beneficial features compared to other sensing platforms, which will be discussed in the following sections.

2.2 Interdigital Transducers (IDT) on Piezoelectric Substrate: A Review

Interdigital transducers (IDT) are well known for their extensive use in acoustic wave device sensors and actuators, medical instruments, oscillators, delay lines, and filter design [35] , [36] . If deposited on a piezoelectric substrate, the IDT allows for efficient transduction of electrical energy to acoustic energy. The IDT consists of a series of interleaved electrode fingers made from a metal film deposited on a piezoelectric

substrate. An ac voltage applied to the electrodes results in generation of an acoustic wave in the substrate material due to the piezoelectric effect. If the frequency of the ac voltage is selected such that the wavelength of the acoustic wave is equal to the periodicity of the transducer, there is strong piezoelectric coupling. Because of the piezoelectric effect, the stress pattern excited by the transducer corresponds to the sum of the stress of the two oppositely traveling acoustic waves, resulting in a standing-wave stress pattern [37] . Conversely, the piezoelectric effect can work to convert a mechanical wave back into an electrical field [34] , [37] . One type of mechanical wave that can be generated using the piezoelectric effect is the Rayleigh wave, also known as surface acoustic wave (SAW) since the acoustic wave is traveling along the surface of a solids [34] , [37] .

IDTs, shown in Fig 2.1 (a) in a delay line configuration, are used in many acoustic wave devices. The delay line has two IDTs, where the input IDT will convert an electrical signal into an acoustic wave launched in the direction of the output IDT. The output IDT will then convert the acoustic wave back into an electrical signal for analysis. The changes in the properties of the wave resulting from perturbations along the delay line are measured and used as a sensing mechanism [34] , [36] .

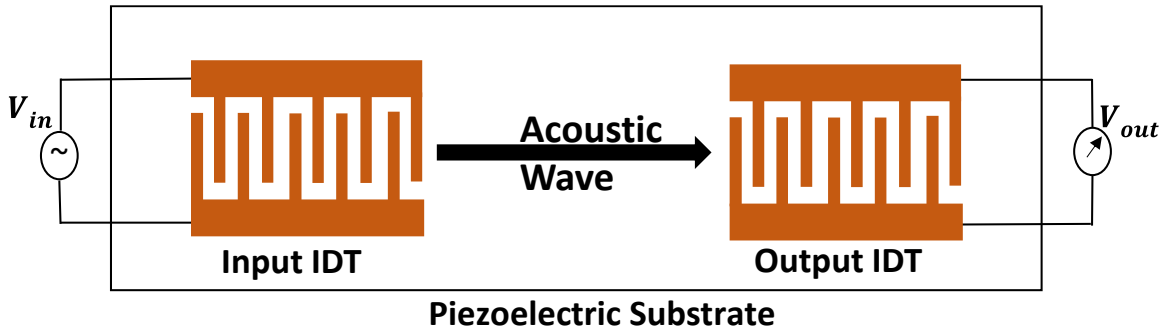

(a)

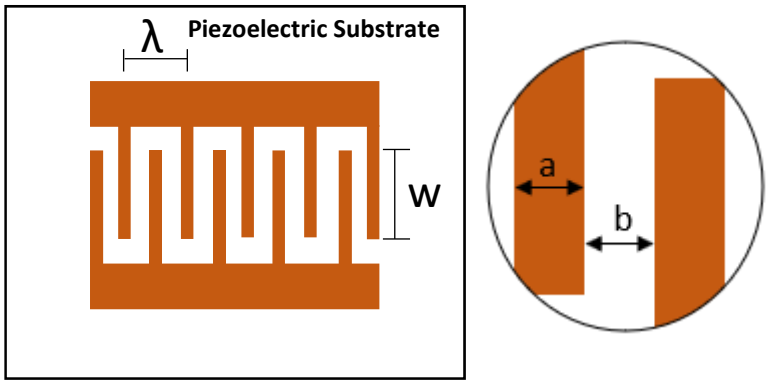

(b)

Figure 2.1: Schematic representation of (a) an acoustic wave device (b) an IDT

Fig 2.1 (b) shows a detailed representation of an IDT [34] , [11] . The transducer is considered to have N finger pairs with period length λ. The width of each electrode is represented as a and the gap width between the IDT fingers is b. The period length (for single-electrode IDTs) is $\lambda = 2a + 2b$. The aperture, W, is the length of finger overlap. The thickness of the electrode is negligibly small. The relationship between the electrode width and the electrode gap width is given by the metallization ratio, $\alpha = a/(a+b)$; it varies from 0 to 1 and is 0.5 for the uniform IDT case. By changing the

length, width, position, and thickness of the IDT, the performance of the device can be modified and controlled [39] , [40] .

Instead of using the perturbation of the acoustic wave for sensing [34] , [37] , the IDT itself can be perturbed by adding discrete circuit elements to modify the transduction process. This approach is taken in this work as described in section 2.3. IDTs are typically deposited on different single crystal piezoelectric substrate materials including quartz (α-SiO_2), lithium tantalate ($LiTaO_3$), and lithium niobate ($LiNbO_3$). Depending on the material type and crystal cut angle, the properties of the devices may vary including cost, acoustic-wave attenuation, propagation velocity, temperature dependence of the velocity, etc. [34] , [36] . For the proposed sensor design IDTs deposited on a $LiTaO_3$ substrate are selected because this substrate material has high coupling coefficient, k^2 which is a measure of the efficiency at which the electric fields are converted into mechanical stress fields [34] , [38] , [39] .

To describe the IDT, a simplified equivalent circuit model will be used where the transducers are considered as an array of sources with each source acting as a piezoelectric plate transducer for generating bulk waves. Using this model, the significant properties of the IDT can be obtained [39] , [41] .

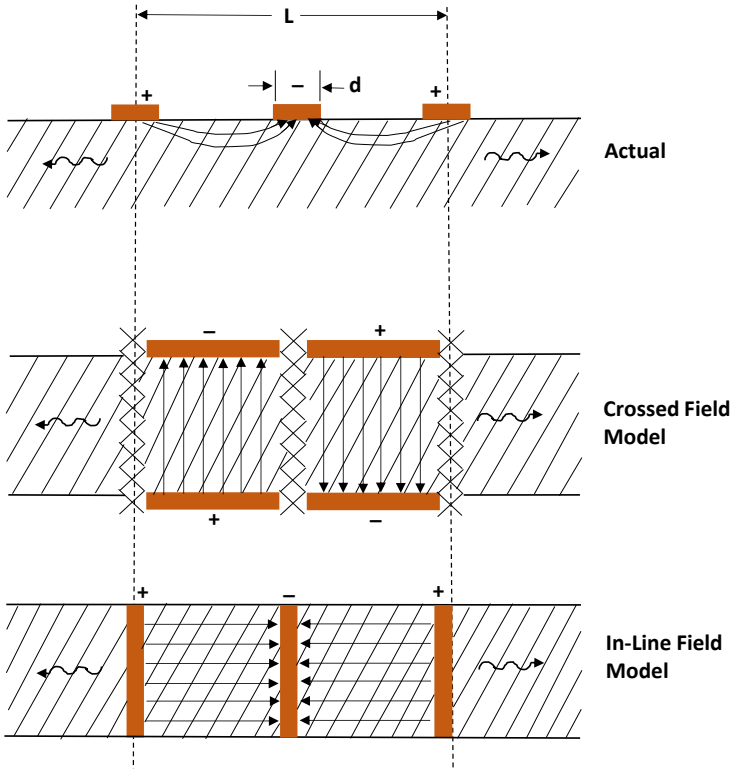

Figure 2.2: Side view of the IDT: field patterns for (a) actual device, (b) crossed field model, and (c) in-line model [39] , [41] .

By analyzing the parallel and perpendicular components of the electric field pattern, the electric field approximation can be represented by either of two models named crossed field, or in-line model as shown in Fig 2.2 (b) and Fig 2.2 (c). Generally, the electric field patterns are a combination of the two as shown in Fig 2.2 (a) [39] . In the cross-field model, the applied electric field is normal to the acoustic propagation vector. In the in-line model, the electric field and propagation vector are parallel to each other. It has been shown that materials with high piezoelectric coupling such as $LiTaO_3$ and $LiNbO_3$ are better represented by the crossed field model [39] , [41] . Therefore, the crossed field model will be used here.

Considering the symmetry and periodicity of the IDT finger pairs, maximum acoustic response occurs for frequencies at or near the IDT synchronous frequency $\omega_0 = 2\pi f_0$, where $f_0 = v/L$; v is the acoustic velocity and L is the periodicity of the electrodes [39] . For the crossed-field model, the input immittance of the IDT can be characterized by a circuit consisting of the total electrode capacitance in parallel with a radiation immittance as shown in Fig 2.3 [39] , [41] .

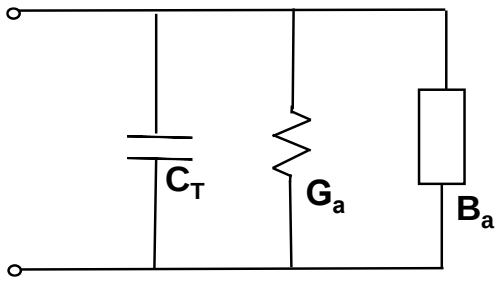

Figure 2.3: Crossed field model (parallel circuit representation) of IDT [39]

For the crossed field model, the IDT admittance at the synchronous frequency is given by [39]

$$Y_t = G_a + j\omega_0 C_T \tag{2.2}$$

where, G_a is the radiation conductance, and C_T is the electroacoustic capacitance between the finger pairs. Note that, the radiation susceptance B_a is a measure of how much stress is out of phase with the motion of the wave and it is zero when the IDT is operated at or near the synchronous frequency, ω_0 [39] . For the crossed field model, at ω_0 the radiation conductance, G_a, is maximum because all the stress contributions are in phase with each other. As the frequency deviates from the ω_0, the magnitude of the susceptance B_a begins to increase resulting in a decrease in radiation conductance G_a [39] - [41] .

2.3 Analysis of Impedance Loaded Single IDT Model: A Review

In this research, the single IDT of an acoustic wave device is investigated as the sensing platform for the proposed micromagnetic sensor design. Generally, for IDTs the forward and backward surface waves are regenerated by the voltage that the incident surface wave delivers to the electric load in the transducer. By varying the load impedance, the magnitude of the regenerated surface waves can be reduced, which leads to a change in the insertion loss [42] . Typically, regenerated acoustic waves can introduce multiple transit echoes and are therefore unwanted; as a result, they are eliminated by using a perfectly matched network to the IDTs. However, by replacing the matching network with a load with varying impedance that depends on the parameter to be measured, the transduction process hence insertion loss or return loss of the IDT can thus be used as a sensing parameter. This technique is used in our proposed magnetic sensor design where a magnetically sensitive element is included as a shunt-load to the single IDT [42] , [43] .

When the magnetically sensitive element responds to a magnetic field, its properties (e.g., impedance, permeability etc.) undergo changes resulting in a change in the transduction process of the IDT due to the impedance mismatch between the two sensor elements. In order to present this theory, a model must be first introduced that explains how the properties of the IDT change upon adding an impedance element [42] , [43] . Specifically, the effect on insertion loss characteristics of an impedance loaded single IDT will be explained. Fig 2.4 shows the equivalent circuit for an impedance loaded single IDT.

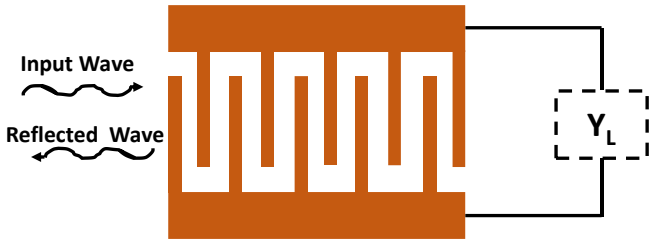

(a)

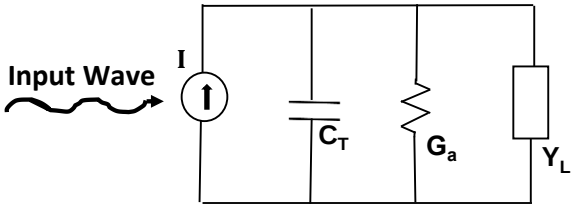

(b)

Figure 2.4: Equivalent circuit for an impedance loaded single IDT: (a) an IDT with load, (b) equivalent electrical circuit

Assuming there are no losses other than the 3 dB bidirectional losses, the electrical circuit shown in Fig 2.4 provides a basis for calculating the return loss of the circuit. For operation at the IDT synchronous frequency with a load, the return loss of the transducer is given by [42]

$$RL = -10\log_{10}\frac{\alpha^2 + {Q_L}^2(\alpha-1)^2}{(\alpha + Q_L Q_r)^2 + (Q_r + [1-\alpha]\,Q_L)^2} \tag{2.3}$$

where, the parameter Q_r is the transducer radiation i.e., the ratio of transducer capacitive susceptance to the synchronous acoustic radiation conductance, $Q_r = \omega C_T/G_a$. $Q_L = \omega C_T/Y_L$ is the variable load radiation, The parameter, α is zero for crossed field model. Equation 2.4 indicates that the return loss of the IDT can be modulated by changing the variable load. Generally, when IDTs are used in a delay line

configuration, there is a load attached to the IDT that acts as a matching circuit to maximize the acoustic radiation. Another purpose of the matching circuit is to eliminate or minimize the multiple transit echoes [42] , [43] . For the proposed magnetic sensor design, the single IDT of an acoustic wave device is shunt-loaded with a magnetically sensitive element, a GMI wire. The impedance of the GMI wire depends on the applied magnetic field and will influence the degree of matching or mismatching between the GMI wire and the IDT. This affects the signal reflected from the IDT, which therefore contains the sensing information as a change in return loss. The next chapter will introduce and explain the different properties and distinctive characteristics of the GMI wire. Based on the equivalent circuit model of the impedance loaded IDT as given here and the frequency-dependent impedance behavior of GMI wire, a detailed model of the proposed micromagnetic sensor will then be presented.

3. MAGNETICALLY SENSITIVE ELEMENT FOR MAGNETIC SENSOR DESIGN

3.1 Introduction

Magnetic sensor technologies have been discussed in the previous chapter. This chapter will focus on magnetically sensitive materials or elements that can be used in magnetic field sensors. The most familiar and simplest magnetically sensitive elements that can detect the changes of magnetic flux are coils and metal pieces used in induction sensors and fluxgate sensors. When a magnetic material is brought close to the coil or when a magnetic field is applied externally close to the metal piece, these coils or metal pieces are magnetized [31] . Other commonly used magnetically sensitive elements are thin film semiconductors used in Hall effect magnetic sensors, thin film magnetoresistive (ferromagnetic) elements used in magnetoresistive sensors, superconducting materials used in SQUID magnetometers, thin film composite layers used in MEMS magnetic sensors, and magnetic tunnel junction sensors, etc. [31] .

In past years, extensive research efforts have been made on different kinds of thin film magnetic sensors based on the magnetostrictive effect. The magnetostrictive effect (also referred to as the magnetoelastic effect) present in magnetic materials causes the materials to change their shape or dimensions (expand or shrink) as an external magnetic field is applied. Conversely, when stress is applied to the magnetostrictive materials, the magnetic anisotropy will change as a result. Generally, materials with high permeability and high Young's modulus (high longitudinal strain) exhibit this effect, including metals (Iron, Nickel, Cobalt), metal alloys (FeNi, FeCo), etc. [44] , [45] . Depending on the sensing platform, the selection of appropriate magnetostrictive material plays a key role

in the performance of a magnetic sensor. A range of acoustic wave devices has been studied as sensing platforms in combination with different magnetostrictive films. Ganguly et al. proposed a magnetically tuned SAW phase shifter using a Nickel coated SAW delay line [44] . Tong et al. developed a magnetostrictive FeNi coated SAW-based current sensor [45] . A magnetostrictive FeCo coated SAW magnetic/current sensor was proposed by Wang et al. [46] . Li et al. reported an integrated SAW sensor that can measure the magnetic field, temperature, and humidity and is fabricated by depositing NiFe/Cu tri-layer composite film on a reflector type SAW device [47] . From the above literature reviews, it has been shown that by proper selection and deposition of a magnetostrictive thin film onto the SAW sensing platform, it is possible to design an appropriate magnetic field sensor. Therefore, this work investigates several magnetostrictive thin films that are deposited onto SAW devices for magnetic field detection.

3.2 Principle of Magnetostrictive Film-based SAW Devices: A Review

The sensing mechanism of the magnetostrictive coated SAW device depends on the magneto-mechanical nature of the selected coating. The coating produces a strain under the magnetic field generated by the applied current. In a delay line configuration of the SAW device, the coating is deposited on the propagation path of the acoustic wave. With the presence of the magnetic field, due to the magnetoelastic nature of the material, the Young's modulus of the film changes, which results in a change in the SAW propagation characteristics in the form of a velocity or frequency shift [44] - [46] .

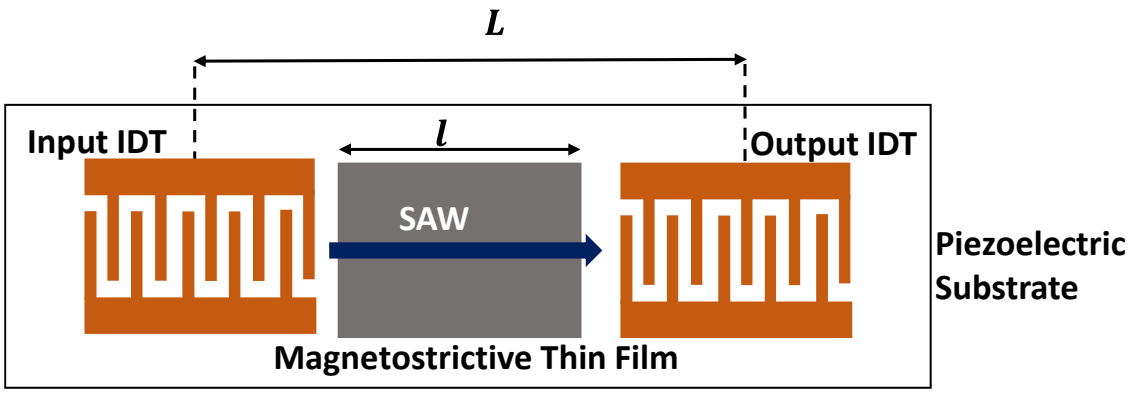

Figure 3.1: Schematic diagram of magnetostrictive film coated SAW Device

Fig. 3.1 shows the schematic diagram of a magnetostrictive film coated SAW device. When the film is rigidly bonded to the surface of the piezoelectric substrate, any change or deformation of the film will perturb the propagating wave velocity. Experimentally, frequency change is measured instead of velocity change because any fractional change in velocity response is proportional to the fractional change in frequency provided that there is no dispersion of the wave. The relation between the change in velocity and frequency shift can be written as [48] , [49]

$$\frac{\Delta f}{f} = \frac{l}{L}\frac{\Delta v}{v} \tag{3.1}$$

Depending on the properties of the coating, the fractional change in velocity, Δv can be described by using the well-known perturbation theory. Perturbation theory describes the interaction between the coating and acoustic waves. Small changes in wave velocity and attenuation can be written as a sum of the partial derivatives and can be expressed as [48] , [49]

$$\Delta v = \frac{\partial v}{\partial m}\Delta m + \frac{\partial v}{\partial c}\Delta c + \frac{\partial v}{\partial \varepsilon}\Delta \varepsilon + \frac{\partial v}{\partial \sigma}\Delta \sigma + \frac{\partial v}{\partial T}\Delta T + \frac{\partial v}{\partial P}\Delta P \tag{3.2}$$

$$\Delta\alpha = \frac{\partial\alpha}{\partial c}\Delta c + \frac{\partial\alpha}{\partial\varepsilon}\Delta\varepsilon + \frac{\partial\alpha}{\partial\sigma}\Delta\sigma + \frac{\partial\alpha}{\partial T}\Delta T + \frac{\partial\alpha}{\partial P}\Delta P \quad (3.3)$$

Equation (3.2) indicates that changes in wave velocity (Δv) can be related to changes in coating mass (m), viscoelastic constant (c), dielectric constant (ε), conductivity (σ), temperature (T), and pressure (P). On the other hand, change in wave attenuation, ($\Delta\alpha$), depends merely on viscoelastic and dielectric constants, conductivity, temperature, and pressure change [49] . Note that the metal (Au, Ni or NiFe) film on the delay line will minimize the effect of any electric field on the SAW. Other environmental effects (e.g., temperature) can be eliminated using a dual delay line acoustic wave device design. Therefore, only the magnetostrictive sensing mechanism (dependence on Δc) will remain in the simplified form of equation (3.2) and (3.3). For the proposed magnetic sensor, the change in shear modulus, $G = G' + jG''$, (with shear storage, G' and shear loss, G'') of the coating due to an applied magnetic field needs to be considered. Since magnetostrictive metal films possess very high stiffness, the change in acoustic loss modulus G'' has a negligible effect on acoustic wave propagation and the change in wave velocity is depending on G' only [48] .

3.3 Design of Coated SAW Devices for Magnetic Sensing

The above indicates how the elastic properties of a ferromagnetic material affect the velocity of the propagating acoustic wave. Materials with high magnetic permeability and high Young's modulus are good candidates for high dimensional changes as an external magnetic field is applied [50] .

Metal (Name)	Young's Modulus (GPa)	Boiling Point (K)	Maximum Magnetic Permeability	Magnetostrictive Properties (qualitative)
Iron	211	3135	5000	Low
Nickel	200	3005	600	High
Cobalt	209	3143	250	Very High

Table 3.1: Properties of common Ferromagnetic materials [50]

Among the most common ferromagnetic materials, while iron has a very high Young's modulus (hence high magnetic permeability), pure iron tends to oxidize rapidly and thus, is not appropriate for deposition. Compared to cobalt, nickel has high magnetic permeability, therefore, nickel and nickel-alloys were chosen as materials for deposition. We investigate two types of coatings (Ni and NiFe) deposited on the SAW devices at different film thicknesses. In the following sections, a detailed description of the investigation is given including some preliminary results.

3.3.1 Nickel-Coated SAW Device

In this work, nickel film was deposited onto the SAW device using thermal evaporation process. For this purpose, after performing the cleaning procedure (see materials and procedure section in chapter four), a SAW device is placed in the thermal evaporation chamber, which is then evacuated. During evaporation, the IDTs, contact pads, and other areas are masked carefully using Kapton tape.

There were several devices prepared with different coating thicknesses and configurations as follows:

- Device 1: 100nm nickel coated on one delay line, with the second delay line uncoated (with only the gold coating used to eliminate any electric field effect (see Fig. 3.2)
- Device 2: 100nm nickel coated on both delay lines
- Device 3: additional 1 µm PMMA (polymethyl methacrylate) layer (deposited using spin coater) on both delay lines as on device 1
- Device 4: 150nm nickel coating on one delay line, 50nm nickel coating on the second delay line

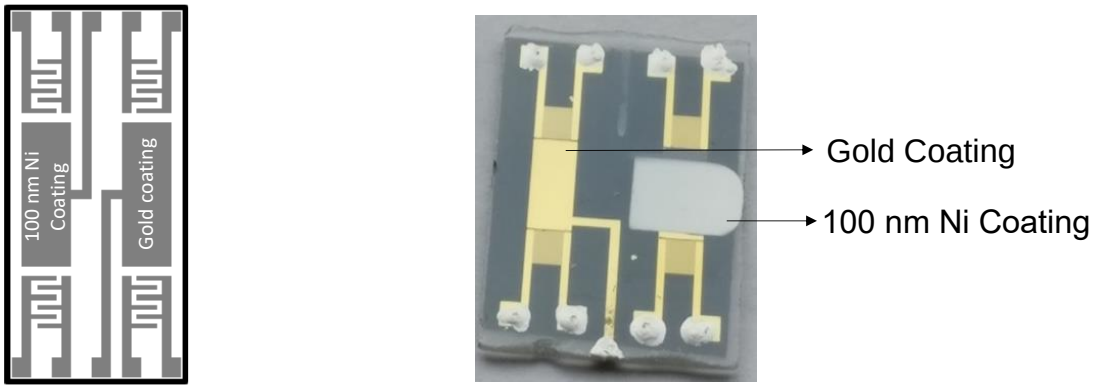

(3) **(b)**

Figure 3.2: Nickel coated SAW device 1 (a) schematic diagram (b) actual device

Fig 3.2 shows the Ni coated SAW device with 100 nm thickness. Device 1 was characterize using a differential measurement technique. Due to the magnetostrictive nature of the Ni coating, it is expected that the film should be sensitive to the magnetic field hence the velocity of the acoustic wave will be perturbed. Since gold is a diamagnetic material, the velocity of the acoustic wave on the gold- coated delay line will not be affected, thus enabling a differential measurement.

To characterize the device shown in Fig 3.2, two permanent magnets 30DNE0606 (with pulling force of 11oz ~ 4.253 mT), and some non-magnetic materials (non-magnetic nuts) are introduced and removed near the film and the frequency shifts of both delay lines were recorded using the Agilent Vector Network Analyzer E5061B. Fig 3.3 (a) shows the frequency shift characteristics of both the Ni coated and gold coated delay lines with and without the presence of magnet and non-magnets. As the frequency shift might vary with the direction of the applied magnetic field, both the magnets and non-magnets were placed in three different orientations: vertical, shear-horizontal, and longitudinal orientation, respectively. A reference to these directions is given in Fig 3.3 (b).

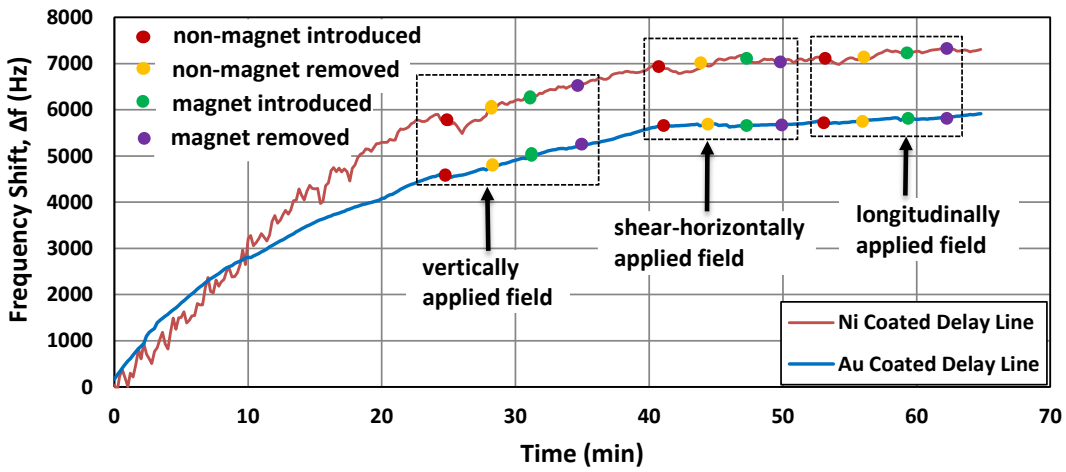

(a)

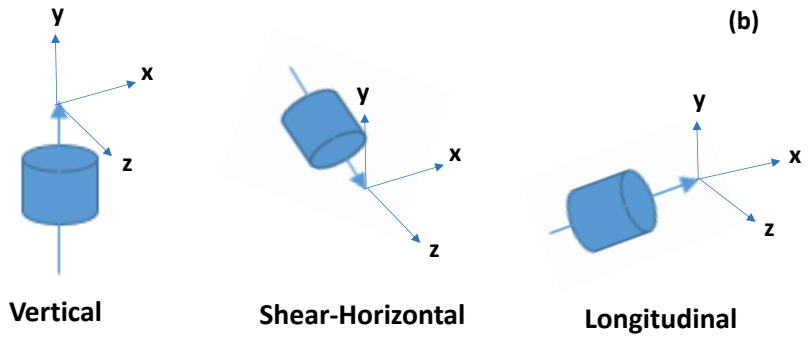

Figure 3.3: (a) Response of Ni coated SAW device shown in Fig 3.2 for different orientation of magnet and nonmagnet (b) reference of the directions (wave propagation is along the x axis)

From Fig 3.3 it has been observed that, the Ni coated delay line does not show the expected sensitivity to magnetic field. Therefore, different strategies were followed to increase the sensitivity by using device 2 with the Ni coating on both delay lines and by using device 4 with two different thicknesses on each of the delay lines (150 nm and 50 nm, respectively). Moreover, on device 3, an additional PMMA (polymethyl methacrylate) polymer layer was deposited as a waveguide layer to better confine the wave to the surface [51] . In all cases, it is found that the devices were not sensitive to the magnetic field. Thus, another type of magnetostrictive metal-alloy-coated SAW device is investigated.

3.3.2 NiFe-Coated SAW Device

Thin films based on metal alloys (e.g., FeCo, FeNiMo, etc.) exhibit soft magnetic properties thus possess strong magneto-mechanical coupling when subjected to a magnetic field [52] . Moreover, they have a relatively high magnetostrictive coefficient and show a large change in longitudinal dimension with an application of the magnetic

field, which makes them good candidates for sensor applications [52] . Here, a 200nm NiFe-coated SAW sensor was prepared for the detection of the magnetic field.

For depositing NiFe film, the magnetron sputtering technique is used, where a plasma is generated and confined to a space containing the material to be deposited. The selection of a target with proper material composition is important to achieve the desired magnetostrictive properties of the film. The NiFe sputter targets used in this work have a composition of 80-81% Ni. Deposition of a 200 nm- thick NiFe coating on the delay line of the acoustic wave device took approximately 4 hours including the cooling phases. Before deposition, the entire cleaning procedure was performed (see materials and procedures section in chapter 4). A PMMA layer of 1 μm is used as a mask. The steps performed to deposit NiFe coating onto both delay lines of the SAW device are shown in Fig 3.4. They are: (a) an insulating tape is placed in between the IDTs to protect the delay lines from the PMMA mask; (b) a 1 μm PMMA layer is deposited by spin coating; (c) the insulating tape that was placed in (a) was carefully removed resulting in a bare delay line but masked IDTs. The device is next placed in an oven at 180°C for 2 hours; (d) a 200 nm NiFe coating is deposited using magnetron sputtering; the PMMA mask is dissolved with an appropriate solution and the NiFe-coated SAW device is ready for characterization. A figure of the prototype device is shown in Fig 3.5.

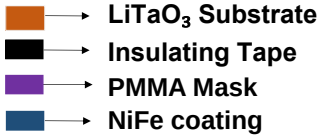

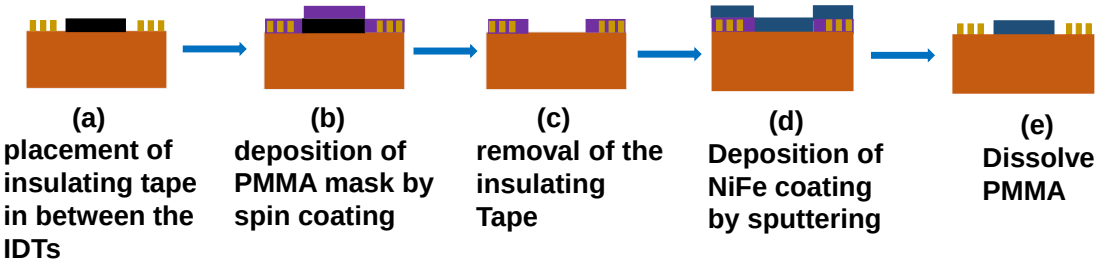

Figure 3.4: Steps of the NiFe coating deposition process onto the SAW device

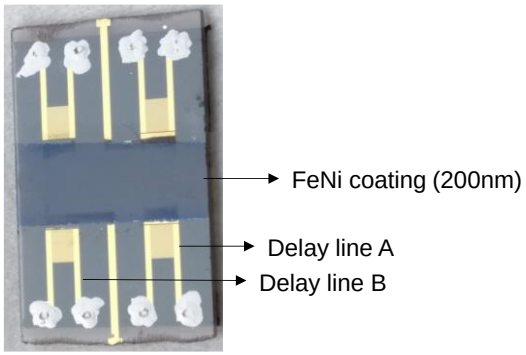

Figure 3.5: One prototype device of NiFe coated (200 nm) SAW device (note that, this coating is already oxidized)

The NiFe-coated SAW device is characterized using the same permanent magnets and nonmagnetic materials in different orientations. It has been observed from those characterizations that the coating does not show significant sensitivity to the magnetic field and the coating appears to be oxidized within a few weeks after deposition.

3.3.3 Limitations of Coated SAW Device

From the above analysis and experimental results, it has been found that both Ni- and NiFe- coated SH-SAW devices do not have the sensitivity required to respond to the magnetic field. To make those films sensitive, one possible solution is to deposit an additional layer of SiO_2, which can cover the IDTs and delay lines, thus trapping the

wave closer to the surface. Also, during the deposition of the magnetostrictive thin film, it is important to introduce an easy axis of magnetization to the film. This was done by applying a magnetic field along the Y-axis for a Love wave SAW based ST-cut quartz substrate by Kittmann et al. [54] . Moreover, instead of metal or metal alloy, possibly a composite film layer would be a good candidate for a magnetostrictive film-based SAW magnetic field sensor [54] .

As a result of the poor sensitivity shown by the Ni- and NiFe- coated sensor design approach, an alternative approach is investigated in this research. An IDT based magnetic sensor design where a single IDT on a piezoelectric substrate is combined with a highly magnetically sensitive element consisting of microwires based on the Giant Magnetoimpedance (GMI) effect will be discussed in the following sections.

3.4 Giant Magnetoimpedance (GMI) Elements for Sensor Application

Since the discovery of the GMI effect, it has been demonstrated that magneto-impedance elements can be used for high-performance magnetic sensor devices [55] . Presently, the research in this field has been focused mainly on special thermal treatments and/or on the development of new materials for improved GMI properties [56] , [57] . However, continuous efforts have been devoted to investigating a variety of GMI sensors for different applications such as magnetic sensor, current sensor, stress sensor, object detection sensor, electronic compass, etc. Although the development of GMI sensors is still at an early stage, it is likely that, in comparison to the processing cost and power consumption of existing conventional magnetic sensors, their low prices and high flexibility (see table 3.2) will permit extensive applications soon [58] .

Sensor type	Sensor Head Length	Detectable field (Oe)	Response Speed	Power Consumption
Hall	10-100 μm	$1\text{-}10^6$	1 MHz	10 mW
GMR	10-100 μm	$0.1\text{-}10^2$	1 MHz	10 mW
GMI	1-2 mm	$10^{-8}\text{-}10^2$	1-5 MHz	10 mW
Flux gate	10-20 mm	$10^{-6}\text{-}10^2$	5 kHz	1 W

Table 3.2: Comparison of magnetic sensors [58]

GMI elements include some soft ferromagnetic materials and metal-based amorphous alloys and can be fabricated in the shape of microwires, ribbons, or thin films [58] . Among them, amorphous GMI microwires are promising for sensing applications in the microsystem industry [57] - [59] . Excellent GMI behavior has been found in Co-based amorphous and Fe-based nanocrystalline soft ferromagnetic wires and has been achieved in glass-covered Co-based microwires. In Co-based amorphous wires, the GMI effect originates from the high transverse permeability characteristics of the material, resulting in the presence of a transversely oriented domain structure and shows nearly zero but negative magnetostriction [60] . Phan et al. showed that microwires primarily of Co-Fe-Si-B in compositions if doped with transition metal elements such as Mo, Cr, Nb, etc., display improved GMI effect and field sensitivity [61] . Intense research has been conducted to improve microwire based GMI sensor design by optimizing sensor parameters and/or design of the electrical circuit [62] , [64] . However, to date, successful GMI microwire-based magnetic sensors have only been developed and commercialized by Aichi Steel Company in Japan with a range of nT to μT [55] , [62] , [65] .

3.5 Giant Magnetoimpedance (GMI) Effect: A Review

The GMI effect is the large impedance change of an alternating current (ac) powered conductive soft magnetic material resulting from a change in the external magnetic field. It was first observed in Co-based amorphous wires by Panina and Mohri in 1994 and has since attracted strong interest due to its high sensitivity enabling magnetic field measurement in the low magnetic field (~ μT to nT) range [56] , [65] - [68] . When a soft ferromagnetic conductor is subjected to a small ac current, a large change in the ac complex impedance of the conductor can be achieved upon applying a magnetic field. The relative change of the impedance, Z, with the applied field, H, which is defined as the giant magneto-impedance effect, is expressed by [58] . Fig 3.6 shows the magnetic field dependence of GMI impedance (Z) at 1MHz for a typical soft ferromagnetic material [58] , [69] .

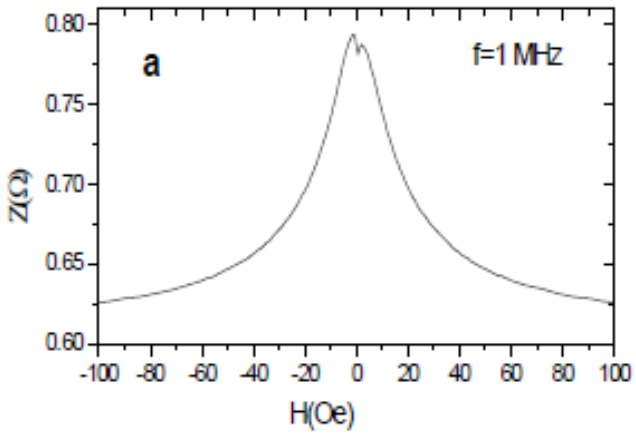

Figure 3.6: Impedance (Z) as a function of applied magnetic field for a conventional GMI material [58] , [69] .

3.5.1 Frequency Dependent Characteristics of GMI Elements

Depending on the operating frequency of the driving ac current, the magnetoimpedance effect of the GMI materials can be roughly categorized into three frequency regimes: [58]

- Low-frequency regime ($f \leq 1\ MHz$): due to the weak skin effect, the change in impedance of the GMI material upon application of the applied magnetic field is mainly from the contribution of the change in the inductance of the material, which is proportional to the circumferential permeability for a cylindrical magnetic conductor (i.e., magnetic wire) and the transverse permeability for a planar magnetic film (i.e., magnetic ribbon) [68] .
- Intermediate frequency regime ($1\ MHz \leq f < 1\ GHz$): due to the strong skin effect a strong change in the effective magnetic permeability upon application of dc magnetic field is observed. Depending on the composition and geometry of the GMI material, the magnetoimpedance at its peak may be dominated by the contribution of either the domain wall motion or the magnetization rotation of the GMI material for the frequency range 1~10 MHz. For further increase in frequency, the domain wall motion is becoming strongly damped by eddy currents, leaving only magnetization rotation as the sole contributor to GMI [69] .
- High frequency regime ($1\ GHz \leq f$): change in magnetoimpedance in this frequency range is due to the gyromagnetic effect and ferromagnetic relaxation. Due to a strong change in the skin depth caused by ferromagnetic resonance

(FMR), the maxima in GMI profiles are shifted towards higher fields in this case [56] .

There are many theoretical models of GMI materials that have been proposed in past years classified according to different criteria such as geometry, domain structure, fabrication procedure etc. The Quasistatic model has been proposed based on the assumption that the operating frequency is small, the Eddy current model can explain the experimental results in the frequency range of several kHz to a few MHz [66] , [68] , [70] . The domain structure model explains the underlying mechanism of a metallic soft magnetic wire with periodic circular domains. It correlates the inductance and permeability characteristics of the wire, which allow for estimating the circumferential permeability as a function of frequency [71] . Both the eddy current and domain structure models have successfully explained several basic features of GMI at frequencies below 100 MHz. The electromagnetic model has described the GMI characteristics in the high-frequency regime. According to this model, the contribution of domain wall motion to the circumferential/ transverse permeability can be neglected and only magnetization rotations considered for GMI effect. This model can interpret qualitatively the basic features of GMI and most of the experimental data in the high-frequency regime. However, it does not consider the exchange interactions in the effective fields [68] , [72] , [73] . There are several other theoretical models that try to describe the GMI features in a wide frequency range as described in the literature [58] .

Existing theoretical models of GMI are developed for specific materials and/or specific frequency ranges (from a few kHz up to GHz). However, none of them can completely explain the underlying mechanisms of GMI for a variety of magnetic

materials, and further theoretical models should be developed based on the identified domain structures of the materials [58] , [68] , [73] . In the following section, the underlying physics and impedance characteristics of a Co-rich amorphous wire fabricated using melt extraction process and operated in the MHz range are described as it is well-matched with the geometry and operating frequency of the GMI microwire used in the proposed magnetic sensor design.

3.5.2 Impedance Characteristics of GMI Microwires

Depending on the operating frequency $f = \omega/2\pi$, when an ac current, $I = I_0 e^{-i\omega t}$, flows through a GMI wire, the skin effect confines the current to the surface region of the wire. The penetration depth, δ, of the current depends on the resistivity of the material ρ, the frequency of the current ω, and the magnetic permeability, μ [74] :

$$\delta = \sqrt{\frac{2\rho}{\omega\mu}} \tag{3.4}$$

From equation (3.4), it can be inferred that with increasing operating frequency, there is a large variation in skin depth. Most importantly, this large GMI effect is observed if the wire is subjected simultaneously to ac current and external dc field, which modifies the value of μ, thus changing the effective conduction region and consequently the impedance of the wire. The complex impedance of a GMI microwire for a high frequency of operation is given by the following equation [56] , [66] :

$$Z_g = R_{dc}\, {}^{r}/_{2\delta} + j\omega\, L_g\, {}^{2\delta}/_{r} \tag{3.5}$$

where, $R_{dc} = \rho l/\pi r^2$ is the dc resistance, r and l are the radius and length of the wire, and $L_g = \mu l/8\pi$ is the internal inductance of the GMI wire [75] . The permeability of the wire is a complex function and depends on the applied external field, H_a and can be expressed as, $\mu = \mu_s/(1 - j\,\omega/\omega_r)$ [66] . Here, μ_s is the static circumferential permeability and ω_r is the characteristic relaxation frequency. The magnetoimpedance effect of a negative magnetostrictive amorphous wire (Co-rich) can be explained using equation (3.5) together with the frequency dependent permeability, μ.

Depending on the material composition and microwire fabrication technique, the internal domain structure may vary, which in turn affects the internal current distribution hence the impedance response of the wire [76] , [80] , [84] . The GMI wires used for this research are amorphous Co-rich fibers, and were fabricated using the melt extraction fabrication technique, where the fibers are extracted from the melt by a rapidly rotating sharpened wheel. When the fibers are extracted, they first cool at the tip and around the circumference, placing the still liquid core under compression [76] . The melt extraction determines uniaxial anisotropies along the wire axis called easy axis and transverse anisotropy (circular magnetic domain in the outer shell) in the radial part of the wire with outstanding soft magnetic properties and high magnetic permeability as shown in Fig. 3.7 [77] .

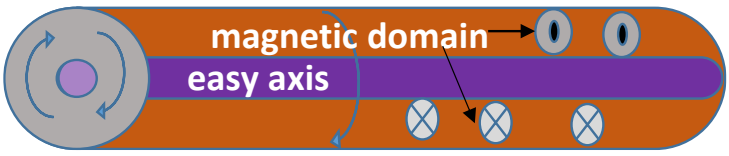

Figure 3.7: Internal structure of GMI microwire fabricated using melt extraction and rapid solidification process

This induced anisotropy plays an important role in the GMI behavior of the amorphous wires. It has been demonstrated that for wires with circumferential anisotropy there exists a critical circumferential field below which there is no significant circumferential flux change and accordingly no impedance change [78] .

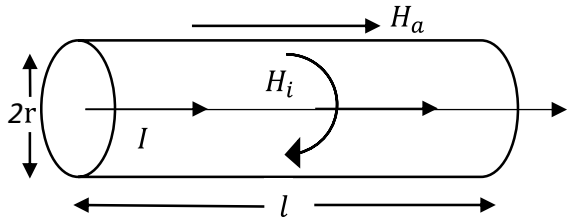

Figure 3.8: GMI microwire placed in an external dc longitudinal magnetic field and carrying an ac current which produces a circumferential ac field [70]

In general, when a high frequency ac current is applied, because of the strong skin effect (i.e., $r/\delta \gg 1$) the current tends to be concentrated near the surface of the wire, resulting in the generation of a small ac circumferential field as shown in Fig. 3.8. The magnitude of this small field can be defined as $H_i = I/2\pi r$ and is uniform at a distance r from the wire axis. Under such conditions, when H_a is applied along the wire axis, there is a balance between the circumferential anisotropy, applied axial dc field and circumferential ac fields [78] . The combined axial dc field, and circumferential ac field suppress the circular flux change and μ contributes to a change in transverse anisotropy due to magnetization rotation. The magnitude of complex circumferential permeability, μ increases with increasing H_a in the low field region until it reaches the effective anisotropy field, H_K, of the wire.

H_K depends on the material composition and geometry of the wire and can be expressed as $H_K = 2K/\mu_0 M_s$ where K is anisotropy constant and M_s is saturation magnetization [56] , [66] . In this case, the expression for impedance in equation (3.5) can be reduced to

$$Z_g[\omega, \mu(\omega, H_a)] \propto (\omega\mu)^{1/2} \tag{3.6}$$

From the above analysis, the GMI effect can be understood in terms of the skin depth and its relation to the radius, r, of the wire, which is affected by the circumferential permeability, μ. To obtain a large GMI effect, it is necessary to reduce the skin depth by choosing magnetic materials that have large permeability and small dc resistance.

3.6 Summary

In this Chapter, the fundamental aspects of GMI materials exhibiting the GMI effect have been discussed. A brief review of several theoretical models of the GMI effect was presented. A comprehensive description of the correlation between the frequency-dependent impedance characteristics is given, specifically for the Co-rich amorphous wire fabricated using melt extraction process and operated in MHz frequency range.

4. GMI-IDT MAGNETIC SENSOR: MODELLING AND ANALYSIS

4.1 Introduction

Micromagnetic sensors with high sensitivity, rapid response time, and high temperature stability are needed for nondestructive testing and sensing in various areas such as industrial, automotive, and environmental measurement, etc. Magnetic sensors based on surface acoustic wave (SAW) sensing platform utilizing GMI wire and/or GMI sensor have only recently been explored by a few researchers [36] , [65] , [75] , [79] . Hauser et al. have designed a passive, wireless magnetic sensor using a two-port SAW transponder coupled with GMI wire and external impedance element [75] . Using a similar concept, Li et al. proposed a magnetic sensor using a two-port SAW transponder coupled with a tri-layer thin film GMI sensor [65] . Vijay et al. developed a wireless current sensor by combining a GMI thin film magnetic sensor and a two-port SAW transponder [79] . However, for most of these investigations, only proof-of-concept work has been done on the integration of the SAW device with GMI wires or films. There is still a need for theoretical analysis, investigation of the sensor parameters, preconditioning method, and repeatability measurement, which is essential before developing and commercializing those sensors.

The objective of this chapter is the study and analysis of the underlying physics and sensing mechanism of the proposed magnetic sensor. Based on the impedance loaded equivalent circuit model of the IDT and frequency dependent permeability characteristics of GMI wire, a detailed model of the proposed GMI-IDT magnetic sensor will be given. This chapter will also describe how the sensor parameters were modified to maximize the sensitivity and ensure repeatability.

4.2 Theoretical Modelling of GMI-IDT Sensor

The GMI wire exhibits a magnetoimpedance effect when operated in the MHz frequency range, when the skin effect is strong, i.e., the skin depth, δ, is much smaller than the wire radius, r, ($\delta \ll r$). In this case, the expression for the GMI microwire impedance can be written as [80]

$$Z_g[\omega, \mu(\omega, H_a)] = D\sqrt{\mu}\,; \tag{4.1}$$

where, $D = \frac{(1-j)}{2\sqrt{2}} \frac{l\sqrt{\rho\omega}}{r}$

Note that D is constant for a GMI wire with given wire length, l, radius, r, resistivity, ρ, and operating frequency, ω. Equation 4.1 implies that Z_g depends on microwire permeability, μ, which in turn depends on the applied magnetic field H_a. In the present sensor design, the GMI wire is used as a shunt-load to a single IDT to affect the transduction process of the IDT.

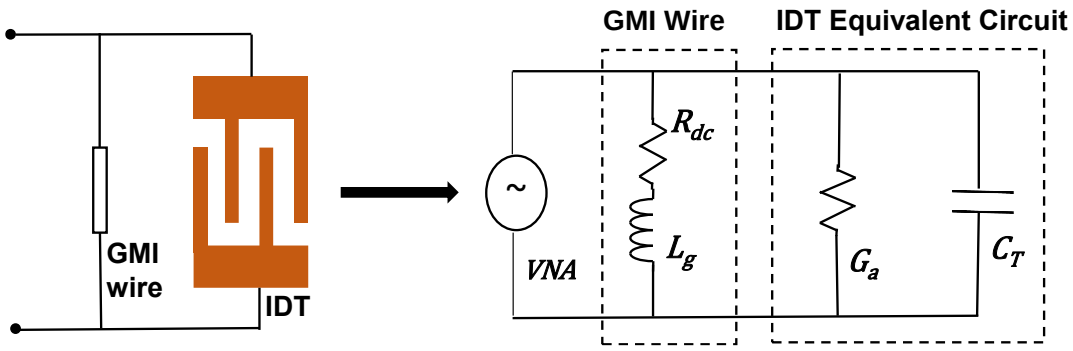

Figure 4.1: Equivalent circuit model for GMI-IDT sensor

When the GMI-IDT sensor is exposed to a dc magnetic field, the signal reflected from the IDT is modified by the GMI wire and thus contains the sensing information as a change of return loss. The equivalent circuit model of the GMI-IDT sensor is shown in

Fig. 4.1, where the IDT is operated at or near the IDT synchronous frequency, ω. The return loss of a transducer with a load can be expressed by the following equation [106] , [42] ,

$$RL = -10\log_{10}\frac{{Q_L}^2}{(Q_L Q_r)^2+(Q_r + Q_L)^2} \tag{4.2}$$

where Q_r and Q_L are acoustic radiation and external load radiation, respectively. For a GMI wire load, $Q_L = \omega C_T Z_g$, the return loss for the GMI-IDT sensor can be derived from the above model and expressed as

$$RL = -10\log_{10}\frac{{G_a}^2}{(\omega C_T)^2+ (G_a+1/D\sqrt{\mu})^2} \tag{4.3}$$

In equation 4.3, the IDT radiation conductance, G_a and static capacitance, C_T are constant and insensitive to H_a. Thus, the change in return loss, *RL,* depends on how the permeability, μ of the GMI wire modulates the IDT transduction process (i.e., G_a). The sensitivity equation of the proposed GMI-IDT sensor model can be obtained from Eq. 4.4, as

$$S = \frac{\partial RL}{\partial H_a} = \frac{\partial RL}{\partial \mu}\frac{\partial \mu}{\partial H_a} = -4.34\left\{\frac{(G_a+1/D\sqrt{\mu})}{D\mu^{3/2}[(\omega C_T)^2+ (G_a+1/D\sqrt{\mu})^2]}\right\}\frac{\partial \mu}{\partial H_a} \tag{4.4}$$

Equation 4.4 indicates that the sensitivity of the GMI-IDT sensor depends on the change of permeability with the magnetic field ($\partial\mu/\partial H_a$) as well as ω and G_a. The dependence of the permeability of the GMI microwire on an external magnetic field, H_a is generally the result of two mechanisms: magnetic domain-wall motion and magnetic moment rotation. However, as the operating frequency for the selected sensor design is in the high frequency range (MHz range), the domain-wall motion can be neglected, and

permeability is affected only by magnetic moment rotation [80] . The resulting transverse permeability ($\mu_{tr} = \mu'_{tr} - j\mu''_{tr}$) is a function of frequency; it increases with the magnetic field value up to the effective anisotropy field H_K and exhibits a saturation behavior above H_K [80] , [81] . H_K depends on the material composition and geometry of the wire and has the form of $H_K = 2K/\mu_0 M_s$, where K is the anisotropy constant and M_s is saturation magnetization [66] , [75] .

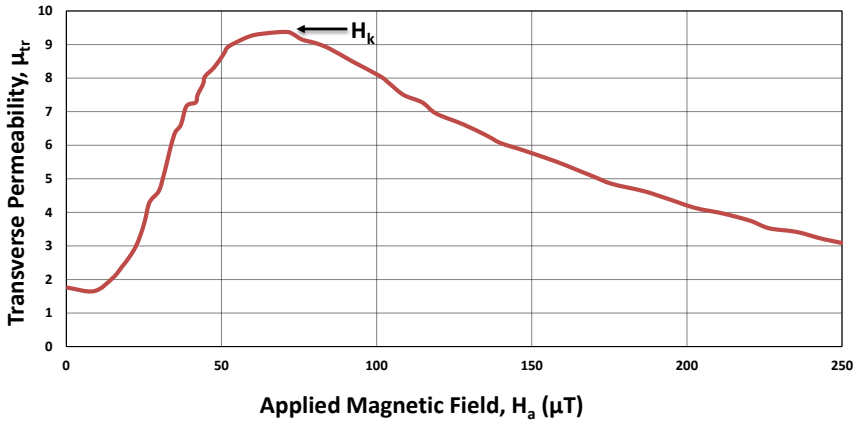

Figure 4.2: Characteristics of the relative transverse permeability of GMI ribbon as a function of applied dc magnetic field operated at 100 MHz frequency [81] .

The semi-empirically determined behavior of GMI wire permeability as a function of the applied dc magnetic field is shown in Fig. 4.2. This estimation is done by scaling the imaginary part of the relative transverse permeability for a GMI ribbon as a function of the applied dc magnetic field at 100MHz, as measured in ref. [81] . The sensitivity of the GMI-IDT sensor as a function of the magnetic field can be explained according to the permeability characteristics of the GMI wire, which will be discussed later in the results section of this dissertation.

4.3 Effect of Sensor Parameters on GMI-IDT Sensor Performance

The proposed sensor design utilizes two sensor elements, a single IDT and a GMI wire. The use of a GMI wire as the sensing element in a real industrial environment requires consideration of several wire parameters that can affect the accuracy, reliability, and stability of the sensor measurement. The IDT parameters can also affect the sensor measurement with the appropriate selection of the piezoelectric substrate and orientation, the IDT frequency of operation, the number of finger pairs and electrode dimensions such that the radiation conductance, G_a and electrostatic capacitance, C_T can enhance the effect of the GMI impedance change. In this work, the IDT of a previously designed sensor device was selected and used to prove the concept. Only the parameters associated with the GMI wire are considered for this investigation and are listed below.

1. Investigation of the appropriate GMI wire length for suitable pairing with the selected IDT design
2. Investigation of stress (wire bending) on GMI wire performance
3. Investigation of appropriate GMI wire preconditioning procedure to ensure sensor stability and repeatability
4. Investigation of suitable impedance matching of the GMI wire with the IDT to maximize the IDT transduction process, hence sensor sensitivity

4.3.1 Effect of GMI Wire Length on the Sensor Performance

The GMI effect is significant with large wire permeability, large skin effect hence small skin depth, and large resistivity. However, these parameters are strongly dependent on microwire geometry e.g., wire length, diameter, distribution of magnetic domains across the wire length, etc. [82] , [83] . Varying the geometrical dimensions of the

microwire can significantly affect the magnetic properties hence GMI behavior. A few studies have been conducted to assess the effects of wire length on the GMI wire characteristics and it has been found that there exists a critical length for all types of GMI wires below which the magnetoimpedance effect was found to decrease [82] . Since the present work involves Co-rich GMI wires, the focus will be on the length effect. Zhukova et al. characterize Co-rich microwires with a diameter of about 125 μm and estimated critical length of approximately 4 cm. For those wires, the spontaneous magnetic properties are lost if the sample becomes shorter than the critical length. Moreover, due to the demagnetizing field, the magnetization of the inner core of the Co-rich wires is twisted near the wire end whereas it is normally directed along the wire axis throughout the full wire length [82] . It is crucial to find the critical length to avoid demagnetizing effect and achieve the highest GMI effect with low electrical resistance. However, for the GMI wires with short wire length, there is a trend of formation of closure domains near the ends of the wire, which can reduce the GMI effect [82] , [83] .

To avoid that, the GMI wires chosen for this proposed sensor design were taken from a long piece of GMI wire and the middle portion of it cut carefully to ensure the wire has a good domain wall structure. In addition, the effects of different wire lengths on wire impedance were investigated, and the best length was selected for the proposed sensor design, which will be discussed in the next chapter along with experimental results.

4.3.2 Effect of Stress or Bending on GMI Wire Performance

Another important parameter that is investigated is the effect of bending on GMI wire properties. Commonly, some magnetically sensitive elements such as induction

wires show a trend to enhance the sensitivity when formed into a coil or toroidal structure. Efforts have been made to make such toroidal structures using GMI wires despite their rigidity. However, it was observed that the GMI effect was reduced significantly or almost vanished in those deformed structures. Nabias et al. investigated the effect of the bending stress on the GMI wire performance for Co-rich wires [85] . From their analysis, upon bending, the magnetic domain structure formed during fabrication is subjected to a deformation hence reducing the GMI effect and sensitivity. The applied stress due to the deformation leads to a decrease in the number of magnetic domains and an increase in the domain width. As a result, the mobility of the domain wall is reduced, which eventually reduces the permeability hence the sensitivity of the wire. However, for smaller stress, the circumferential domain structure of the GMI wire may be refined and could increase the magnitude of the GMI effect. As a result, the GMI wires are preconditioned by applying smaller stress called stress annealing [86] , [87] .

4.3.3 GMI Wire Preconditioning Methods for Maximizing Sensor Stability

For GMI wires, the formation of the domains and magnetic anisotropies are the result of the complex internal stress imposed during the fabrication process. However, the unique domain structure of such prepared GMI wires is very unstable and changes their magnetic properties with time (aging) and other environmental effects [88] , [89] . Therefore, further investigation of the magnetic properties using different kinds of preprocessing such as annealing is essential to enhance the sensitivity and ensure the repeatability of the sensor.

A simple and classical method of tailoring the structure of GMI wires is by adequate thermal treatment. The temperature dependence of the GMI wires and ribbons

were explored by several researchers: Kim et al. [88] investigated the magnetoimpedance properties for Co-rich GMI ribbons for various temperatures (10K – 300K) while operated at different frequencies; Knobel et al. [89] investigated the magnetic behavior of Fe-rich GMI wires on annealing in the range of 500-600°C for 1 hr.; Aichi steel company developed a commercially available magnetic sensor, which is subjected to thermal treatment at a temperature between 500-600°C for only 4 to 10 sec [86] , [88] , [89] . GMI wires were preconditioned by applying dc and ac current through the samples[90] , [92] . By controlling the amplitude of the annealing current, annealing time, and cooling conditions, it is possible to achieve a stable magnetic anisotropy and domain structure. Pirota et al. explored the GMI wire behavior while the samples are heated by applying a constant current and different tensile stress; the effects were analyzed to estimate the rate of crystallization [93] . From the above literature review, it has been found that with proper selection of the annealing method it is possible to change the complex distribution of internal stress of the GMI wire. Moreover, proper annealing will help to induce circular anisotropy, preferably vortex structure, which consists of a single domain and allows more reproducible magnetic properties compared to untreated GMI wires [86] , [91] .

4.3.4 Investigation of Suitable Matching Elements of the IDT to Improve Sensor Sensitivity

Earlier in this chapter, a detail model of the GMI-IDT sensor was described along with the sensitivity equation. However, to improve the sensitivity, the basic sensor design is further modified. This investigation was required for the intended application since small changes in magnetic field need to be measured, and the modified design is tested in monitoring the magnetic properties of EV-type Li-ion battery cells. For a GMI wire-

loaded IDT configuration, (shown in Fig. 4.1) resonance occurs in the system because of the inductive effect from the GMI wire and the capacitive effect from the IDT. Also, the inductive effect of the GMI wire increases upon the application of the dc magnetic field and a part of it is compensated by the capacitance of the IDT.

Thus, in the modified sensor design, efforts have been made to compensate all the capacitive effect that originated from the IDT and the other circuit elements with an appropriately selected matching circuit. Incorporation of the matching circuit with the sensor design confirms all the capacitive effects are compensated for properly, leaving only the inductive effect from the GMI wire present in the sensor circuit. Thus, the transduction process of the IDT is affected only when the GMI wires are exposed to an external magnetic field, resulting in an increase in the sensitivity of the sensor. The sensor design is modified with particular attention to the operating frequency of 104 MHz as this is the frequency the IDT is designed for [95] . The characterization results of the modified GMI-IDT sensor will be presented in the results and discussion chapter of this dissertation.

4.4 Principle of Battery Internal State Monitoring via Magnetic Sensing

This section will describe the underlying principle of the magnetic properties of Li-ion batteries using a magnetic field distribution model. As battery internal state is proportional to the magnetic properties of the battery, determination of these properties can be linked directly to the internal state (e.g., charge capacity, SOC, etc.) of the battery.

4.4.1 Model for Magnetic Field Distribution of Li-ion Batteries

The magnetic susceptibility, $\chi = M/H$, is a measure of how much a material will become magnetized in an applied magnetic field, where M is the magnetization

(magnetic moment per volume unit) and H is the intensity of the applied magnetic field [94] . Generally, magnetic susceptibility measurement involves placing the sample in a reference magnetic field and measuring the small magnetic field distortion induced by the sample's magnetic susceptibility via a magnetic field sensor [28] . This principle can be visualized using the magnetic field distribution model shown in Fig 4.3.

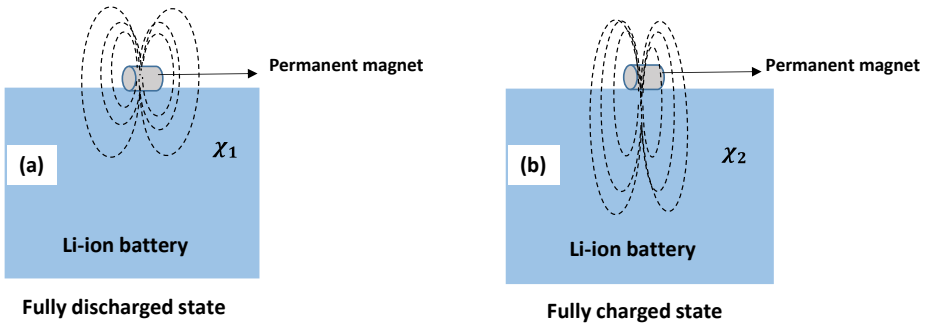

Figure 4.3: Magnetic field distribution of the reference permanent magnet in response to battery's magnetic susceptibility (a) for fully discharged state (b) for fully charged state

Consider a Li-ion battery cell with a reference magnet (permanent magnet in this case) attached to the surface of the battery as shown in Fig 4.3. Assume that, initially, the battery is in completely discharged state, thus, the magnetic susceptibility of the battery is very low. The magnetic field distribution around the permanent magnet in this case is nearly undistorted as shown in Fig 4.3 (a) and the magnetic susceptibility in this case is χ_1. Upon charging from this state, the active material (Li-ion) is extracted from the positive electrode, which changes the oxidation state of the transition metal. This leads to a change in the magnetic moments of the transition metals, hence an associated change in the magnetic susceptibility, and the latter becomes χ_2 for a fully charged battery as

shown in Fig 4.3 (b), where $\chi_2 > \chi_1$. Due to the change in magnetic susceptibility, the magnetic field distribution around the permanent magnet will be distorted as shown in Fig 4.3 (b) from its initial state as shown in Fig. 4.3 (a). Except for single crystals, it is known that the magnetic susceptibility is a scalar quantity; thus, the distortion of the magnetic field does not depend on the direction of the magnetic field. Since the electrode material of the battery is paramagnetic, the magnetic field of the reference magnet is pulled by the electrode material and the field distribution extended towards the battery. By subtracting the magnetic fields of the reference magnet from (b) to (a) a total change in magnetic field caused by the change in battery magnetic susceptibility can be inferred. Using this setup, if a magnetic sensor having high sensitivity in the low magnetic field range is placed in an optimum position relative to the reference magnet and the battery, it is possible to track the minute change in magnetic field caused by the change in battery magnetic susceptibility, which can be linked to the battery internal state. The above approach will be used when the proposed sensor is implemented for monitoring battery internal state.

4.4.2 Impact of the Strength of the Reference Magnet in Monitoring Batteries Magnetic Properties

From the model presented above, we have learned that the magnetic field of the reference magnet will be distorted with the change in magnetic susceptibility of the electrode material during charging and/or discharging. However, the distortion of the magnetic field of the reference magnet is not only depending on the overall change in magnetic susceptibility of the battery but also the strength of the reference magnetic field. It has been shown experimentally that if the magnitude of the reference magnetic field is small, and the sensor is placed far from the sample, the detected change in magnetic field

could be much smaller (~ 100s of pT) [28] . Generally, the overall change in magnetic susceptibility of the battery material from a fully discharged state to charged state is very small [26] thus, one way to maximize the distortion of the reference field is the selection of strong reference magnetic field. A quantitative analysis will be presented here to elaborate the impact of the strength of the reference magnetic field in the detection of the battery's magnetic susceptibility.

Theoretically, the overall change in magnetic susceptibility from a fully discharged to a charged battery is $\Delta\chi = \chi_2 - \chi_1 = 0.8 \times 10^{-3}$ S.I. units and the associated change in magnetic flux is 0.0798% [26] . Also, from T. Gallien et al., the experimental overall change in magnetic susceptibility from a fully discharged to a charged battery is $\Delta\chi = 2.27 \times 10^{-4}$ S.I. units and the associated change in magnetic flux is 0.0227% [94] . If a permanent magnet has the strength of 170 mT, the calculated change in magnetic field around the permanent magnet is approximately 135 μT for a change in magnetic flux of 0.0798% and 38.6 μT for a change in magnetic flux of 0.0227%. Note that 170 mT is the strength of a NdFeB magnet, which will be used later as reference magnetic field for the magnetic measurement of the battery. The calculated field values: 135 μT and 38.6 μT are the upper limits for the maximum change that the magnetic sensor could possibly see for the selected reference magnetic field. Based on the above, an optimum geometry of the of the experimental setup for battery measurement is developed, which will be discussed in the following chapter.

4.4.3 Impact of the Packaging Material in Monitoring Batteries Magnetic Properties

Another important factor of concern is the impact of packaging material in monitoring battery magnetic properties. The most common packaging material used for

cylindrical and prismatic cells are hard metallic enclosures whereas, for pouch cells, the packaging material consists of conductive multi-layer foils. Furthermore, for a multi-cell battery pack construction, often compression plates are used to provide additional mechanical pressure to the battery, which helps to prevent battery swelling [25] .

In this research, efforts have been made to track the change in magnetic susceptibility of the battery electrode material using a commercially available portable magnetic susceptibility meter (model: KT-10) having a sensitivity of 10^{-7} S.I. units. One of the objectives in the present work is to quantify the magnetic susceptibility of the electrode material for a fully charged and discharged battery. However, it was found that the susceptibility meter is based on ac technology (an ac coil is used to probe the sample) with an operating frequency of 10 kHz [97] . At this frequency, the conducting packaging material acts as a Faraday cage and prevents the susceptibility measurement of the battery electrodes using commercially available susceptibility meters. An alternative way to measure battery magnetic susceptibility is using dc magnetic field sensing. Since the proposed GMI-IDT magnetic sensor is based on dc magnetic field sensing, it can be used in monitoring the magnetic properties of a Li-ion battery cell or a Li-ion multi-cell battery pack regardless of the packaging material type.

4.5 Equipment and Instrumentation

4.5.1 GMI-IDT Sensor

The sensor device used to implement the proposed sensor is a multielectrode IDT pattern deposited on a piezoelectric substrate (36° YX-$LiTaO_3$) [95] . The device has an electrode finger width of 5 μm, a periodicity of 120 μm, a basic operating frequency of 34 MHz, and harmonics at about 68, 104, and 138 MHz. The GMI wires used in this

work consist of amorphous $Co_{71}Fe_4Si_{14.5}Nb_4B_{6.5}$ fibers of about 30 μm in diameter [80] and were obtained from MXT, Montreal, Canada is shown in Fig 4.4.

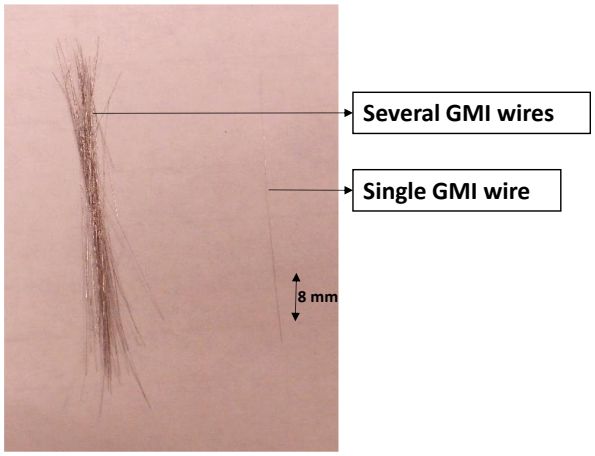

Figure 4.4: A sample of the Co-rich GMI wires used in the sensor implementation

The single IDT of the sensor device is used to implement the GMI-IDT sensor. An insulating tape is used to cover the delay lines of the device to attenuate the acoustic transmission between the IDTs. The single IDT of the device was connected in parallel to the GMI wire as shown in Fig 4.5. A network analyzer (Agilent E5061B, Santa Clara, CA) was used to measure the impedance spectra and insertion loss of the GMI-IDT sensor device as a function of magnetic field strength for different SAW harmonic frequencies.

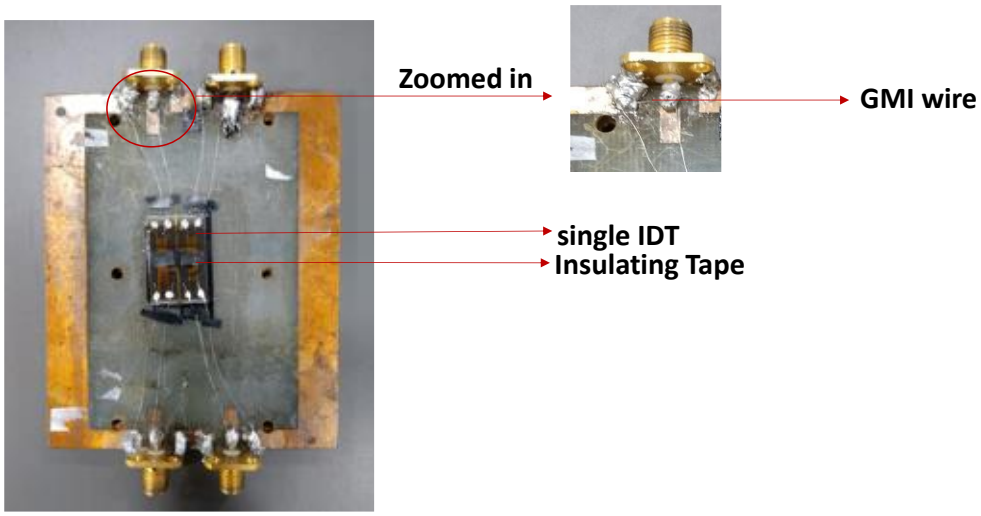

Figure 4.5: GMI-IDT sensor device

4.5.2 Magnets and Electromagnet

To characterize the GMI-IDT sensor, several magnets and electromagnets were used. The constant magnetic field was applied using three different permanent NdFeB magnets exhibiting different magnetic strengths. The images of permanent magnets are shown in Fig 4.6 (a). An electromagnet is used to apply the magnetic field with varying field strength as shown in Fig. 4.6 (b). The electromagnet (model number: BDE-1212-12, operating voltage: 12 V, pull force: 18 kg) has a good resolution in the weak field range. To vary the magnetic field strength of the electromagnet an Agilent E3631A power supply was used. Furthermore, a gaussmeter (model number: GM-1-ST DC) from Alphalab Inc. is used to measure the magnetic field of the permanent magnets and the electromagnet during experiments.

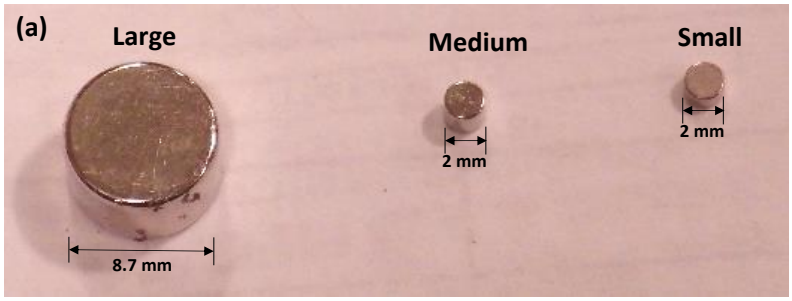

- **Large magnet: approximate pull 6 lb (2.8 kg ~ 170.36 mT)**
- **Medium magnet: approximate pull 11 oz (0.31 kg ~ 42.53 mT)**
- **Small magnet: approximate pull 7 oz (0.2 kg ~ 22.21 mT)**

Figure 4.6: (a) Permanent magnets (b) Electromagnet

4.5.3 Faraday Cage

Since the sensor is sensitive to a dc magnetic field and the operating frequency is in the RF range, it was assumed that the sensor is not affected by the background magnetic field generated by other instruments present in the lab as they are operated through the power cables at grid frequency (60Hz). However, to ensure any other background magnetic field noise is not interfering with the sensor measurement, the characterization of the GMI-IDT sensor was performed inside of a Faraday cage. The

cage was built in the Microsensor Research Lab by modifying an aluminum truck toolbox with a size of 59.4 (L) × 40.6 (T) × 45.7 (W) cm and a thickness of about 0.127 cm.

4.5.4 Li-ion Batteries and Battery Tester

There are two types of NMC (lithium nickel manganese cobalt oxide) Li-ion batteries used in the magnetic measurement. They are the BEV pouch cell and the PHEV cell. The BEV pouch cells are manufactured by LG company and are used in Battery Electric Vehicles (BEV). They have a capacity of 15 Ah and a size of 226 (L) × 5.45 (T) ×164 (W) mm. The PHEV cells are manufactured by Panasonic company and are used in Plug-in Hybrid Electric Vehicles (PHEV). They have a pure NMC cathode with the general formula $LiNi_xCo_yMn_zO_2$; where, x = 0.33, y = 0.33, z = 0.33. They have a capacity of 25 Ah with a size of 148 (L) × 26.5 (T) × 91 (W) mm. Generally, for EV- type Li-ion batteries, compression plates are used to prevent cell swelling and to ensure a uniform pressure distribution to the cell surface.

For performing battery measurements, a portable battery and cell test system (Mint MS7520 battery tester) is used. This tester model consists of two channels and can test and evaluate power generation, storage, and drive technology of Li-ion cells and batteries. The tester is controlled by proprietary software used to write the test-flow program and monitor and collect measurement data in real-time.

4.6 Experimental Procedure

4.6.1 GMI-IDT Sensor Characterization

Proper device surface cleaning should be performed to ensure that the IDT performance is reproducible. The cleaning procedure used in this work is described in [96] . A solder connection is used to fix the GMI wire in parallel with the IDT and

mounted in place on a sensor board for measurements (as shown in Fig 4.5). The initial characterization of the GMI-IDT sensor was performed inside a Faraday cage using an electromagnet as described above. A diagram of the experimental setup is shown in Fig 4.7.

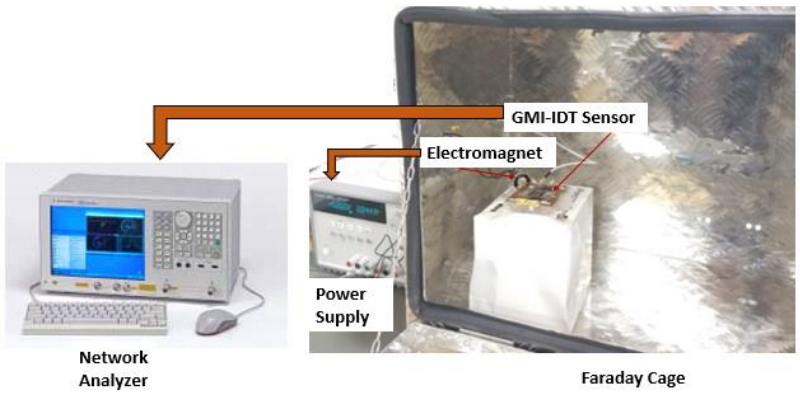

Figure 4.7: Schematic view of the experimental setup for the characterization of the GMI-IDT sensor using an electromagnet

To achieve maximum influence on the magnetic properties of the GMI wire, the magnetic field is applied parallel to the GMI wire, as described in the literature [84] . Sensor return loss as a function of varying magnetic field is collected using a network analyzer in 10 second intervals. This setup is also used for the investigation of sensor parameters associated with the GMI wire.

4.6.2 GMI Wire Parameter Characterization

To investigate the effect of GMI wire length on sensor performance, several GMI wires of different lengths are selected in the range of 3 mm – 10 mm. Each selected wire length is connected appropriately to each IDT, and the impedance response of each GMI-

IDT sensor is characterized for varying magnetic field and data was collected using the network analyzer.

To investigate the effect of bending on GMI performance, long pieces of GMI wires were taken and formed into coil shape with one or two loops. It is noted that the GMI wire displays some degree of rigidity, and as a result, the formed coil has to be maintained with a tape. The GMI coils are then connected to a similar type of sensor board as shown in Fig 4.5. The impedance response of the GMI coil was characterized without and with applied magnetic field (a permanent magnet of strength 170 mT) and data were collected using the network analyzer.

For maximizing sensor stability, several preconditioning methods for GMI wires are investigated experimentally, which consist of:

- Thermal annealing: For the thermal annealing process, several GMI wires were heated inside an environmental chamber at 50°C or 100°C for 30 mins followed by another 30 min of relaxation time. Next, the thermally annealed wire is connected to the IDT, and the return loss response of the sensor is characterized for varying magnetic field over an extended period of time.
- Current annealing: For current annealing, several GMI-IDT sensors were prepared each with an untreated GMI wire on it. A selected amplitude of RF current (between 1.5 – 2 mA) was applied to each sensor device by adjusting the output power of a network analyzer. The bandwidth of the applied current is selected for 60-210 MHz. The annealing time is selected between 4-15 min followed by a relaxation time of 10 min. Next, the return loss response of each sensor device is characterized for varying magnetic field.

- Magnetic field annealing: In magnetic field annealing, a constant magnetic field of 1.5 mT is applied using an electromagnet to an untreated GMI wire connected to an IDT. The direction of the applied magnetic field was kept parallel with respect to the wire axis. Using this procedure, several GMI wires were annealed with annealing time between 8-10 min followed by a relaxation time of 10 min. The return loss response of each sensor device is characterized for varying magnetic field and data was collected using the network analyzer.
- Simultaneous current and magnetic field annealing: several untreated wires were subjected to simultaneous magnetic field and current annealing while each of them is connected to a separate IDT. A constant RF current (1.5 mA, bandwidth: 50-150 MHz) and a constant magnetic field (1.5 mT, parallel to the easy axis of the wire) is applied to the wire by using a network analyzer and an electromagnet, respectively. The annealing time is selected between 8-10 min followed by a relaxation time of 10 min. The return loss response of each sensor device is characterized for varying magnetic field and data was collected using the network analyzer.

Next, the preconditioned device is further modified by including a matching element with the basic GMI-IDT sensor device to improve sensor sensitivity. The selection procedure of the appropriate sensor preconditioning method and matching component will be described in the next chapter along with experimental results.

The measurement of the return loss response of the impedance matched and preconditioned devices was performed using an electromagnet and was recorded using the network analyzer. Only sensors which show repeatable responses for several months

are considered suitable for use. The repeatable device is then used in monitoring the internal state of two types of Li-ion battery cells.

4.6.3 Battery Internal State Characterization using GMI-IDT Sensor

Fig. 4.8 represents the experimental setup that was used to characterize the internal state of a BEV pouch cell with the GMI-IDT sensor. Note that the same setup was used for monitoring the internal state of a PHEV cell. For testing BEV/PHEV battery cells, the sensor is placed in close proximity to the battery. After connecting the battery to the battery tester and the sensor to the network analyzer, the battery is cycled for selected charge time and selected discharge time depending on the battery type. Measurements consist of enough cycles to take the battery from the fully discharged state to fully charged for charging measurements, and vice versa for discharging measurements. Data is collected at the end of a rest step after each charging/discharging step to ensure that the battery has had adequate time to rest, thus ensuring that the equilibrium open circuit voltage is reached. Measurements are conducted in this manner over time to quantify sensor repeatability. All the measurements were performed at room temperature.

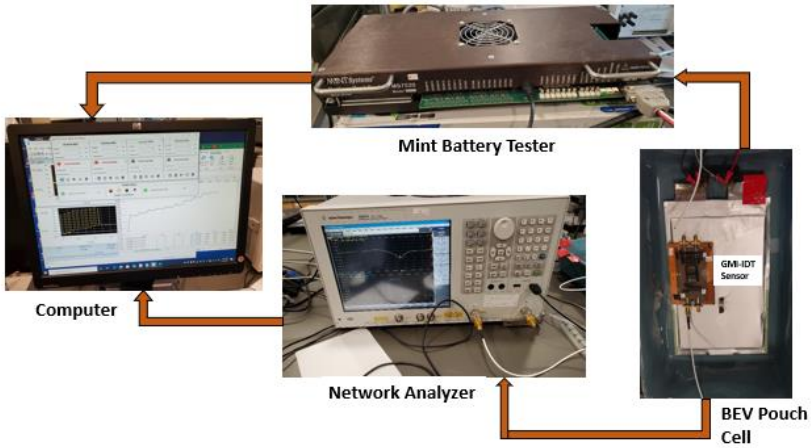

Figure 4.8: Experimental setup of BEV Pouch cell measurement with GMI-IDT sensor

4.7 Summary

In this chapter, a detailed model of the GMI-IDT sensor was presented. To enhance sensitivity, stability, and repeatability, an investigation of the sensor parameters was performed, which was discussed with respect to the GMI wire properties and the IDT transduction process. A literature review of several types of preconditioning methods of the GMI wire was presented. Furthermore, a detailed discussion of the materials and procedures was presented along with the experimental setup. In the next chapter, the experimental results and discussion will be presented.

5. RESULTS AND DISCUSSIONS

5.1 Introduction

In this chapter, the experimental results for the GMI-IDT sensor characterization will be presented and analyzed. The proposed sensor is implemented for magnetic field measurements of two types of Li-ion batteries. Using the sensor responses, the internal state of the batteries is extracted, and a correlation is established with the underlying battery electrochemistry.

5.2 Characterization of GMI-IDT Sensor

The frequency dependence of the return loss characteristics of the GMI-IDT sensor was described using an equivalent circuit model in chapter four. The measured loss is shown in Fig 5.1 for different field strengths.

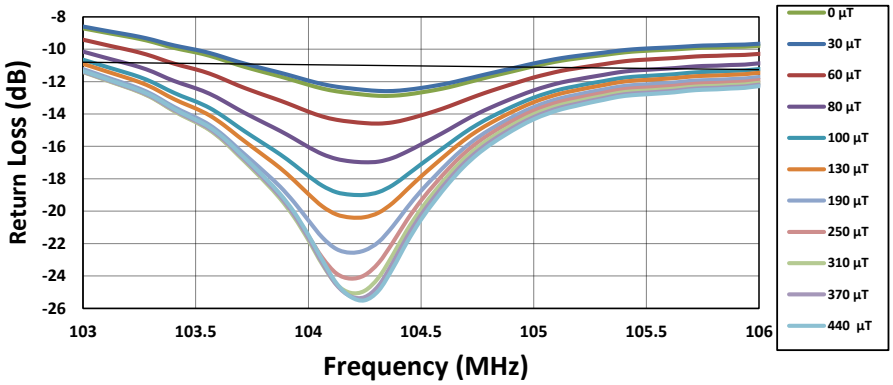

Figure 5.1: Frequency dependence of the loss of GMI-IDT micromagnetic sensor for external magnetic field H_a = 0 to 440 µT

Responses are shown for varying magnetic field, H_a, ranging from 0 µT to 440 µT. For field values up to 310 µT, the largest change in return loss is observed; beyond

these values, the sensor response reaches a saturation region [106] . This effect can be related to the permeability characteristics of the GMI wire as given in equation 4.3. Moreover, Fig. 5.1 illustrates that with increasing magnetic field, the increasing impedance mismatch between GMI wire and IDT leads to a slight shift in the IDT center frequency. Thus, the loss at the saturation magnetic field approaches that of an unloaded IDT. The sensor is also characterized at higher frequencies using harmonics of the IDT. The measured changes in loss and sensitivity responses of the GMI-IDT sensor for three different frequencies of operation are presented in Fig. 5.2 (a) and (b), respectively. The observed sensitivity peaks in Fig. 5.2 (b) are due to the complex permeability behavior of the GMI microwire (see section 4.2) [106] .

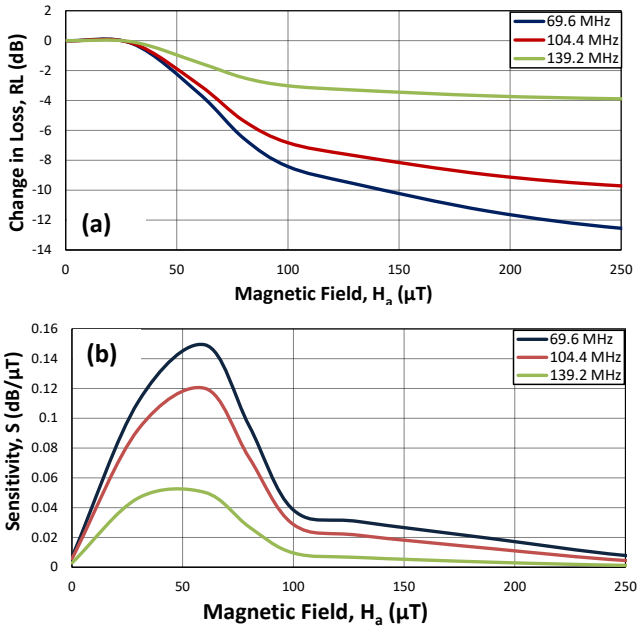

Figure 5.2: GMI-IDT micromagnetic sensor response (a) change in loss and (b) sensitivity as a function of magnetic field for different IDT frequencies

5.3 Characterization of Different GMI Wire Parameters

To enhance the sensitivity and ensure the repeatability of the proposed sensor, several parameters associated with the GMI wires were investigated. First, the effect of stress (i.e., bending) on the GMI wire performance is investigated. To identify the most suitable wire configuration, the impedance characteristics of both straight mounted and coiled GMI wires were measured. Results for each wire are given in Table 5.1. Note that lower impedance is desired for a larger GMI effect, hence straight-mounted wires are selected.

GMI Wire	Measured Peak Impedance (Ω)	Frequency of the Peak Impedance (MHz)
Coil with 1 loop	3769	129
Coil with 2 loop	990	145
Straight wire	**93.30**	**176.5**

Table 5.1: Measured impedance of coil shaped and straight GMI wires

GMI wire impedance was monitored over a period of several days to observe any changes in GMI wire impedance. It has been found that with the application of a static magnetic field of 170 mT, only minimal change in impedance of the wire is observed, indicating a small reduction in the GMI effect. As there is no quantifiable measure of tolerable stress for GMI wires beyond what is described above, it is ensured throughout this work that GMI wires are mounted straight and stress-free.

Following the analysis of the effect of stress on GMI wire impedance, selection of an appropriate length is required. For implementation in the proposed sensor design, the selected GMI wire length should cause maximum change in the overall impedance of the sensor, thus effectively modulating the IDT transduction process. For that purpose, several GMI wires with length varying from 3 to 10 mm were selected for characterization in the initial design of the GMI-IDT sensor for varying magnetic field strengths, the results of which are presented in Fig. 5.3.

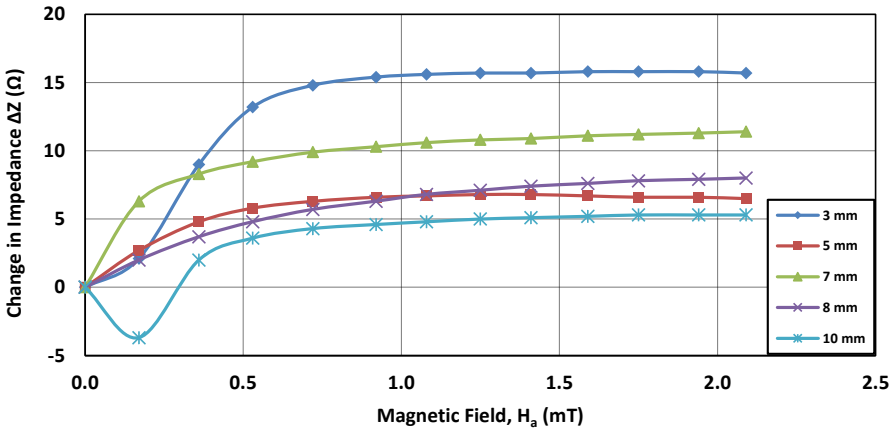

Figure 5.3: Change in impedance of GMI-IDT sensor as a function of magnetic field for GMI wire lengths between 3-10 mm at 104 MHz [98]

As seen in Fig. 5.3, the largest overall change in impedance of the sensor is observed for the 3-mm GMI wire. Particularly important is that the largest magnitude change occurs in the low magnetic field region (below 0.5 mT), which is critically important for our selected application. For GMI wire lengths greater than 5 mm, changes in impedance are smaller in magnitude, thus only wire lengths 5 mm or lower are selected for use in this work.

To further characterize the GMI-IDT sensors with respect to wire length, two lengths are selected based on the results above and characterized for the previously used IDT synchronous frequencies (see Fig. 5.2). The results of this characterization are shown in Fig. 5.4 for the 3-mm and 5-mm GMI wire lengths.

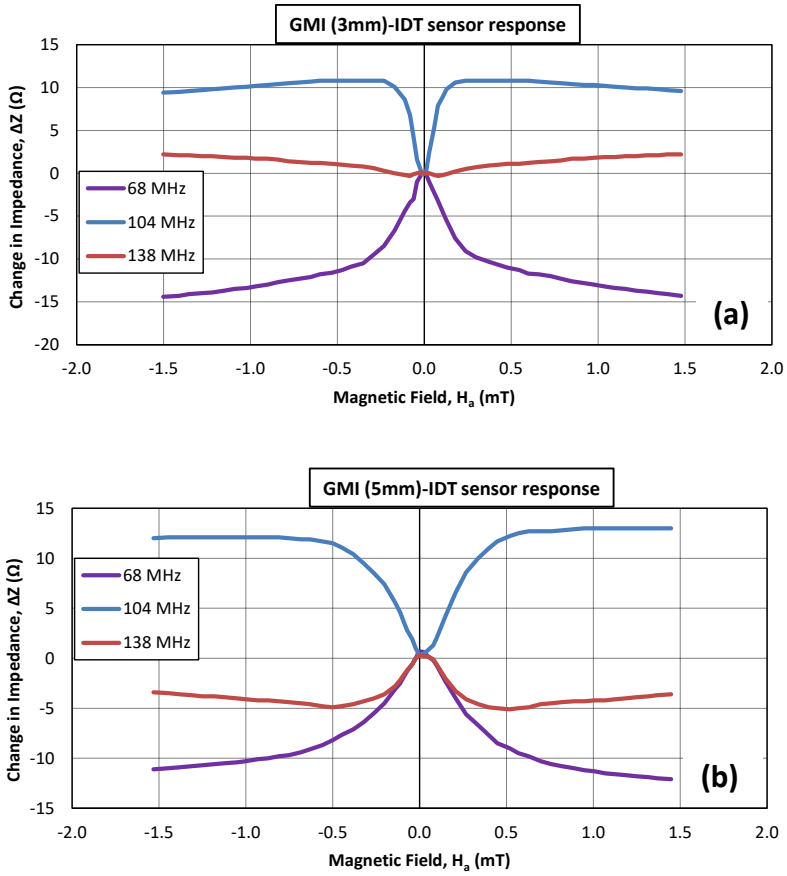

Figure 5.4: Impedance responses of the GMI-IDT sensor to magnetic field for (a) 3 mm, (b) 5 mm GMI wire lengths [98] .

In both cases, there is a sharp change (increase or decrease) in impedance, which is related to the effective anisotropy field, H_K, operating frequency, and length of the wire. For the 3 mm wire length, the change in impedance is observed over a narrower range of

applied magnetic fields for the 68 and 104 MHz frequencies when compared to the 5 mm wire length. This response confirms that high sensitivity can be achieved in various field ranges depending on the microwire length and operating frequency [98] . At 138-MHz the magnetoimpedance is very small, as this is the weakest coupling frequency for this specific IDT design. Note that while a higher slope (i.e., higher sensitivity) is observed for the 3 mm wire length, the 5 mm wire still shows good sensitivity over a wider range of magnetic fields, which could be advantageous for some applications. Similar characterization was performed for the wire lengths ranging from 6 mm to 10 mm. Furthermore, analysis of the dc resistance of the GMI wires as a function of length has been performed. It is observed that for increasing wire length, a corresponding increase in dc resistance is also observed, which is not desirable in this sensor configuration. As discussed previously, large resistances and impedances can impede current flow through the GMI wire and negatively impact the IDT transduction process. Therefore, it is desirable to minimize the dc resistance of the wire. It has been found that a dc resistance of 8-12 Ω is observed for GMI wire lengths between 3-5 mm, indicating that this range of lengths is suitable for the proposed sensor design and will be used for the remainder of this work. The practical importance of the shorter length is that the wire can be ideally used for designing miniaturized magnetic sensing devices, which are required for various applications.

In addition, for the responses shown in Fig. 5.4, the sensor is characterized for both the positive and negative directions of the applied magnetic field. As can be seen, the sensor response is symmetric, indicating that the sensor responds regardless of the direction of the applied magnetic field.

Another important factor investigated here are appropriate preconditioning methods for GMI wires to maximize the stability and ensure the repeatability of the sensor. Several preconditioning methods were investigated as discussed in chapter 4, and the experimental results of each are presented and discussed below:

- Thermal annealing: Prior to mounting the GMI wire to the IDT, the 50°C thermal annealing process described in chapter 4 was used to precondition the GMI wire. Fig. 5.5 shows the return loss of the resulting GMI-IDT sensor at the selected operating frequency. Note that after the first day of operation, a significant reduction in return loss is observed, indicating that this preconditioning method is not suitable for use with the GMI wire. Similar sensor responses were also observed for the sensor with the GMI wire annealed at 100°C. Based on these results, it has been determined that thermal annealing of the GMI wires is not suitable for this work.

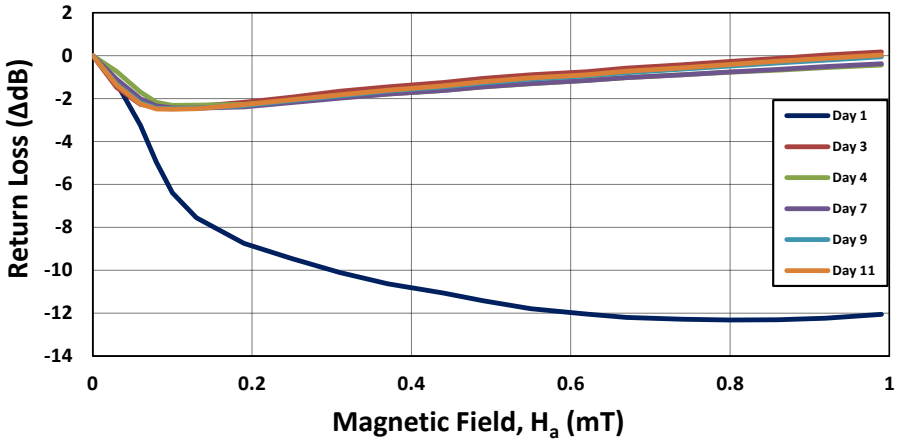

Figure 5.5: Return loss responses of the GMI-IDT sensor consisting of thermally annealed (50°C) GMI wire at 104 MHz

- Current annealing: The GMI-IDT sensors subjected to the current annealing method were characterized with varying magnetic field. From the return loss responses of several sensors with current annealed GMI wires, no observable pattern of repeatability was present. While several sensors were repeatable for several weeks, a sharp decrease in dc resistance was observed resulting in non-repeatable behavior. Similar behavior was observed in ref. [90] .
- Magnetic Field annealing: The GMI-IDT sensors subjected to the magnetic field annealing method were characterized with varying magnetic field. As the return loss response for the sensors shows non-repeatability over several days, other methods were investigated here.
- Simultaneous magnetic field and current annealing: several sensor devices were subjected to simultaneous magnetic field and current annealing with varying annealing time. The annealing process is followed by a fixed relaxation time of 10 min, ensuring the wires have enough time to redistribute internal stress and/or orientation [88] . DC resistance for each sensor preconditioned with this method has been tracked as an indicator of repeatability. The GMI-IDT sensors with GMI wires subjected to this preconditioning method are shown in Table 5.2, with the associated wire length and initial dc resistance included.

GMI-IDT Sensor	Microwire Length, l, (mm)	dc Resistance, R_{DC}, (Ω) (At start)	Annealing Current, I_a, (mA)	Annealing Field, H_a, (mT)	Annealing Time, t_a, (min)	Frequency of I_a, f, (MHz)	Repeatability
1	4	11.9	1.63	1.5	10	50-150	**8 months**
2	4	9.9	1.5	1.5	10	50-150	**6 months**
3	**5**	**8.0**	**1.5**	**1.5**	**8**	**50-150**	**12 months**
4	**4**	**9.45**	**2**	**1.5**	**4**	**50-150**	**50 days**
5	5	7.5	2	1.5	8	50-150	**64 days**

Table 5.2: Parameters associated with the simultaneous current and magnetic field annealing of GMI-IDT sensors

Note that for the majority of the tested sensors, repeatability is observed for several months up to one year. Fig. 5.6 shows the average sensor return loss at 104 MHz measurement frequency for device 3 in Table 5.2. Note that this device was selected as an example, and that all devices considered repeatable showed similar return loss characteristics. This device shows repeatable responses with relatively low error (as shown with the error bars, representing standard deviation of the measurement responses) over a period of 1 year, with large changes in return loss in the targeted low magnetic field region.

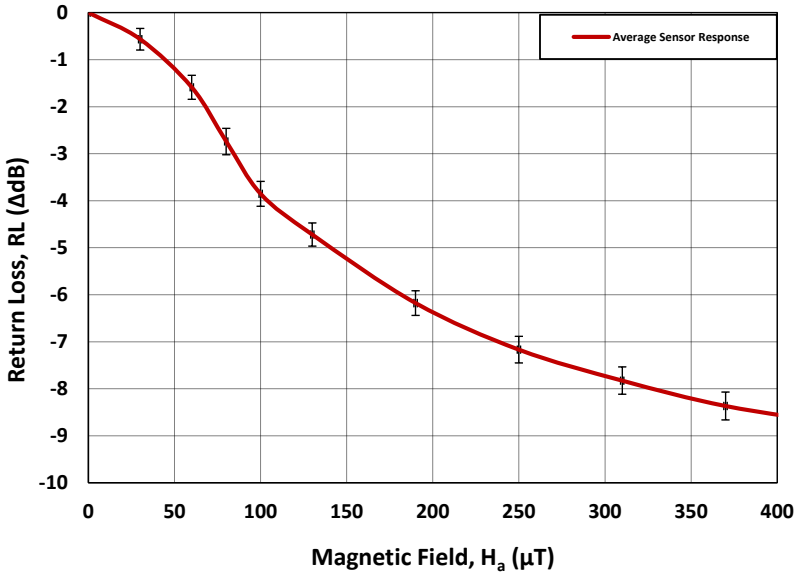

Figure 5.6: Average sensor response of the GMI-IDT sensor (device 3 in table 5.2) at 104 MHz

To visualize sensor repeatability, dc resistance for devices 3 and 5 are plotted together in Fig. 5.7. Note that while the resistance of device 3 remains relatively stable for the lifetime of the sensor, a large drop in resistance is observed for device 5 at 50 days. This indicates potential crystallization inside of the GMI wire of device 5, resulting in non-repeatability of sensor responses.

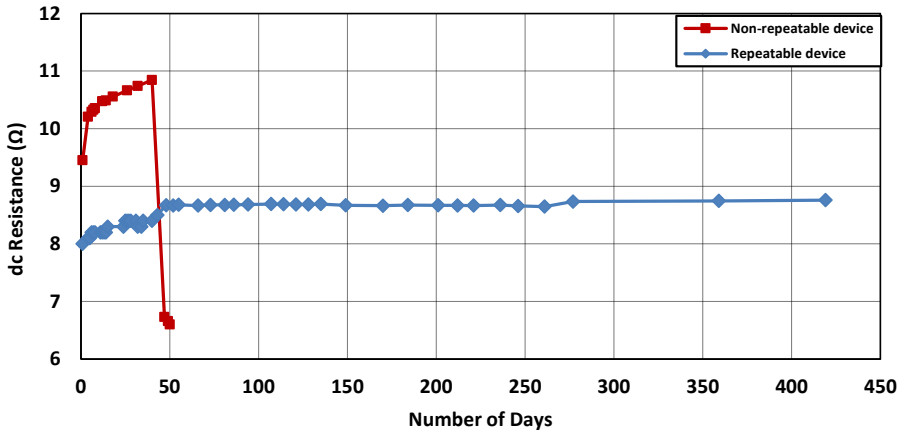

Figure 5.7: Comparison of dc resistance profile of a repeatable and a non-repeatable device (device 3 and device 5, respectively in table 5.2)

Other possible reasons for non-repeatability include aging of the wire and variations in the internal stress distribution resulting from the annealing process. As a large number of the sensors annealed using this method show repeatable responses, this annealing method is selected for preconditioning the GMI wires used in the final sensor design.

5.4 Characterization of Matched GMI-IDT Sensor

To enhance the sensitivity of the designed sensor, the basic sensor design is further modified using the impedance matching technique described in chapter four. At first, the equivalent capacitance of the IDT and other elements was extracted by using a network analyzer. From this approximated capacitance value, using an RF impedance matching calculator [105] , an approximate value for matching inductors and capacitors was estimated. Several inductances and capacitances were tested in series and parallel configurations, and it was found that only series inductances in the range of 22–39 nH

result in good matching. Fig. 5.8 shows the schematic diagram of the GMI-IDT sensor with a matching inductor.

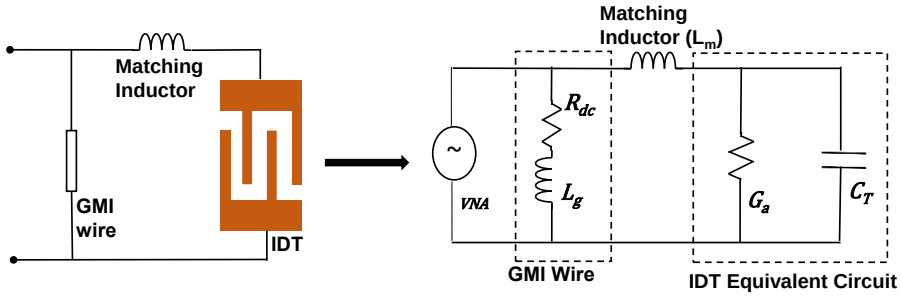

Figure 5.8: Modified design of GMI-IDT sensor with matching inductor

The impact of the matching inductor can be explained using Smith chart analysis of the GMI-IDT sensor. Fig 5.9 shows the Smith chart for a matched sensor with a matching inductor of 27 nH (selected from the above-mentioned inductor range) operating at 104 MHz frequency. The matching element compensate all the capacitive effects in the system, resulting in a purely inductive sensor impedance, which is directly related to the GMI wire inductance as shown in Fig 5.9 (a).

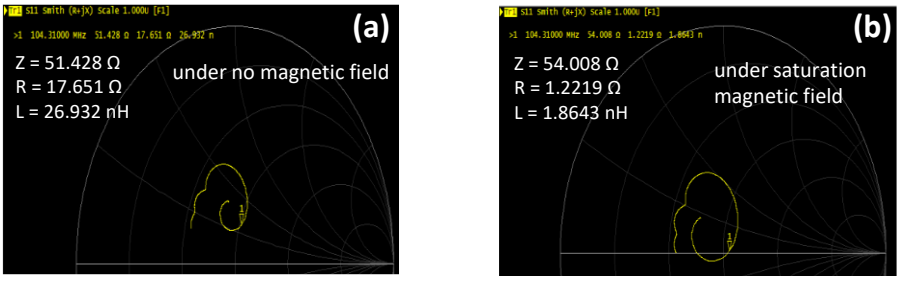

Figure 5.9: Smith chart analysis of a GMI-IDT sensor with matching inductor (a) no external magnetic field (b) under saturation magnetic field. The marker position marks the frequency of operation (104 MHz) of the GMI-IDT sensor

As seen in Fig. 5.9 (b), the sensor impedance approaches the neutral line under the saturation magnetic field condition, implying that only the GMI wire impedance is modulating the IDT transduction process until saturation. Beyond saturation, current flows primarily through the IDT and matching inductor, resembling the response of a perfectly matched IDT. Therefore, to modify the GMI-IDT sensor, a matching inductor should be chosen to eliminate the capacitive effects of the sensor elements. Several designs were modified with the proposed technique, and all were found to be highly sensitive compared to the unmatched GMI-IDT sensor.

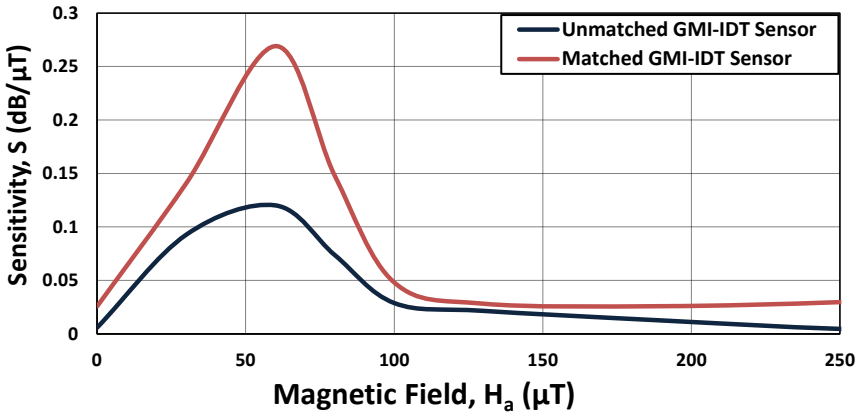

Figure 5.10: Measured sensitivities of GMI-IDT sensors for unmatched and matched sensor designs operated at 104 MHz frequency.

Fig 5.10 shows the extracted sensitivities of a matched and unmatched GMI-IDT sensor [107] . The sensor is matched using a series inductor with an experimentally determined inductance value of 27 nH. The observed peak sensitivity of the unmatched GMI-IDT sensor is 0.12 dB/μT, whereas for a matched GMI-IDT sensor the peak sensitivity is 0.27 dB/μT confirming that the addition of the matching element

significantly increases the sensitivity of the sensor, with peak sensitivity observed at 60 μT. The immediate application of the proposed sensor is to track the changes in magnetic susceptibility of Li-ion batteries, which are expected to be very small of the order of (0.8×10^{-3} SI unit) [26] . As such, the sensitivity of the matched sensor indicates that, provided a reference magnetic field of sufficient strength is used, this sensor is appropriate for the intended application.

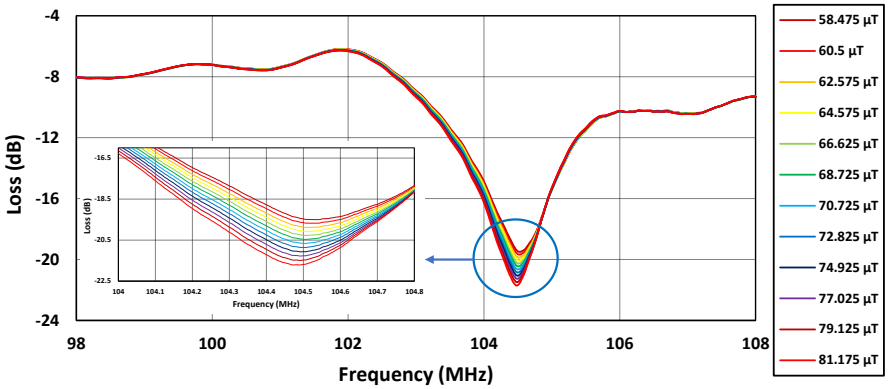

Figure 5.11: Responses of matched GMI-IDT sensor for applied magnetic field ranging from 58 to 81 μT

Furthermore, to establish linearity and frequency dependence of the sensitivity the sensor is calibrated in smaller magnetic field value steps around the peak sensitivity value. Results of this linearity characterization are shown in Fig. 5.11 for magnetic field values between 58 and 81 μT, measured in 2 μT steps [107] . Small variations in the IDT synchronous frequency are observed with changing magnetic field strength (similar to Fig. 5.1), resulting in a peak sensitivity observed at 104.41 MHz.

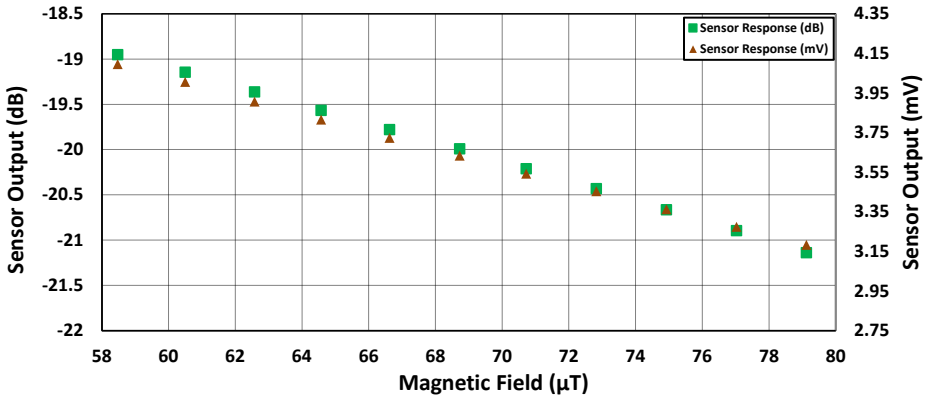

Figure 5.12: Observed linearity of sensor response at 104.41 MHz

After identifying a suitable frequency of operation, the sensor is calibrated for linearity across the previously indicated magnetic field strengths. Results of this linearity analysis are shown in Figure 5.12, with both the measured sensor loss value and the equivalent sensor response on a voltage scale. It is noted that the observed linearity of the response at the selected frequency is good, and thus will provide high accuracy in the magnetic sensor measurement.

5.5 Implementing GMI-IDT Sensor for Monitoring Battery Internal State

The proposed GMI-IDT magnetic sensor is designed to monitor the internal state of the Li-ion battery in a direct and non-invasive manner. As the first step towards this goal, two types of Li-ion batteries are selected to characterize their internal state using the designed GMI-IDT sensor. In this section, the responses of the GMI-IDT sensor in monitoring the internal state of Li-ion cells used in Battery Electric Vehicles (BEV) and Plug-in Hybrid Electric Vehicles (PHEV) will be presented. In addition, the identification of an appropriate experimental setup for those measurements will be discussed.

5.5.1 Optimum Geometry of the Experimental Setup for Battery Measurement

Appropriate placement of the reference magnetic field and sensor relative to the battery cell is critical to this work to quantify the minute variations in magnetic properties during battery cycling. Therefore, efforts have been made to explore several different geometries using reference magnets with different field strengths. The designed sensor and reference magnets were placed in various locations on each type of the Li-ion cell in order to find the best geometry for future battery measurements. The configuration that was found to give the highest sensitivity to changes in batteries magnetic properties is shown in Fig 5.13 for the PHEV cell. Note that a similar configuration will be used for the BEV Pouch cell.

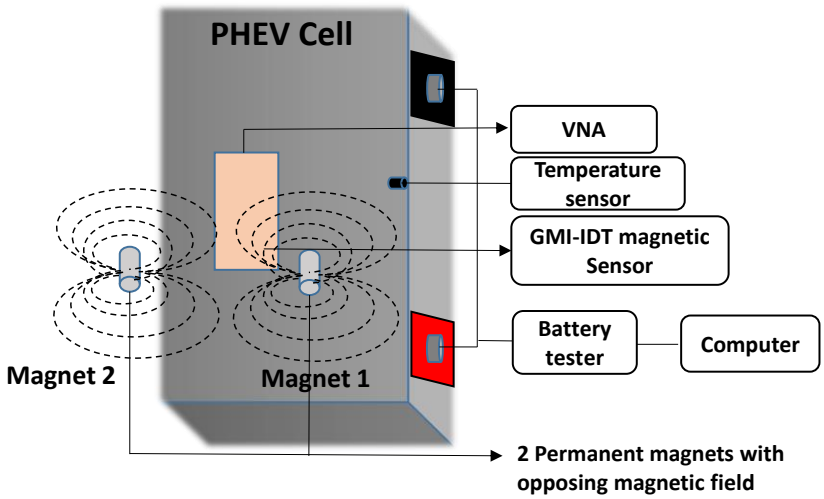

Figure 5.13: Schematic diagram of the optimum geometry for measuring PHEV cell internal state using GMI-IDT sensor

In this configuration, two permanent magnets with opposing magnetic fields are used to provide the reference magnetic field, with the sensor placed between the magnets.

The magnets and sensor are placed such that the sensor will operate in the highly sensitive region identified previously (60 μT). During battery cycling, this reference magnetic field will be perturbed by the changes in magnetic properties of the electrode materials. The magnitude of the perturbation depends on the overall change in magnetic properties of the battery and the strength of the reference magnetic field. The use of strong permanent magnets as a reference static field will ensure that any change in the magnetic properties of the battery will result in relatively large sensor response provided that the sensor is operated in its dynamic range. Thus, the presence of background dc magnetic field (e.g., the geomagnetic field) will not affect the magnetic measurement of the battery. For this experiment, all compression plates were removed from the battery to ensure a close proximity between the battery, sensor and reference magnets.

5.5.2 BEV Pouch Cell Measurement using GMI-IDT Magnetic Sensor

Using the geometry presented in the previous section, the internal state of a Li-ion pouch cell has been measured using the proposed GMI-IDT magnetic sensor. Measurements consist of 10 loops, where each loop has one charge step of 15 mins followed by a rest step of 40 mins. Rest time is constrained to a minimum of 30 minutes, as this is required for accurate estimation of battery OCV [28] . The charging current used for this measurement is 5 Amps. The measurement procedures are selected as such to ensure that the battery will go from a fully discharged state to a fully charged state. The terminal voltage of the battery and the GMI-IDT sensor response are collected simultaneously for the entire measurement to measure the battery's magnetic properties across a charge cycle.

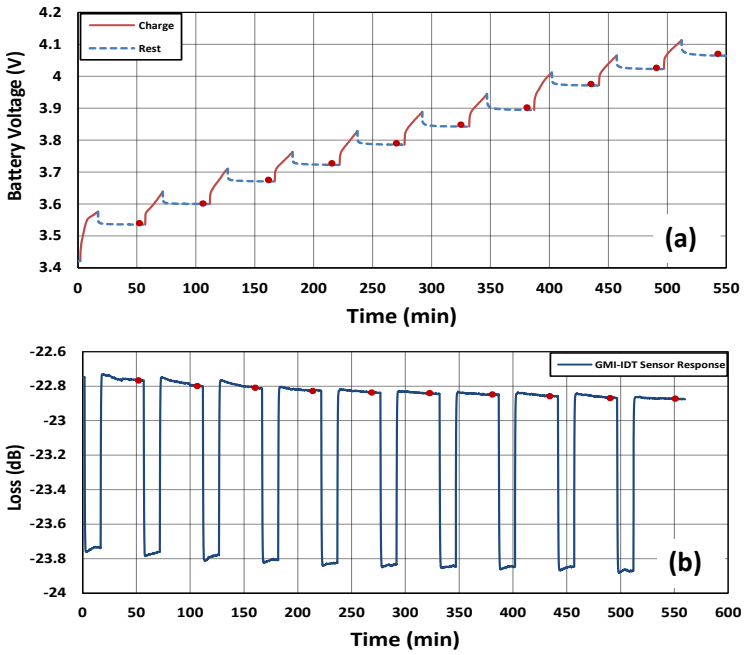

Figure 5.14: BEV pouch cell charging measurement (a) voltage profile (b) corresponding GMI-IDT sensor response at 104.41 MHz

The voltage profile and corresponding sensor response for a BEV pouch cell charging measurement are shown in Fig 5.14. The red dots indicate data taken at the end of each rest step, ensuring the battery reaches an equilibrium state and there are no effects associated with the charging current on the magnetic field. Using these data, the internal state of the battery can be extracted from the battery OCV and the measured response of the GMI-IDT sensor.

The measured data from the sensor response shown in Fig 5.14 (b) are used along with the linearity characteristics of the sensor (shown in Fig 5.12) to find the approximate change in magnetic field which results from a full battery charging cycle. To extract the associated charge capacity of the battery, Coulomb counting method is used (integrating the applied current over time) [11] . In addition, the associated SOC is extracted from

the battery OCV calibration curve, which was obtained as proprietary information from Ford. The sensor response (converted to magnetic field change) as a function of the charge capacity of the battery is shown below in Fig. 5.15 (a), and the associated change in SOC as a function of OCV is shown in Figure 5.15 (b). It is found that a change in charge capacity of 12 Ah, and a change of SOC of 86%, corresponding to a change in magnetic field of 900 nT is measured.

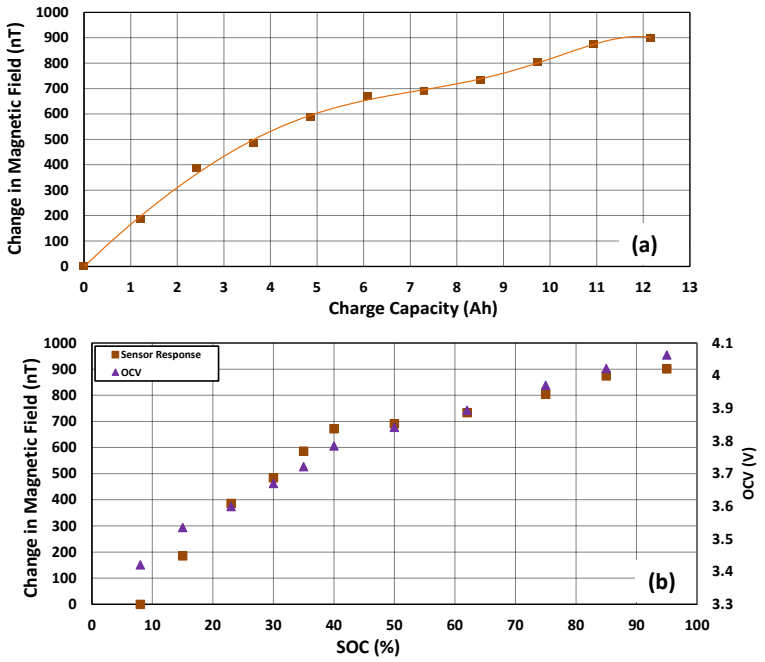

Figure 5.15: GMI-IDT sensor response for BEV pouch cell charging measurement vs (a) battery charge capacity, (b) battery SOC and OCV

However, it is known that extraction of battery SOC from battery OCV is an indirect method and gives only an approximation of the battery SOC, which often leads to measurement inaccuracy [19] . As battery charge capacity is linearly related to SOC, a more direct way to extract SOC is by calculating it directly from the battery charge

capacity [1] . Note that as the battery ages the charge capacity corresponding to 100% SOC decreases compared to a new cell. Therefore, knowledge of battery history is still required for accurate determination of battery SOC. Fig. 5.16 presents battery SOC data calculated using the charge capacity data from Fig. 5.15 (a). It is noted that a calculated change of 82% is observed for this battery with a change in charge capacity of 12Ah, differing slightly from SOC estimated using OCV.

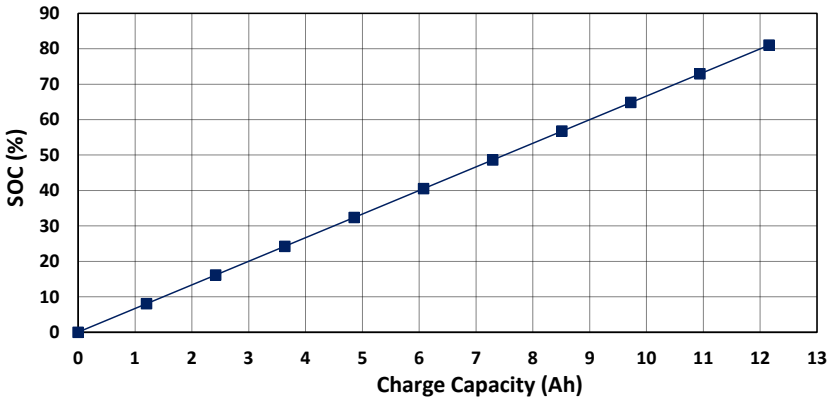

Figure 5.16: Calculated SOC from measured charge capacity for BEV pouch cell measurement

As the changes in magnetic properties of the battery are directly related to the concentration of active Li-ions of the battery electrode [26] , direct magnetic measurement of the internal state of a Li-ion battery provides a more accurate estimation of the remaining charge capacity of the battery. Moreover, because SOC and charge capacity are linearly related, measurement of charge capacity via magnetic sensing can provide more accurate estimation of SOC compared to estimation from OCV, specifically as the battery ages.

5.5.3 PHEV Cell Measurement using GMI-IDT Magnetic Sensor

The voltage profile and corresponding sensor response for the PHEV cell charging and discharging measurements are shown in Figs. 5.17 and 5.18. Note that the same measurement procedure was used for the BEV cell as described in the previous section, with charge/discharge steps of 25 minutes and rest steps of 50 minutes.

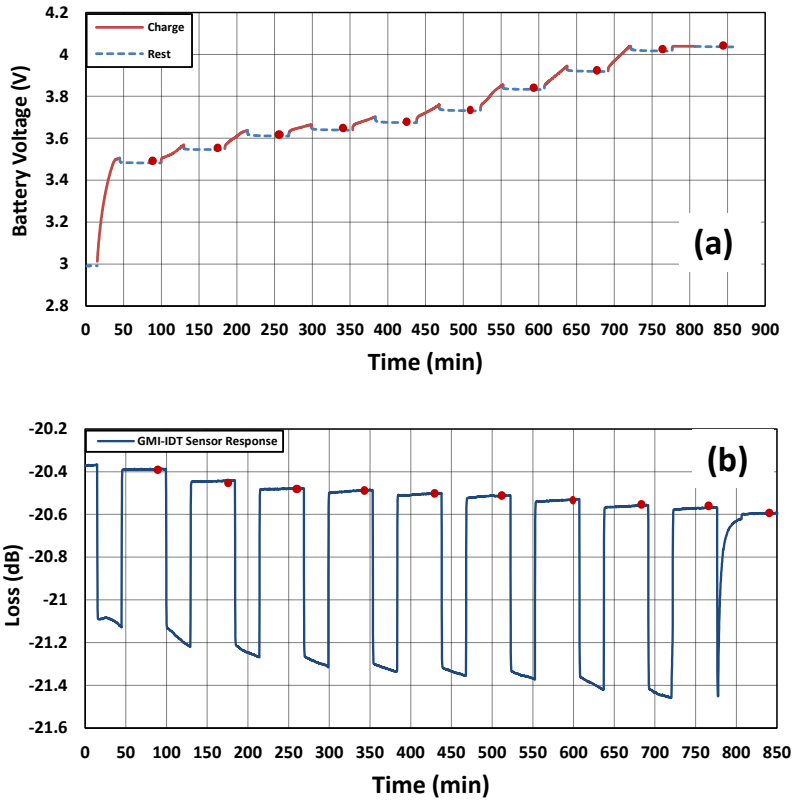

Figure 5.17: PHEV cell charging measurement (a) voltage profile (b) corresponding GMI-IDT sensor response

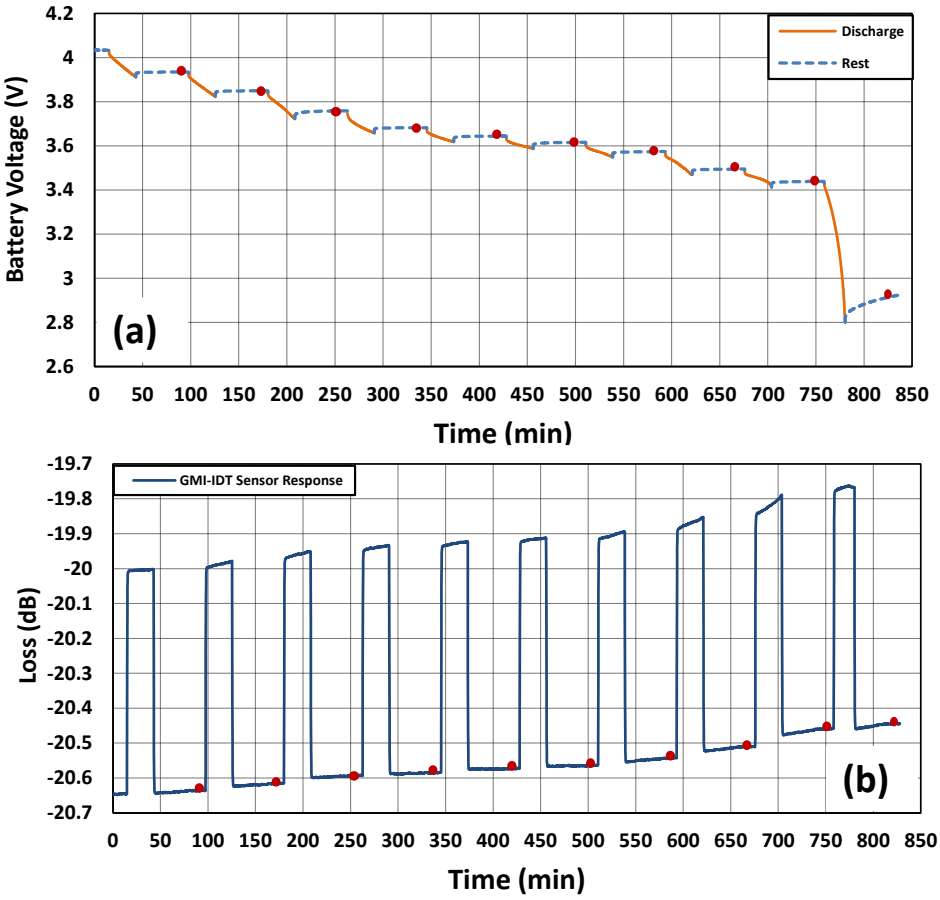

Figure 5.18: PHEV cell discharging measurement (a) voltage profile (b) corresponding GMI-IDT sensor response

The red dot in these figures again indicates data taken at the end of each rest step. As was done for the BEV cell, sensor responses from Figs. 5.17 (b) and 5.18 (b) were converted into corresponding magnetic field values from the sensitivity characteristics of the sensor and correlated with the charge and discharge capacity of the battery, respectively, as shown in Fig 5.19.

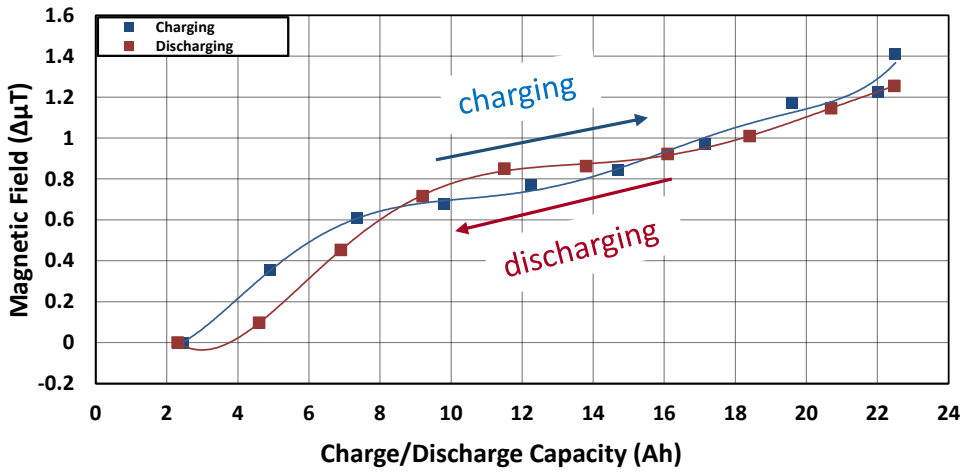

Figure 5.19: Sensor responses for PHEV cell charging and discharging measurement

From Fig 5.19, it is shown that for a change in battery charge capacity of approximately 22 Ah, a change in magnetic field of approximately 1.4 μT is noted. This change in the magnetic field can be correlated with the change in the magnetic properties of the electrode materials. Since the change in battery electrochemistry is reversible, the change in magnetic properties during charging and discharging must be reversible. From the observed sensor response shown in Fig 5.19, it is confirmed that the change in magnetic field during battery charging and discharging follows similar and reversible characteristics. Moreover, the sensor responses reflect the hysteresis behavior of the battery, which is related to the inhomogeneous distribution of the battery materials, specifically the distribution of Li-ions and metal atoms, during battery cycling [26] .

Furthermore, to characterize the repeatability of the responses, both the charging and discharging measurements were performed over several days and plotted together in Fig 5.20 (a). The average sensor response is shown in Fig 5.20 (b). From the observed

responses, it is confirmed that within some measurement scattering the responses are repeatable.

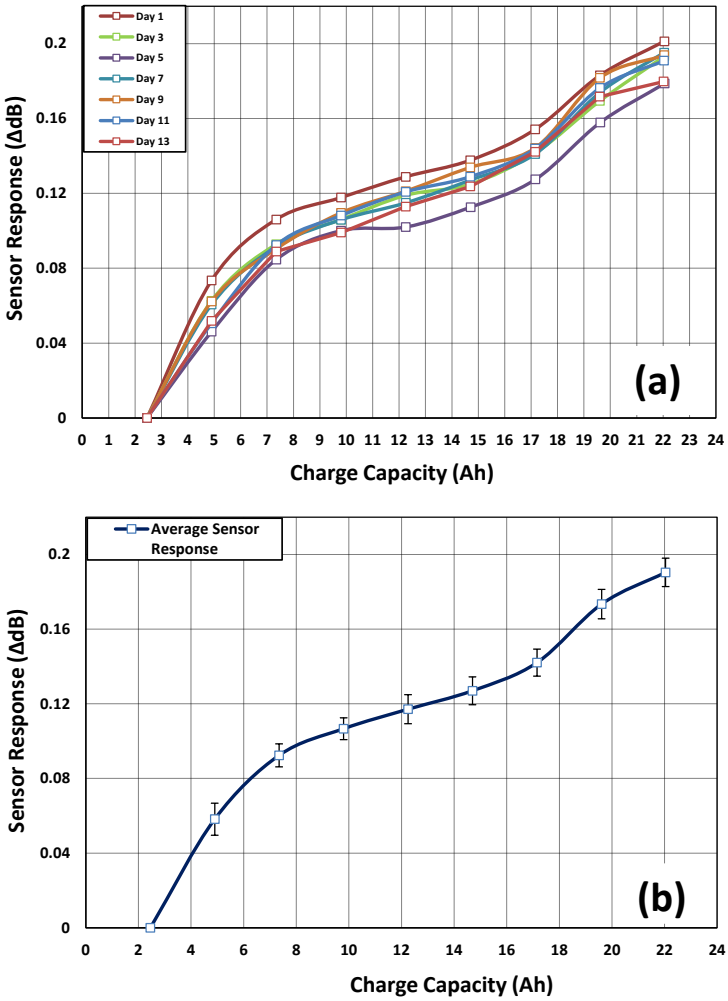

Figure 5.20: Repeatability of response for PHEV cell charging measurement: (a) sensor responses for several days (b) average sensor response; error bars indicating the measurement scattering (standard deviation)

Moreover, the change in sensor responses is steeper when the battery is near the fully charged or discharged states, and smaller when the battery is between these charge

states. Therefore, the sensor exhibits regions of differing sensitivity depending on the charge capacity of the battery, as shown in Fig. 5.21.

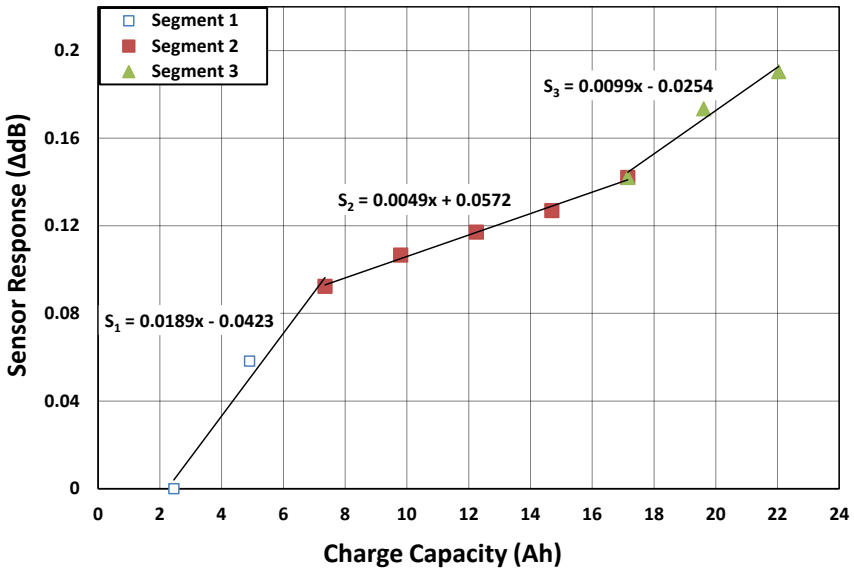

Figure 5.21: Average sensor response divided into different segments for PHEV cell charging measurement

As in the figure above, the average sensor response can be divided into three distinct regions, each with their own unique sensitivity. These differences can be related to the electrochemical changes the battery undergoes during charging and discharging. The materials, which can be influenced during charging/discharging with an externally applied magnetic field, are listed below [28] , [27] , [99] :

- Paramagnetic properties of Li^+ ions
- Oxidation state of the metal atoms in the positive electrode
- Spin state of Co^{4+} ions relative to the concentration of Li- ions

Lithium atoms exhibit diamagnetic or nonmagnetic behavior as demonstrated in spectroscopic measurements [100] . However, Li^+ ions exhibit a small paramagnetic effect under some specific conditions, such as when they are dissolved in polar solvents [101] . For Li-ion batteries, this effect also changes when the battery undergoes aging, which is seen after many battery charging/discharging cycles. During aging, due to irreversible physical and chemical changes, the electrolyte layer decomposes, often resulting in growth/modification of the solid electrolyte interphase (SEI) layer at the anode [100] . In that case, Li^+ ions can show a small paramagnetic effect under an external magnetic field [101] . In this work, since we are not investigating the long-term aging process of the battery, we can neglect the paramagnetic effect of Li^+ ions.

The next parameter that has a significant influence under an external field is the change in the oxidation state of the metal atoms in the positive electrodes during battery cycling (described in chapter one) [26] , [28] , [94] .

The last parameter is the change in the spin state of Co^{4+} ions relative to the active Li-ions concentration present in the electrode compound [27] , [102] , [103] . It has been found that when the concentration of Li-ions in the $Li_{1-x}MO_2$ compound is between $0.94 \leq 1\text{-}x \leq 1.00$, the spin state of the Co^{4+} ions is high and for $0.5 \leq 1\text{-}x \leq 0.78$ the spin state of the Co^{4+} ions is low [27] , [103] . In the high spin state of Co^{4+} ions, the change in the effective magnetic moment is high, reflecting a high perturbation under an external magnetic field. Therefore, the observed sensor response with higher sensitivity found in segment 1 of Fig 5.21 for the charge capacity range 2- 8 Ah, can be correlated with the high spin state of Co^{4+} ions. In contrast, for the low spin state range of Co^{4+} ions, the overall change in the effective magnetic moment is over 5 times lower as compared to the

high spin state. Thus, for the low spin state of Co^{4+} ions, the sensor perturbation under an external magnetic field will be much lower compared to the high spin state region and can therefore be related to segment 2 of the sensor response. Moreover, for $0.5 \leq 1\text{-}x \leq 0.78$ range, the changes in the effective magnetic moment of Co^{4+} ions are linear [27] , which is also seen for segment 2 in Fig 5.21. In the last segment, the sensor response again shows higher sensitivity compared to segment 2, which may be related to the increased concentration of Co^{4+} ions in the positive electrode due to the higher lithiation.

By combining the above, for PHEV cell measurements, the sensor response shows high sensitivity for both the low charge capacity range in segment 1 and high charge capacity range in segment 3. These distinctive characteristics of the sensor response have practical importance, as for presently used OCV technique, the battery cell often cannot be fully charged or fully discharged because the BMS does not have accurate information of SOC/charge capacity [19] . Therefore, to avoid operating in the overcharging or deep discharging regions of the battery, the BMS cannot make full use of the charge capacity of the battery, and often operates well below its rated charge capacity value. These are precisely the battery charge capacity ranges where the GMI-IDT sensor shows maximum sensitivity, which is a promising feature for highly accurate sensor technology.

5.5.4 Comparison of Response Times for GMI-IDT Sensor Technique vs OCV Technique

From the results presented above, it has been confirmed that the internal state of Li-ion batteries used in EVs can be measured using the designed magnetic field sensor. However, before implementing this new technique for practical applications, it is important to assess the proposed technique and compare it with the current state-of-the-

art for battery internal state monitoring. Currently, the most extensively used technique for battery internal state monitoring is the OCV technique, where after a charge and/or discharge period, the batteries are subjected to a long rest time, where the OCV of the battery is recorded at the end of the rest period. This is because a disconnection of the battery terminal from the load after a charge and/or discharge of the battery leads to a recovery effect of the battery [28] , [104] . During the recovery/rest period, the battery reaches an equilibrium voltage level. Therefore, to ensure the accuracy of OCV data, a long rest-time must be provided to the battery, which is often troublesome and limits its efficiency in real-time applications.

Therefore, a comparison of the response time of the OCV techniques and the proposed sensor is investigated. Generally, the response time for OCV is defined as the time required until the change in cell voltage is less than 3mV over a 30 min period [104] . Using this definition, one sample rest step from the BEV and PHEV sensor responses data is selected and shown in Figure 5.22 for comparison with the response time required for the OCV technique. It is found that for the BEV cell and PHEV cell it takes over 35 min for the battery OCV to reach equilibrium. However, in both types of battery, for the GMI-IDT sensor, equilibrium is reached approximately in 1 min. As indicated by the above results, the sensor response reaches equilibrium much faster compared to the OCV response; this is an important step towards near real-time monitoring of battery internal state in practical applications.

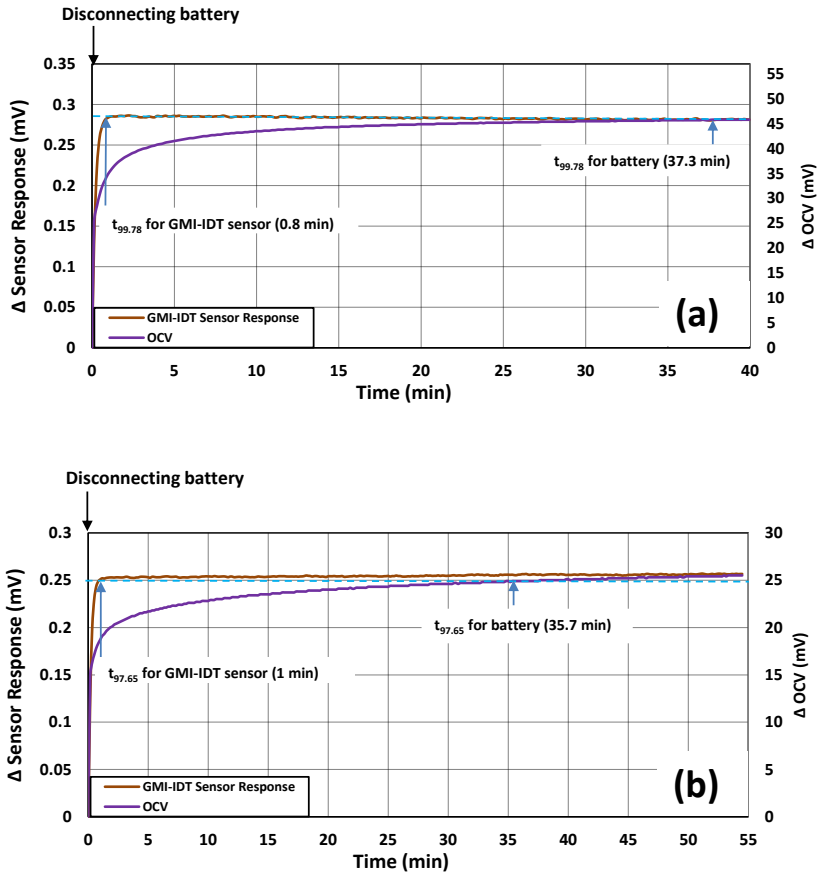

Figure 5.22: Comparison of response times of GMI-IDT sensor response and OCV response for (a) BEV pouch cell (b) PHEV cell

5.6 Summary

This chapter combines all the theories presented in the previous chapters with the experimental results. The proposed sensor is characterized using a known magnetic field and important parameters such as sensitivity, linearity, repeatability, etc. are extracted and analyzed for the sensor. Also, the challenges associated with proper implementation of the designed sensor for monitoring battery internal state were addressed and it has been successfully demonstrated that the designed GMI-IDT sensor can detect the change in magnetic properties of different types of Li-ion batteries used in EVs.

6. SUMMARY, CONCLUSION, AND FUTURE WORK

6.1 Summary

This research is aimed at improving existing BMSs by investigating a novel way of monitoring the internal state of Li-ion batteries directly via magnetic sensing. To achieve this objective, a sensitive micromagnetic sensor design is investigated. Essential characteristics for the proposed sensor and target application include high sensitivity (specifically in the low magnetic field (~μT) region) and low power consumption. Furthermore, the sensor must have the potential for miniaturization, should be functional over a large temperature range, and must have the potential for passive interrogation for sensor arrays for multi-cell battery packs. In the first phase of this research, a thorough investigation of the underlying physics involved in the intended sensor application has been conducted. In addition, an investigation of a suitable sensing platform and magnetically sensitive element was performed. A single IDT on a piezoelectric substrate and GMI microwire were selected as the sensor platform and magnetically sensitive element, respectively, and initial characterization of the design was performed. In the second phase of this work, this initial sensor design was further developed, modified, and implemented in monitoring the magnetic properties of two types of Li-ion battery cells.

Initial sensor designs involved the use of magnetostrictive thin film coatings deposited onto already designed surface acoustic wave devices. Thermal evaporation and magnetron sputtering techniques were used to deposit those coatings with thicknesses varying from 50 nm – 200 nm. The coated devices were characterized with varying field strengths, and found to have relatively poor sensitivity, resulting in other designs being pursued.

Following the magnetostrictive film sensor design, an alternative approach was identified utilizing a single IDT of an acoustic wave device, shunt loaded with a magnetically sensitive giant magnetoimpedance (GMI) element. GMI elements (e.g., microwires, ribbons, films, etc.) exhibit high frequency complex permeability characteristics, with high sensitivity specifically in the low magnetic field (~μT) region and are promising for various applications. This design was selected to take advantage of the coupling of the impedance characteristics of the GMI microwire to the IDT transduction process. Based on the impedance-loaded equivalent circuit model of the IDT, a detailed model of the proposed GMI-IDT sensor was developed. An initial characterization of the GMI-IDT magnetic sensor was performed using an electromagnet to apply dc magnetic fields of specific values to the sensor and measuring the resulting responses. The return loss response of the sensor has confirmed that the magnetic properties of the GMI wires can be quantified through monitoring of the electroacoustic transduction process of the IDT. Specifically, the sensor shows high sensitivity in the targeted low magnetic field region, which is a key characteristic required for the intended application.

To maximize the sensitivity and linearity, the GMI-IDT sensor design is modified using several methods, including the selection and use of an appropriate inductive matching element, identification of suitable GMI wire lengths, and investigation of various GMI wire preconditioning methods to improve sensor response repeatability. It has been found that GMI wire lengths between 3 and 5 mm, and a series matching inductor in the range of 22 to 39 nH result in suitable paring with the selected IDT design. Among several investigated preconditioning methods, the selected method is

simultaneous current and magnetic field annealing (ac current: 1.5 – 2 mA; magnetic field: 1.5 mT, annealing time: 8 – 10 min), which shows repeatable sensor responses over a period of up to one year.

Furthermore, to achieve maximum sensitivity to changes in the magnetic properties of Li-ion batteries, an optimum geometry of the experimental setup was investigated and identified. Finally, the proposed sensor has been implemented for monitoring the internal state of a BEV pouch cell and a PHEV cell. The measured sensor responses confirm that the GMI-IDT sensor can detect variations in the magnetic properties of both cells during charging and discharging.

6.2 Conclusion

This work demonstrates the feasibility of direct, non-invasive, and non-destructive magnetic measurement of the internal state of Li-ion batteries using a novel micromagnetic sensor. It has been shown that the designed sensor can detect small changes in the magnetic properties of Li-ion cells, provided that an appropriate geometry and reference magnetic field are selected for the measurement. An analysis of sensor linearity has demonstrated that the sensor response is linear for magnetic field strengths between 58 – 81 μT, indicating that the sensor shows suitable dynamic range for the intended application. When operated in this highly sensitive linear region, for BEV cell charging measurements the smallest detectable variation in the magnetic field is observed to be ~100 nT, corresponding to a change in charge capacity of ~1 Ah. An overall change in magnetic field of ~900 nT and ~1.4 μT is measured from a full battery charging cycle for the BEV pouch cell and PHEV cell, respectively. As the changes in the magnetic properties of the battery are directly related to the concentration of active Li-ions in the

battery electrode (hence directly related to the battery charge capacity), the observed sensor response can be correlated with the underlying electrochemistry of the batteries. In good agreement with the literature, the observed reversibility and hysteresis in the sensor response for PHEV cell charging and discharging measurement confirms that the change in magnetic properties is reversible and related to the inhomogeneous distribution of the battery materials (e.g., Li-ions, transition metal ions, etc.). Moreover, as charge capacity is directly related to the magnetic properties of the battery electrode material, extraction of charge capacity and determination of battery SOC in this manner will be more accurate, particularly as the battery ages. Therefore, the GMI-IDT sensor enables more accurate determination of the remaining charge capacity of the Li-ion batteries, which could have a major economic impact when applied to electric vehicle BMSs, as well as other industrial applications such as energy storage, particularly for renewable energy sources.

Furthermore, it has been found that for the PHEV cell, the sensor shows distinct sensitivity for different ranges of charge capacity, which is related to the variations in the spin state of the Co^{4+} ions relative to the active Li-ion concentration that dominate in the different charge capacity regions. Specifically, high sensitivity is observed for the GMI-IDT sensor when the battery is near the fully charged (between 17-22 Ah charge capacity) or discharged regions (between 2-8 Ah charge capacity). Accurate detection of the state of charge (SOC) in these regions is crucial for the prevention of overcharging and/or deep discharging of the battery. As the sensor can measure charge capacity in these operative regions precisely, it offers the potential for enabling safer battery operation.

Current battery internal state monitoring techniques only give an approximation of SOC and charge capacity, as such the battery systems are typically overdesigned to operate well below their rated capacity, increasing overall system cost. This can result in inaccurate estimation of charge capacity for multicell battery packs due to charge balancing mismatches for individual cells and reduce the overall available charge capacity of the system. As the proposed technique can provide a more accurate assessment of battery charge capacity, this could lead to a more cost-effective way of monitoring battery internal state by maximizing and appropriately distributing the useable charge capacity of the battery.

The major drawbacks of the current OCV techniques are the need for long rest time for accurate OCV estimation, and often batteries such as pure $LiFePO_4$ batteries have a flat OCV profile. A comparison of the response time of the battery OCV response and GMI-IDT sensor response reveals that equilibrium is reached in approximately 1 min for the GMI-IDT sensor and over 35 min for the battery OCV. The sensor response is much faster than the OCV response, indicating the potential for near-real time extraction of battery internal state, which is not currently possible using the existing monitoring techniques. In addition, current monitoring techniques also require the use of multiple sensors to collect data for accurate estimation of the internal state of a battery, which increases system cost and complexity. The proposed technique utilizes a single sensor to monitor the internal state of a battery non-invasively, drastically reducing system complexity and cost.

Moreover, the proposed approach addressed several additional concerns, such as the impact of background magnetic fields and of battery packaging materials that can

potentially interrupt magnetic measurements of battery internal state. Potential solutions are provided to alleviate these concerns. In conclusion, the proposed technique appears suitable for monitoring the internal state of commercial type battery cells under standard conditions.

6.3 Future Scope

The work presented in this dissertation could be extended upon for further experimental and theoretical work. A few possible research proposals are listed below:

1) Based on the impedance characteristics of the specific composition and diameter of Co-rich GMI wires used in this work, a sensor model and pretreatment techniques were developed. The sensor design and model could potentially be improved by investigating GMI wires having different material compositions such as amorphous Fe-rich fibers and by investigating GMI wires with different diameters.
2) The proposed sensor design utilizes multi-electrode IDTs that are deposited onto a $LiTaO_3$ substrate. However, these devices were designed for other applications such as liquid-phase chemical sensing, and therefore were not modified for this work. Other IDT geometries could be investigated and designed to result in specific IDT equivalent circuit (with appropriate radiation conductance, G_a and electrostatic capacitance, C_T) to maximize the effect of GMI impedance on the IDT transduction process. Also, a study of different IDT designs could include the use of different piezoelectric substrate material, IDT resonator design, etc.
3) Potential methods exist for the designed sensor to be modified for wireless interrogation and passive operation. One such potential method for wireless

interrogation is to use orthogonal frequency coding (OFC) with multiple IDTs deposited on a single substrate material, where each IDT has a different operating frequency. Designing sensor arrays in this way will also enable a differential measurement technique, where the effect of temperature on the sensor responses can be observed, measured, and accounted for. Moreover, a wirelessly interrogated smart sensor system with an IDT array design can be implemented in monitoring the internal state of a multi-cell battery pack.

4) The sensing principle presented here is based on the electrode materials for two specific types of Li-ion batteries. An investigation into other types of Li-ion batteries should be conducted, including other types of batteries containing ferroelectric electrode materials and batteries used for renewable energy sources.
5) In the proposed battery measurement setup, for better proximity of the sensor and reference magnets relative to the battery cell, the compression plates of the battery were removed. The experimental setup can be further improved by integrating the sensor and reference magnet with the compression plate or packaging material.
6) As the charge capacity of the battery decreases with battery aging, long-term magnetic measurements of batteries might enable determination of other parameters related to battery health, such as state of health (SOH) or the formation of solid electrolyte interface (SEI) layer and could potentially help identify defects inside batteries. Therefore, an investigation of long-term battery charge capacity extraction should be performed using the proposed measurement technique.

7) The observed hysteresis on the sensor response for the PHEV cell charging and discharging measurements might depend on the charge or discharge rate. Therefore, an investigation of the magnetic measurements of the battery should be performed with varying charge and discharge rates. This might enable the determination of the nature of the Li-ion distribution and/or motion of the ions in the battery electrode during battery cycling.
8) In this work, all measurements were performed at room temperature. Before applying the proposed technique for EVs, magnetic measurements of the battery with the designed sensor must be conducted in a temperature range of -40 °C to 40 °C to account for the effects of temperature fluctuations on the battery parameters and performance.

REFERENCES

[1] Thomas B. Reddy, "*Linden's Handbook of Batteries*," 4th edition, McGraw Hill, 2011.

[2] Gregory L. Plett, "*Battery Management Systems, Volume II, Equivalent Circuit Methods*," Aetech House, 2016.

[3] B. Scrosati, J. Garche, W. Tillmetz, "*Advances in Battery Technologies for Electric Vahicles,*" Woodhead Publishing Series in Energy, no.80, Uk, 2015.

[4] Y. Xing, E. W. M. Ma, K. L. Tusi, M. Pecht, *"Battery Management Systems in Electric and Hybrid Vehicles"*, Energies, vol 4, pp 1840-1857, 2011. DOI: 10.3390/en4111840.

[5] K. W. E. Cheng, B. P. Divakar, Hongjie Wu, Kai Ding, and Ho Fai Ho, *"Battery-Management System and SOC Development for Electric Vehicles," IEEE Trans on Vehicular Technology,* vol 60, pp 76 - 88, 2011.

[6] https://batteryuniversity.com/learn/article/how_to_measure_state_of_charge

[7] Shyh-Chin Huang, Kuo-Hsin Tseng, Jin-Wei Liang, Chung-Liang Chang, Michael G. Pecht, *"An Online Estimation Model for Lithium-Ion Batteries," Energies,* vol 10, 2017. DOI: 10.3390/en10040512.

[8] Juan Pablo Rivera-Barrera, Nicolás Muñoz-Galeano, Henry Omar Sarmiento-Maldonado, "*SOC Estimation for Lithium-ion Batteries: Review and Future Challenges*," *Electronics,* vol 6, 2017. DOI: 10.3390/electronics6040102.

[9] Cheng Zhang, Kang Li, Jing Deng, and Shiji Song, *"Improved Realtime State-of-Charge Estimation of $LiFePO_4$ Battery Based on a Novel Thermoelectric Model", IEEE Trans on Industrial Electronics,* vol 64, pp 654 - 663, 2017.

[10] Nima Lotfi, Robert G. Landers, Jie Li, and Jonghyun Park, "*Reduced-Order Electrochemical Model-Based SOC Observer With Output Model Uncertainty Estimation*," *IEEE Trans on Control System Technology,* vol 25, pp 1217 - 1230, 2017.

[11] Kong Soon Ng, Chin-Sien Mooa, Yi-Ping Chen, Yao-Ching Hsieh, *"Enhanced coulomb counting method for estimating state-of-charge and state-of-health of lithium-ion batteries," Applied Energy,* vol 86, pp 1506 - 1511, 2009.

[12] L. Lavigne, J. Sabatier, J. Mbala Francisco, F. Guillemard, A. Noury, "*Lithium-ion Open Circuit Voltage (OCV) curve modelling and its ageing adjustment*," *Journal of Power Sources,* vol 324, pp 694 - 703, 2016.

[13] Michael A. Roscher, Dirk Uwe Sauer, *"Dynamic electric behavior and open-circuit-voltage modeling of LiFePO4-based lithium ion secondary batteries", Journal of Power Sources,* vol 196, pp 331 - 336, 2011.

[14] U. Westerhoff, T. Kroker, K. Kurbach, M. Kurrat, *"Electrochemical impedance spectroscopy based estimation of the state of charge of lithium-ion batteries," Journal of Energy Sources,* vol 8, pp 244-256, 2016.

[15] Dave Andre, Christian Appel, Thomas Soczka-Guth, Dirk Uwe Sauer, "*Advanced mathematical methods of SOC and SOH estimation for lithium-ion batteries*" *Journal of Power Sources,* vol. 224, pp. 20 - 27, 2013.

[16] Pritpal Singh, Ramana Vinjamuri, Xiquan Wang, David Reisner, "*Design and implementation of a fuzzy logic-based state-of-charge meter for Li-ion batteries used in portable defibrillators*" *Journal of Power Sources,* vol. 162, pp. 829 - 836, 2006.

[17] Naxin Cui, Chenghui Zhang, Qing Kong, Qingsheng Shi, "*A Combined Method of Battery SOC Estimation for Electric Vehicles,*" 5th IEEE Conference on Industrial Electronics and Applications, pp. 1147 - 1151, 2010.

[18] Gregory L. Plett *"Extended Kalman filtering for battery management systems of LiPB-based HEV battery packs: Part 2. Modeling and identification," Journal of Power Sources*, vol. 134, pp. 262 - 276, 2004.

[19] Gregory L. Plett, *"Battery Management Systems, Volume I, Battery Modelling"*, Aetech House, 2016.

[20] Shankar Mohan, Youngki Kim, Jason B. Siegel, Nassim A. Samad, and Anna G. Stefanopoulou, "*A Phenomenological Model of Bulk Force in a Li-Ion Battery Pack and Its Application to State of Charge Estimation,*" *Journal of the Electrochemical Society,* vol 161, pp. A2222 – A2231, 2014.

[21] Youngki Kim, Nassim A. Samad, Ki-Yong Oh, Jason B. Siegel, Bogdan I. Epureanu and Anna G. Stefanopoulou. *"Estimating State-of-Charge Imbalance of Batteries Using Force Measurements,"* 2016 American Control Conference (ACC), 2016.

[22] Lukas Gold, Tobias Bach, Wolfgang Virsik, Angelika Schmitt, Jana Müller, Torsten E.M. Staab, Gerhard Sextl, "*Probing lithium-ion batteries' state-of-charge using ultrasonic transmission – Concept and laboratory testing*," *Journal of Power Sources,* vol. 343, pp. 536 - 544, 2017.

[23] Lars Wilko Sommer et al., "*Fast and slow ion diffusion processes in lithium ion pouch cells during cycling observed with fiber optic strain sensors," Journal of Power Sources,* vol. 296, pp. 46 - 52, 2015.

[24] Julian Schwartz et al., *"Embedded Fiber Optic Sensors for In Situ and In-Operando Monitoring of Advanced Batteries," Materials Research Society Symposium Proceedings,* vol 1740, pp 7 – 11, 2014.

[25] Matthias Herrmann, *"Packaging – Materials Review"*, AIP Conference Proceedings, vol 121, pp 121-133, 2014.

[26] Thomas Kadyk and Michael Eikerling, "*Magnetic susceptibility as a direct measure of oxidation state in $LiFePO_4$ batteries and cyclic water gas shift reactors*," *Phys.Chem.Chem.Phys.,* vol 17, pp 19834 – 19843, 2015.

[27] J. T. Hertz, Q. Huang, T. McQueen, T. Klimczuk, J. W. G. Bos, L. Viciu, and R. J. Cava, "Magnetism and structure of Li_xCoO_2 and comparison to Na_xCoO_2", Physical Review B, vol 77, pp 075119-1-075119-12, 2008.

[28] Y. Hu, G. Z. Iwata, M. Mohammadi, E. V. Silletta, A. Wickenbrock, J. W. Blanchard, D. Budker, A. Jerschow, "*Sensitive magnetometry reveals inhomogeneities in charge storage and weak transient internal currents in Li-ion cells*," *Proceedings of the National Academy of Sciences,* vol 117, pp 10667–10672, 2020.

[29] R.S. Popovic, J.A. Flanagan, P.A. Besse, "*The future of magnetic sensors*," *Sensors and Actuators A,* vol 56, pp 39 - 55, 1996.

[30] Jacob Fraden, "*Handbook of Modern Sensors Physics, Designs and Applications*," Springer Publications, 2015.

[31] James Lenz and Alan S. Edelstein, "*Magnetic Sensors and Their Applications,*" *IEEE Sensors Journal,* vol 6, pp 631 - 649, 2006.

[32] R S Popovic, "Hall Effect Devices", CRC Press, 2003.

[33] Eyal Weiss, Roger Alimi, "*Low-Power and High-Sensitivity Magnetic Sensors and Systems*," Artech House, 2019.

[34] D. S. Ballantine, R. M. White, S. J. Martin, A. J. Ricco, G. C. Frye,E. T. Zellers, and H. Wohltjen, *"Acoustic Wave Sensors: Theory, Design and Physico- Chemical Applications",* Academic Press, San Diego, 1997.

[35] R.M. White, F.W.Voltmer, *"Direct Piezoelectric Coupling to Surface Elastic Waves", Applied Physics Latters,* vol. 7, no. 12, pp 314-316, 1965.

[36] B. Drafts, *"Acoustic wave technology sensors," IEEE Trans.on Microwave Theory and Techniques*, vol. 49, pp. 795-802, 2001.

[37] C. K. Campbell, *"Surface Acoustic Wave Devices for Mobile and Wireless Application",* Academic Press, San Diego, 1998.

[38] A. J. Slobodnik Jr., *"Surface Acoustic Wave and SAW Materials"*, Proceedings of the IEEE, vol 64, no 5, pp 581 - 595 , 1976.

[39] W. R. Smith, H. M. Gerard, J. H. Collins, T. M. Redder, H. J. Shaw, *"Ananlysis of Interdigital Surface Wave Transducers by Use of an Equivalent Circuit Model," IEEE Trans on Microwave Theory and Techniques,* vol. MTT-17, no 11, pp 856 - 864, 1969.

[40] D.P. Morgan, *"Surface Acoustic Wave Devices and Applications"*, Ultrasonics, 1973, vol 11, pp 121-131.

[41] W. R. Smith, H. M. Gerard, W.R.Jones *"Analysis and Design of Dispersive Interdigital Surface-Wave Transducers," IEEE Trans on Microwave Theory and Techniques,* vol. MTT-20, no 7, pp 458 - 471, 1972.

[42] W.R. Smith, Jr. *"Minimizing Multiple Transit Echoes in Surface Wave Devices," IEEE Ultrasonic Symposium,* 1973, pp 410-413.

[43] Kentaro Hanma, Bill J. Hunsinger, "*A triple Transit Suppression Technique*," in *IEEE Ultasonic Symposium* 1976, pp. 328-331.

[44] D.C.Webb, D.W.Forester, A.K.Gangu1y and C.Vittoria, "*Applications of amorphous magnetic-layers in surface-acoustic-wave devices*", IEEE Transactions on Magnetics, vol. 15, no. 6, pp 1410-1415, 1979.

[45] J.Tong, Y.Jia, W.Wang, Y.Wang, S.Wang, X. Liu and Y.Lei, "*Development of a Magnetostrictive FeNi Coated Surface Acoustic Wave Current Sensor*", Applied Science, vol. 7, no. 755, 2017. doi:10.3390/app7080755.

[46] W.Wang, Y.Jia, X. Liu, Y. Liang, *"Performance Improvement of the SAW Based Current Sensor Incorporating a Strip-Patterned Magnetostrictive FeCo Film",* 2017 IEEE International Ultrasonics Symposium (IUS), 2017. doi:10.1109/ULTSYM.2017.8091986

[47] Bodong Li, Omar Yassine, and J. Kosel, *"A Surface Acoustic Wave Passive and Wireless Sensor for Magnetic Fields, Temperature, and Humidity",* IEEE Sensors Journal, vol. 15, no. 1, pp 453-462, 2015.

[48] A. Mensah-Brown, *"Analysis of the Detection of Organophosphate Pesticides in Aqueous Solutions Using Polymer Coated SH-SAW Devices",* Ph.D. dissertation, Dept. Elec. Comp. Eng., Marquette Univ., Milwaukee, WI, 2010.

[49] Z. Li, *"Guided Shear-Horizontal Surface Acoustic Wave (SH-SAW) Chemical Sensors for Detection of Organic Contaminants in Aqueous Environments",* Ph.D. dissertation, Dept. Elec. Comp. Eng., Marquette Univ., Milwaukee, WI, 2005.

[50] Richard M. Bozorth, *"Ferromagnetism",* First reissued ed., Piscataway, NJ: IEEE Press, reissued 1993.

[51] F. Josse, F. Bender, R. W. Cernosek, *"Guided Shear Horizontal Surface Acoustic Wave Sensors for Chemical and Biochemical Detection in Liquids"*, Anal. Chem, vol 73, pp 5937-5944.

[52] C. Liang, C. P. Gooneratne, Q. X. Wang, Y. Liu, Y. Gianchandani and J. Kosel, *"Magnetic Properties of FeNi-Based Thin Film Materials with Different Additives",* Biosensors, vol. 4, pp 189-203, 2014. doi: 10.3390/bios4030189.

[53] P.J. Kelly, R.D. Arnell, *"Magnetron sputtering: a review of recent developments and applications",* Vaccum, vol. 56, pp 159-172, 2000.

[54] A. Kittmann, P. Durdaut, S. Zabel, J. Reermann, J. Schmalz, B. Spetzer, D. Meyners, N. X. Sun, J. McCord, M. Gerken, G. Schmidt, M. Höft, R. Knöchel, F. Faupel, E. Quandt*, "Wide Band Low Noise Love Wave Magnetic Field Sensor System"*, Scientific Reports, vol. 8, no. 288, 2018. doi: 10.1038/s41598-017-18441-4.

[55] K. Mohri, T. Uchiyama, L. V. Panina, M. Yamamoto, K. Bushida, *"Recent Advances of Amorphous Wire CMOS IC Magneto-Impedance Sensors: Innovative High-Performance Micromagnetic Sensor Chip",* J. of Sensors, vol 2015, 718069, June 2015.

[56] L. Karus, *"GMI modeling and material optimization",* Sensors and Actuators A, vol 106, pp. 187-194, 2003.

[57] M. Vázquez, M. Knobel, M. L. Sánchez, R. Valenzuela, A. P. Zhukov, *"Giant magnetoimpedance effect in soft magnetic wires for sensor applications",* Sensors and Actuators A, vol 59, pp. 20-29, 1997.

[58] M.-H. Phan, H.-X. Peng, *"Giant magnetoimpedance materials: Fundamentals and applications",* Progress in Materials Science, vol. 53, pp 323-420, 2008.

[59] H. Chiriac and T. A. Óvári, *"Amorphous Glass-Covered Magnetic Wires: Preparation, Properties, Application",* Progress in Material Science, vol. 40, pp 333-407, 1996

[60] Md. Kamruzzaman, I.Z.Rahman, M.A.Rahman, *"A review on magneto-impedance effect in amorphous magnetic materials",* Journal of Material Processing Technology, vol. 119, pp 312-317, 2001.

[61] Faxiang Qin and Hua-Xin Peng, *"Ferromagnetic microwires enabled multifunctional composit materials",* Progress in Material Science, vol. 58, pp 183-259, 2013.

[62] I. Giouroudi, H. Hauser, L. Musiejovsky, and J. Steurer, *"Giant magnetoimpedance sensor integrated in an oscillator system",* J. Appl. Phys., vol. 99, no. 8, 2006. doi: 10.1063/1.2170051.

[63] Y. Honkura, *"Development of amorphous wire type MI sensors for automobile use",* J. Magnetism and Magnetic Materials, vol. 249, pp 375-381, 2002.

[64] K. Mohri, T. Uchiyama, L.P. Shen, C.M. Cai, L.V. Panina, *"Amorphous wire and CMOS IC-based sensitive micro-magnetic sensors (MI sensor and SI sensor) for intelligent measurements and controls",* J. Magnetism and Magnetic Materials, vol. 249, pp 351-356, 2002.

[65] B. Li, H. Al Rowais, and J. Kosel, *"Surface Acoustic Wave Based Magnetic Sensors",* Intech Open, 2013, pp. 355–380, DOI: 10.5772/55220.

[66] L. V. Panina, K. Mohri, *"Magneto-impedance effect in amorphous wires",* Appl. Phys. Lett., vol 65, no. 9, pp. 1189-1191, August 1994.

[67] L. V. Panina, K. Mohri, K. Bushida, M. Noda, *"Giant Magneto-impedance and magneto-inductive effects in amorphous alloys (invited)",* J. Appl. Phys., vol 76, no. 10, pp. 6198-6203, November 1994.

[68] L. V. Panina, K. Mohri, T. Uchyama, and M. Noda, "Giant Magneto-Impedance in CO-Rich Amorphous Wires and Films", IEEE Trans. Magnetics, vol. 31, no. 2, pp 1249- 1260, 1995.

[69] A. Chaturvedi, *"Novel Magnetic Materials for Sensing and Cooling Application",* Ph.D. dissertation, Dept. Phisics, University of South Florida, Tampa, Florida, 2011.

[70] D. Atkinson, and P. T. Squire, *"Phenonemological model for magnetoimpedance in soft ferromagnets",* Journal of Applied Physics, vol. 83, no. 11, pp 6569- 6571, 1998.

[71] I. Betancourt, R. Valenzuela, and M. Vazquez, *"Domain model for the magnetoimpedance of metallic ferromagnetic wires",* Journal of Applied Physics, vol. 93, no. 10, pp 8110- 8112, 2003.

[72] D. Ménard, M. Britel, P. Ciureanu, and A. Yelon, *"Giant magnetoimpedance in a cylindrical magnetic conductor",* Journal of Applied Physics, vol. 84, no. 5, pp 2805- 2814, 1998.

[73] M. R. Britel, D. Ménard, L. G. Melo, P. Ciureanu, A. Yelon, R. W. Cochrane, M. Rouabhi, B. Cornut, *"Magnetoimpedance measurements of ferromagnetic resonance and antiresonance",* Applied Physics Letter, vol. 77, no. 17, pp 2737-2739, 2000.

[74] L. D. Landau and Lifshitz, *"Electrodynamics of Continuous Media",* Course of Theoretical Physics, 2nd ed., vol 8, NY 10523, U.S.A.

[75] H. Hauser, R. Steindl, Ch. Hausleitner, J. Nicolics and A. Pohl, *"Miniaturized Magnetic Field Sensors Utilizing Giant Magneto-Impedance [GMI] Effect and Surface Acoustic Wave [SAW] Technology,"* Sens. Mater., vol. 13, pp. 025-040, 2001.

[76] J. Ström-Olsen, *"Fine fibres by melt extraction",* Materials Science and Engineering, vol. 178, pp. 239-243, 1994.

[77] V. Zhukova, A. Zhukov, K.L. García, V. Kraposhin, A. Prokoshin, J. Gonzalez, M. Vázquez, *"Magnetic properties and GMI of soft melt-extracted magnetic amorphous fibers",* Sensors and Actuators A, vol. 106, pp. 225-229, November 2003.

[78] K. V. Rao, F. B. Humphrey, J. L. Costa-Krämer, *"Very large magneto-impedance in amorphous soft ferromagnetic wires",* J. of Applied Physics, vol. 76, No. 10, pp. 6204-6208, November 1994.

[79] Vijay V. Kondalkar, Xiang Li, Ikmo Park, Sang Sik Yang and Keekeun Lee, *"Development of chipless, wireless current sensor system based on giant magnetoimpedance magnetic sensor and surface acoustic wave transponder"*, Scientific Reports, 2018, DOI:10.1038/s41598-018-20867-3.

[80] D. Me´nard, M. Britel, P. Ciureanu, and A. Yelon, V. P. Paramonov and A. S. Antonov, P. Rudkowski and J. O. Stro¨m-Olsen, *"High frequency impedance*

spectra of soft amorphous fibers", Journal of Applied Physics, vol. 81, no. 8, pp 4032-4034, 1997.

[81] M. Heshmatzadeh et al., *"High-Frequency Giant Magnetoimpedance Measurement and Complex Permeability Behavior of Soft Magnetic Co- Based Ribbons",* IEEE Trans on Magnets, vol. 41, pp. 2328–2333, 2005.

[82] V. Zhukova, N. A. Usov, A. Zhukov, and J. Gonzalez1, *"Length effect in a Co-rich amorphous wire",* Physical Review B, vol. 65, no. 13, pp. 134407-1 :134407-7, 2002.

[83] M.H. Phana, H.X. Penga, S.C. Yub, M.R. Wisnom, *"Large enhancement of GMI effect in polymer compositescontaining Co-based ferromagnetic microwires"*, J. Magnetism and Magnetic Materials, vol. 316, pp 253-256, 2007.

[84] P. Ciureanu, G. Rudkowska, P. Rudkowski, and J. 0. StrZim-Olsen, "Magnetoresistive Sensors with Rapidly Solidified Permallov Fibers", IEEE Transactions on Magnetics, vol. 29, no. 5, September 1993.

[85] J. Nabias, A. Asfour and Jean-Paul Yonnet, *"The Impact of Bending Stress on the Performance of Giant Magneto-Impedance (GMI) Magnetic Sensors"*, Sensor, vol.17, doi:10.3390/s17030640.

[86] Y. Honkura, M. Yamamoto, N. Hamada, A. Shimode,*" Magneto-sensitive wire, magneto-impedance element and magneto-impedance sensor"*, European Patent Specification, 09724160.8, Mar. 03, 2009.

[87] A. Zhukov, A. Talaat, J. M. Blanco, M. Ipatov and V. Zhukova, *"Tuning of Magnetic Properties and GMI Effect of Co-Based Amorphous Microwires by Annealing"*, Journal of Electronic Materials, vol. 43, no. 12, 2014.

[88] Y. K. Kim, W. S. Cho, T. K. Kim, C. O. Kim, and Heebok Lee, *"Temperature dependence of magnetoimpedance effect in amorphous $Co_{66}Fe_4NiB_{14}Si_{15}$ ribbon"*, Journal of Applied Physics, vol. 83, no. 11, 1998.

[89] M. Knobel, M. L. Sa´nchez, C. Go´mez-Polo, P. Marı´n, M. Va´zquez, and A. Hernando, *"Giant magneto-impedance effect in nanostructured magnetic wires"*, Journal of Applied Physics, vol. 79, no. 3, 1998.

[90] H. Chiriac and I. Astefanoaei, *"A Model of the DC Joule Heating in Amorphous Wires"*, Phys. Stat. Sol. vol. 153, pp 183-189, 1996.

[91] P Klein, R Varga1, P Vojtanik1, J Kovac, J Ziman, G A Badini-Confalonieri and M Vazquez, *"Bistable FeCoMoB microwires with nanocrystalline microstructure and increased Curie temperature",* J. Phys. D: Appl. Phys., vol. 43, 2010. doi:10.1088/0022-3727/43/4/045002.

[92] J.S. Liua, X.D. Wanga, D.M. Chena, F.X. Qinc, H. Wanga, D.W. Xinga, X. Xuea, J.F. Sun, *"Comparative Study on Magnetic Properties and Microstructure of As-prepared and Alternating Current Joule Annealed Wires"*, Physics Procedia, vol. 48, pp 140-145, 2013.

[93] K.R. Pirota, L. Kraus, H. Chiriac, M. Knobel, *"Magnetic properties and giant magnetoimpedance in a CoFeSiB glass-covered microwire"*, Journal of Magnetism and Magnetic Materials, vol. 221, pp L243-L247, 2000.

[94] T. Gallien, H. Krenn, R. Fischer, S. Lauterbach, B. Schweighofer, H. Wegleiter, *"Magnetism Versus LiFePO4 Battery's State of Charge: A Feasibility Study for Magnetic-Based Charge Monitoring",* IEEE trans. On Instrumentation and Measurement, vol 64, no 11, pp 2959 - 2964, 2015.

[95] F. Bender, R.E. Mohler, A.J. Ricco, and F. Josse, *"Analysis of Binary Mixtures of Aqueous Aromatic Hydrocarbons with Low-Phase-Noise Shear-Horizontal Surface Acoustic Wave Sensors Using Multielectrode Transducer Design"*, Anal Chem., vol. 86, pp. 11464-11471, 2014.

[96] P. Adhikari, *"Plasticized Polymer Coatings for SH-SAW Sensors for High Sensitivity and Long-Term Monitoring of BTEX Analytes in Liquid Phase",* M.S. Thesis, Dept. Elec. Comp. Eng., Marquette Univ., Milwaukee, WI, 2016.

[97] https://mountsopris.com/kt-10-magnetic-susceptibility-and-conductivity-meters/

[98] A. Khatun, F. Bender, F. Josse, A. K. Mensah-Brown, R. D. Anderson, *"High-Sensitivity Magnetic Sensor Based on GMI Microwire-SAW IDT Design,",* 2019 Joint Conference of the IEEE International Frequency Control Symposium and European Frequency and Time Forum (EFTF/IFC), doi: 10.1109/FCS.2019.8856050.

[99] P. Singh, N. Khare, P.K. Chaturvedi, *"Li-ion battery ageing model parameter: SEI layer analysis using magnetic field probing",* Engineering Science and Technology, an International Journal, vol 21, pp 35-42, 2018.

[100] C. M. Julien, A. Ait-Salah, A. Mauger, F. Gendron, *"Magnetic properties of lithium intercalation compounds"*, DOI: 10.1007/s11581-006-0007-5.

[101] W. R. Myers, *"Magnetism of Hydrogen and Lithium Ions"*, Nature, vol 167, pp 1073-1074, 1951.

[102] N. A. Chernova, M. Ma, J. Xiao, M. S. Whittingham, J. Breger, C. P. Grey, *"Layered $Li_xNi_yMn_yCo_{1-2y}O_2$ Cathodes for Lithium Ion Batteries: Understanding Local Structure via Magnetic Properties"*, Chem. Mater, vol 19, pp 4682-4693, 2007

[103] N. A. Chernova, G. M. Nolis, F. O. Omenya, H. Zhou, Z. Li, M. S. Whittingham, *"What can we learn about battery materials from their magnetic properties?"*, J. Mater. Chem., vol 21, pp 9865-9875, 2011.

[104] B. Lawson, *"A Software Configurable Battery"*, EVS26, Los Angeles, California, May 6-9, 2012.

[105] https://www.analog.com/en/design-center/interactive-design-tools/rf-impedance-matching-calculator.html#

[106] A. Khatun, F. Bender, F. Josse, A. K. Mensah-Brown, R. D. Anderson, D. Washington, *"Micromagnetic Sensor Utilizing Single SAW IDT Shunt-Loaded with GMI Wire"*, 2020 Joint Conference of the IEEE International Frequency Control Symposium and IEEE International Symposium on Applications of Ferroelectrics (IFCS-ISAF), doi: 10.1109/IFCS-ISAF41089.2020.9234856.

[107] A. Khatun, F. Bender, F. Josse, A. K. Mensah-Brown, *"Direct Monitoring of Battery SOC Utilizing GMI-IDT Magnetic Sensor"*, 2021 Joint Conference of European Frequency and Time Forum and the IEEE International Frequency Control Symposium (EFTF-IFCS), doi:10.1109/EFTF/IFCS52194.2021.9604260.